NUMERICALLY EXACT COMPUTATION OF STATIC FRICTION FOR MANY-BODY PROBLEMS

DOMINIK KRENGEL

THE UNIVERSITY OF ELECTRO-COMMUNICATIONS

GRADUATE SCHOOL OF INFORMATICS AND ENGINEERING

A DISSERTATION SUBMITTED FOR DOCTOR OF PHILOSOPHY IN SCIENCE

MAY 14, 2019

NUMERICALLY EXACT COMPUTATION OF STATIC FRICTION FOR MANY-BODY PROBLEMS

APPROVED BY SUPERVISORY COMMITTEE:
CHAIRPERSON: Assoc. Prof. Hans-Georg Matuttis
MEMBER: Prof. Takeshi Miyazaki
MEMBER: Prof. Tomio Okawa
MEMBER: Prof. Naruo Sasaki
MEMBER: Assoc. Prof. Hiroya Mamori

Numerically exact computation of static friction for many-body problems

Dominik Krengel

ABSTRACT

Up to now there has been no exact formalism to determine static friction forces in many-particle configurations with arbitrary contact orientations as reaction to prescribed normal forces. There are models for non-rigid bodies as well as rigorous rigid body solutions for a single contact, such as the case of a block on an inclined plane. If the normal force is known, then the friction force can easily be found, and if $\arctan(\alpha) < \mu$, then we find the static friction force as $F^{\text{fric,stat}} = F^N \tan(\alpha)$. However, taking static friction as $F^{\text{fric,stat}} = \mu F^N$ in the sense of Coulomb friction leads to a problem: Numerical inaccuracies in the determination of $v = 0$ can lead to absurd results such as the block climbing up the slope. The problem becomes more complex with increasing number of contacts. For many-body systems, such as a heap of sand with many thousand contacts, with prescribed normal forces and given friction coefficients, the approach to compute solid friction forces has been lacking throughout the development of classical mechanics. Even if we know the normal forces F_i^{N} and the friction coefficients μ_i, how can we compute the static friction forces $F_i^{\text{fric,stat}}$ so that the heap is stable? It is rather obvious that $F^{\text{fric,stat}} \neq \mu F^{\text{N}}$. But if taking the value of dynamic friction for static friction has already been wrong for a single contact, what will be required if we have systems with thousands or millions of inclined contacts? While analytical formalisms in the framework of rigid body dynamics exist, they are not generalisable beyond linear chains of particles and general treatment of many-body friction has been lacking until now.

The purpose of this thesis is to develop a formalism which gives analytical criteria to determine whether there is static or dynamic friction at the contacts. Further, the formalism ought to provide an analytical formula to compute a well-defined and unique direction and magnitude of the static friction force, without e.g. influence of the order of treatment of the particles. Numerical treatment of the formalism should be stable against numerical error and should not rely on numerically problematic concepts, such as determination of the roots of relative velocities, which contains finite errors for for finite timesteps. The algorithm should be able to fix particle configurations at relative rest in a "numerically exact" way, i.e. within the accuracy of the time integration method, leaving only a numerical drift which should be negligible with respect to the other velocities and scales in the system.

We introduce a formalism for dry Coulomb friction for single contact situations, based on the framework of differential algebraic equations (DAE), that provides us with a crite-

rion to distinguish between static and dynamic friction and lets us find the correct value of static friction in the convex hull of the dynamic friction forces. We also provide the necessary adaptions required for use with numerical integrators with constant timesteps. The formalism is then extended for arbitrary many-particle many-contacts situations in two dimensions, and its invariance under change of particle index is shown. We verify our approach in discrete element method simulations (DEM) of several problem geometries with increasing complexity. We compare the results of the formalism with other approaches and investigate the effect of the timestep and the numerical integrator. In addition, we find, that simulations of static granular configurations show permanent noise in the linear degrees of freedom, independent of the friction law we use. This noise is a result from geometrical inconsistencies at the contacts, caused by residual angular motion and can not be compensated by damping in the linear degrees of freedom. Its effect is that of an external excitation and results in the configurations being less stable than they should be. To alleviate this problem, we develop a supplementary damping formalism for the angular degrees of freedom and implement it as a stabilisation into our friction formalism.

Contents

Contents **i**

List of Figures **v**

List of Tables **xv**

1 Phenomenology and theory of Friction **1**

1.1 Purpose of the thesis 2

1.2 Solid friction 4

1.3 The roughness theory of friction 7

1.4 The adhesion theory of friction 8

1.5 Static vs. dynamic friction coefficients 10

1.6 The geometry of friction 12

1.7 Size scales in friction 14

1.8 Organization of the thesis 15

2 Existing models for solid friction **17**

2.1 Viscous and "regularised" models 17

2.2 Cundall-Strack model 18

2.3 Contact dynamics 20

2.4 Formulation as linear complimentary problem 21

2.5 Leine and Nijmeijer 22

2.6 Differential inclusions 23

2.7 Hairer and Wanner 24

2.8 Stribeck friction 24

2.9 Heuristic models 25

3 Granular media as a frictional many-body systems **29**

3.1 Classification of granular materials 29

3.2 Dynamics and interactions between granular particles 32

3.3 Granular solids 33

3.3.1 Elasticity and plasticity 34

3.3.2 Granular heaps 34

3.3.3 History effects in granular media 36

3.3.4 Reynolds dilatancy 36

3.3.5 Forces distribution inside granular assemblies 38

3.4 Granular flow and granular "liquids" 39

3.4.1 Rheology 40

3.4.2 Segregation 42

3.4.3 Liquefaction 43

4 The Discrete Element Method **45**

4.1 Rigid body kinematics in two dimensions 45

4.1.1 Elastic forces in normal direction 47

4.1.2 Dissipative forces in normal direction 48

4.1.3 Tangential forces 50

4.1.4 Total force and torque 50

4.1.5 Threshold for "zero velocity" 50

4.2 Modelling errors 51

4.3 Numerical integration 52

4.3.1 Gear Predictor-Corrector Scheme 52

4.3.2 Choosing the timestep 54

4.4 The discrete element method in three dimensions 54

4.4.1 The elastic force in three dimensions 54

4.4.2 Normal and tangential directions of the force point 56

5 Constraint forces and the character of static friction as a constraint **59**

5.1 Differential algebraic equations 59

5.1.1 Point pendulum 60

5.1.2 Drift away from the constraint 61

5.1.3 Stiffness and time integrator . . . 62
5.1.4 Numerical stabilization of the constraint . . . 65
5.1.5 Inconsistent initial values . . . 65
5.2 The dynamical system . . . 66
5.3 Numerically exact formalism for a single point mass . . . 72
5.3.1 Phase flow for the linear oscillator . . . 72
5.3.2 Identification of static friction . . . 72
5.3.3 Determination of the static friction force . . . 74
5.3.4 Implementation with adaptive step size . . . 76
5.3.5 Painlevé-paradox . . . 76
5.4 Implementation with constant timestep . . . 78
5.4.1 Theoretical and actual loss of precision . . . 79
5.4.2 Threshold for vanishing velocity . . . 79
5.4.3 Zero crossing of the velocity in the next timestep . . . 80
5.4.4 Zero crossing of the velocity from the previous timestep . . . 81
5.4.5 Dealing with residual velocities . . . 81
5.5 Limitation of the uniqueness of the numerical solution . . . 82

6 Generalisation to many particle systems 83
6.1 Effective single particle problem . . . 83
6.1.1 Discrimination between dynamic and static friction . . . 85
6.1.2 Determination of the static friction force . . . 86
6.2 Invariance under index change . . . 86
6.3 Concluding remarks . . . 88
6.4 Extension of the friction formalism to three dimensions . . . 89

7 Validation of the friction law 91
7.1 Computability and stability for granular systems . . . 91
7.1.1 Sound velocity as an observable unaffected by friction . . . 94
7.1.2 Mechanical stability as unmistakable observable . . . 95
7.2 Block leaning on a wall . . . 97
7.3 A block sliding on a slope . . . 98
7.4 Vibrated box . . . 101

7.5 Friction in a heap . . . 103
7.6 Equilibration of particles in a resting box . . . 106

8 Stabilization **109**

8.1 Angular velocity as indicator function . . . 110
8.2 Damping in analogy to the static friction formalism . . . 111
8.3 Treatment for residual angular velocity . . . 113
8.4 Numerical verification . . . 116
8.4.1 Two leaning particles . . . 116
8.4.2 Equilibration of particles in a resting box . . . 118
8.4.3 Revisiting the granular heap . . . 119
8.5 Summary of the rotation damping . . . 120

9 Conclusion **121**

References **123**

List of Figures

1.1 For a block on an inclined slope the static friction force is not given as the dynamic friction force, but as the opposite of the downhill force. 3

1.2 For a system with millions of inclined contacts determining the correct static friction force is a non-trivial task. 3

1.3 Functional dependence of solid friction with dissipative, velocity independent dynamic regime and the range of possible values for static friction, which is not dissipative. 4

1.4 Amplitude decay for a linear oscillator with viscous (grey) and solid (black) friction. Dashed lines indicate the respective envelopes, "exponential" for viscous friction and "linear towards zero" for dry friction. 6

1.5 Cups used in tapping for the sound data in Fig. 1.6. The left one is free of damage, the right one is chipped at the edge and has a crack running down to the bottom of the cup. 6

1.6 Sound amplitudes emitted by the cups in Fig 1.5 when tapped with a spoon. The decay for the intact cup (above) can be fitted well with an exponential envelope. For the decay of the chipped and cracked cup, the data fits better to straight than exponential envelopes. 7

1.7 Roughness theory with sinusoidal surfaces with an external force pulling to the right. a) static friction, b) dynamic friction, and c) asperities pushing in direction of motion. 7

1.8 Surface roughness for a body under smaller load in a) and larger load in b). The effective real contact area is drawn as ellipses below, and the apparent contact area is drawn as rectangles below the ellipses. 9

1.9 Creep under stick-slip motion (frames at 0, 10, 20 and 40 s) of a tripod of assembled nylon cylinders with spherically curved ends on an inclined slope made from polished stainless steel. 12

1.10 Time evolution of the stick slip motion from Fig. 1.9 with an average velocity of $2.6 \cdot 10^{-4}$ m/s. 13

1.11 Sketch of sliding friction where the relative velocity at the contact is the same as the relative velocity of the centres of mass in a), rolling friction where the velocity at the contact is zero and the relative velocity of the centres of mass is finite with an axis of rotation parallel to the contact surface in b), as well as pivoting friction where the axis of rotation perpendicular to the contact surface in c). 13

2.1 Functional dependence of solid friction with dissipative, velocity independent dynamic regime and the range of possible values for static friction (emphasized by dashed line), which is not dissipative at all (a) as well as "regularizations" with viscous friction (b) and zero static friction (c). 18

2.2 Behaviour of static friction for a simple block on a slope. The actual oscillatory behaviour of the Cundall-Strack model is shown in a dashed line, while its cut-off behaviour is shown with a thin black line. The behaviour of the exact friction is shown as thick black line. The delayed grip of the Cundall-Strack model can be seen immediately after the onset of friction. . 19

2.3 Static friction for particles with many contacts leads to static indeterminate problems for the centres of mass. A problem of overdetermined trusses under pulling strain is equivalent to a granular assembly under compressive strain. 22

2.4 The Filippov-solution for ODEs with non-smooth righthand sides is constructed in the convex hull of solutions "from the left" and "solutions from the right". It leads to an accumulation of stable fix points that is suitable to describe mechanical equilibria for static friction. 23

2.5 Dependence of the Stribeck friction on the velocity for a given load. The lubricated surfaces will have a different plateau than the dry friction of the same materials. 25

2.6 Stribeck curve with the different lubrication regime plotted over the Stribeck number (dynamic viscosity $\eta \cdot$ sliding speed v / pressure p), to which the film thickness is more or less proportional. 25

2.7 Influenced by the roughness notion of friction, the Dahl-model tries to replace constraint forces via spring-like bristles on the contact interface. The bristles mimic hysteretic displacement or plastic deformation with oscillatory behaviour, but completely ignore the atomic nature of the surface interactions. 27

3.1 Some examples of granular media. Clockwise from top-left to bottom-left: Flour has approximately same sized grains of $d_{\text{particle}} \sim \mathcal{O}(10\mu\text{m})$, aggregates show no disorder; similarly rice grains have similar sizes $d_{\text{particle}} \sim \mathcal{O}(\text{mm})$), but their aggregates show large disorder in orientation; rocks have some variation in size ($d_{\text{particle}} \sim \mathcal{O}(\text{dm})$), but also a very notable variation in shape; size dispersion can reach large levels in nature($d_{\text{particle}} \gg \mathcal{O}(\text{m})$). . 30

3.2 Sharp-edged rocks due to fracturing (left), stones in a river bed washed smooth by water (right). 31

3.3 Relevant size scales in granular media: a) contacts and particles ($d_{\text{contact}} \lesssim d_{\text{particle}}$), b) representative volume (micro-structure) ($d_{\text{micro}} \gtrsim d_{\text{particle}}$)., c) macro-structure, ($d_{\text{macro}} \gg d_{\text{particle}}$). 31

3.4 Clustering of mustard seeds into stripes in a horizontally vibrated submonolayer. 32

3.5 Sketches for a) fracturing of bigger particles into smaller particles, b) rolling as the preferred method of motion of round particles, c) sliding of elongated particles, and d) interlocking due to irregular shape. 33

3.6 Heap of polyhedral particles built on a tilted polished mirror. Neither the smoothness of the mirror nor its inclination prevent the heap from being stable. 34

3.7 Snapshots of the heap build under the influence of friction a). Then friction is turned off and the heap flows apart b)-d). While the behaviour looks viscous, in contrast to Newtonian fluids, such an assembly can withstand static normal stresses. 35

3.8 Sketch of the pressure distribution inside granular heaps formed in different ways showing the importance of history effects in granular media. In a) the heap is formed by dropping material from the top, the pressure distribution shows a dip in the centre. In b) the material is piled up in layers. The resulting pressure profile is flat. 36

3.9 Particles in a close packing a) occupy a less dense packing b) after the application of external stresses. 37

3.10 Macroscopically, sand drying under the feet, visible as bright spot, on the beach is one of the most well known examples of dilatancy. 37

3.11 Left: Force network within a static granular configuration. Lines represent the normal forces transmitted along discrete contacts. Right: Granular force networks can result in stable arches by redirecting the particle weight into static walls. 38

3.12 Hourglasses show three states of matter for granular media: In the upper part, the particles form a solid, further down, near the orifice, they flow in a liquid-like manner. Past the orifice, the particles fall with little interactions with other particles with a large mean free path, resembling a "gas". In the bottom, on the top, the particles condense into a solid like heap, with regular granular avalanches down the slopes. 39

3.13 Figure a) shows the Bagnold velocity profile for a particle flow down an inclined plane. Figure b) shows the velocity profile for an avalanche sliding down as a single block under the effect of inter-particle static friction. At the interface between the avalanche and the surface a particle layer with $v = 0$ is possible. 41

3.14 Flow profiles: a) Massflow and b) Plugflow with dead zones of immobile particles (marked in beige) 42

3.15 Granular segregation in particle flows, such as rockslides, pushes larger particles to the outsides and the top of rockslides as smaller particles can easily penetrate below larger ones. 43

4.1 Relative movement of a point P computed from another point C for rigid body kinematics. 46

4.2 Contact geometry for two polygonal particles (dark shading), showing their overlap (light shading), the polygons' centres of mass C_a, C_b, the centre of mass of the overlap polygon P and the contact vectors $\boldsymbol{r}_a, \boldsymbol{r}_b$ from C_a, C_b, to P (left). The inset (right) indicates the normal ($\mathbf{n}$) and tangential ($\mathbf{t}$) contact direction, given by the intersection points of the outlines. The overlap is considerably exaggerated compared to the 1/1000 of a linear particle extension for the simulations in this thesis. 48

4.3 Unphysical jumps in the force evolution for the elastic and dissipative force during approach and separation. 49

4.4 In mechanical equilibrium, the forces and torques in a DEM-simulation should be balanced. Residual angular motion can induce small changes in the contact orientation $\Delta\varphi$. As consequence, the contact forces change, equilibrium is no longer maintained and the rectilinear degrees of motion experience noise. 51

4.5 Sketch of the contact geometry between three-dimensional discrete elements, in equivalency to the two-dimensional case in Fig. 4.2. a) Sketch of the contact line (blue) of two intersecting tetrahedra P_a and P_b and the centroid of the overlap tetrahedron C_0. b) Contact area of a different overlap polyhedron, separated into several triangles around the centroid C_0. The normal direction of the overlap area can be determined by the area weighted average of the normal directions of the triangles. 55

4.6 The projection $P(\boldsymbol{a}_{\mathrm{rel}}|\mathcal{T})$ of the relative acceleration $\boldsymbol{a}_{\mathrm{rel}}$ into the contact plane $\mathcal{T}$ is unique, and therefore the direction of the static friction is unique too. 57

5.1 Pendulum with the centre in the origin, with position vector (x, y) and velocity vector $(\dot{x} = v_x, \dot{y} = v_y)$ and the theoretical trajectory (dotted line) as well as an unphysical (due to inconsistent initial values) trajectory (grey, solid line). 60

5.2 Drift Δl for MATLAB's ode23 (above) and respective timestep τ (below) for the radius of the pendulum problem away from $l = 1$ with different tolerances ϵ_{abs} : The integration with the smaller tolerance shows the larger drift. 62

5.3 Drift Δl for MATLAB's ode45 (above) and respective timestep (below) for the radius of the pendulum problem away from $l = 1$ with different tolerances ϵ_{abs} : The integration with the smaller tolerance shows the smaller drift. 63

5.4 Drift $\Delta\alpha$ of the angle between position and velocity vector from 90° for MATLAB's ode23 (above) and ode45 (below) with different error tolerances. 64

5.5 a) The bouncing ball as an example for a problem with multiple timescales. The free-flight parabola b) can be integrated with higher timestep than the linear oscillations during bouncing off the floor c). 64

5.6 Exact constraint (dashed) with stabilization after Baumgarte in a) and velocity projection in b). 66

5.7 Possible attractors for ordinary differential equations in a) to d) and a global flow configuration in e) with one node and two circles. 68

5.8 Phaseflow for the linear oscillator without damping in (a), viscous (velocity dependent) damping in (b), and Coulomb friction in (c). While the flow Φ is continuous in a) and b), it is discontinuous in c). 69

5.9 Velocity (black) and position (blue) for the frictional oscillator with $m = 1, k = 0.1, \mu = 0.2$ with the values taken from[1]. When the kinetic energy is used up and $|kx| < \mu|F^{\mathrm{N}}|$, the velocity reaches zero. 71

5.10 Stationary points for the phase flow at a discontinuity. 71

5.11 Phase flow $\Phi(x, v, t)$ for a linear oscillator with $m = 1$ and $k = 9.81$ in a),with additional viscous damping $\gamma = 0.75$ in b) and with dry friction $\mu F^{\mathrm{N}} = 0.3$ without viscous damping in c). Direction of the flow field indicated by grey unit vectors, particular trajectories by bold lines with the flow direction indicated by an arrow symbols. 73

5.12 Flow Φ in phasespace (directions only, arrows are unit vectors) for a linear oscillator with dry-friction with $m = 0.25$, $k = 1$ and $\mu = 0.2$ near to the $v = 0$-axis. The thick line is an accumulation of stable fix points. 74

5.13 Flow Φ in phase space (directions only, arrows are unit vectors) for inconsistent initial values at $v = 0$ which are typical for Painlevé-paradoxes: A body with $v = 0$ is unphysically pulled either into the region $v > 0$ or $v < 0$ for a friction value $\pm\mu|F^{\mathrm{N}}|$, away from the constraint manifold (thick line between $-\frac{\mu|F^{\mathrm{N}}|}{k}$ to $+\frac{\mu|F^{\mathrm{N}}|}{k}$ at $v = 0$). This type of flow is not a possible flow for ODEs with non-smooth right hand sides in the sense of Filippov[2]. 77

5.14 Implementation of the friction formalism with constant timestep results in a decrease of the timestep near the zero-velocity transition. Stop- and restart procedures for the friction evaluation at every zero-crossing of the velocity lead to a fragmentation of the effective timestep. An implementation with constant timestep is therefore preferred. 78

5.15 Zero crossings of the velocity usually occur between two successive timesteps but rather inbetween a)-b), resulting in spurious finite velocities. In the current timestep, the velocity can also become vanishingly small without a zero-crossing c), likewise leading to non-zero residual velocities. 79

6.1 For many-body contacts, building up the contact matrix and a related "friction space" for each particle as a simplex of frictional constraints in a combinatorial approach to static friction is not feasible: The same constraints allow multiple solutions, the dimension of the solution space increases in combinatorial order. 84

6.2 For a block sliding down a slope, the friction force is the opposite of the downhill force. For a cylinder rolling down a slope, the tangential acceleration is coupled with an angular acceleration. The friction force required to bring the cylinder to a stop is lower than for pure sliding. This is expressed in an additional corrective term in the reduced mass. 85

7.1 Interaction forces for particles before the collision ($F = 0$ to the left of the vertical axis) and for the contacting particles ($F \propto x$ to the right of the vertical axis), for a "linear" force law in a) and a "non-linear" force law in b. The actual non-linearity which affects the particle trajectories during collisions is the variation from $F = 0$ to $F \propto x$ at $x = 0$. 92

7.2 Granular collisions, where minor differences in the initial position may lead to a cascade of different outcomes in the time evolution of particle positions. For the same initial states, vastly different final states are possible with only a tiny change of the initial position. 92

7.3 Binomial scattering of particles into a binomial distribution in the Galton board due to the triangluar set of pins. While the initial condition shows an initially continuous red region, in the final configuration, white particles are scattered between the red ones and vice-versa due to the non-linearity of the interaction. 93

7.4 Linear chain of discrete particles connected with springs. 94

7.5 Reconstruction of the Tingis Gate in Morocco from a building complex in Volubilis, dating from the 3rd century AD. 96

7.6 Simulation of a granular arch without friction (top row) will lead to unphysical collapse. In simulations with Coulomb friction (middle row) the arch will remain stable, but the key stone will be slightly misaligned. In simulations with the DAE friction aproach, the arch will remain stable and well aligned. 96

7.7 Block leaning on a wall with the wall contact with $\mu = 0$ and the floor contact with $\mu = 0.6$. 97

7.8 Creep (stationary velocity) of the centre of mass for the block leaning on a wall in Fig. 7.7 for damping with $a_{\mathrm{dec}}^{(\eta)} = -(\eta v(t)/\tau - a(t))$ for different values of $\eta = 0.5$, 1, 2, 3 and τ. The data from BDF2 are marked with solid lines, the data from BDF5 are marked in dashed lines (practically on top of each other for different values of η). 98

7.9 Creep of the centre of mass for the block leaning on a wall in Fig. 7.7 using the Heun integration scheme for damping with $a_{\mathrm{dec}}^{(\eta)} = -(\eta v(t)/\tau - a(t))$ for different values of $\eta = 1$, 2 and τ. The data from Heun are marked with dashed lines, the reference data from BDF2 are marked in a solid black line. For larger timesteps the Heun method will not be stable. 98

7.10 Block with weight mg, normal force F^{N} and downhill force F^{downhill} on a slope with $\alpha = 15°$. 99

7.11 Height of the block on a slope for different friction approaches, our differential algebraic equation (DAE), Cundall-Strack (CS) with and without damping, the theoretical (constant) value and the dynamic friction (Dyn) value. 100

7.12 The height of the block as in Fig. 7.11 for differential algebraic equation (DAE), Cundall-Strack (CS) with and without damping along the stationary state: For DAE and CS without damping, there is oscillatory (see insets) downhill creep. The trajectories for CS with damping and for dynamic friction (DYN) are without oscillations. The data is scaled with the effective particle radius to indicate the relative accuracy of the different methods. . . 100

7.13 Vibrated box (walls are higher than shown) with DEM-particles. 101

7.14 Centre of mass energy for the system in Fig.7.13: $E_{\text{kin, COM}} = \frac{1}{2}(\sum_i^N m_i)v_{\text{COM}}^2$ with the DAE method (black) and the CS method (gray). 103

7.15 Difference between centre of mass energy and particle energy for the system in Fig.7.13: $E_{\text{kin, diff}} = \sum_i^N \frac{1}{2} m_i (v_{\text{COM}} - v_i)^2$ for the DAE method (black) and the CS method (gray). 103

7.16 Heap with 1622 particles for which the static friction is computed. The rounding of the apex is not due to a failure of the friction law, but due to the scattering of particles in the preliminary simulation in which the initial positions were determined. 103

7.17 Decay of the centre of mass height for the heap in Fig. 7.16 in Sauter diameters with DAE-friction (black) and Cundall-Strack-friction (gray) in the short term with $\tau_1 = 10^{-5}$s. DAE-friction with half the timestep $\tau_2 = 0.5\tau_1$ is shown in a dashed black line. Friction is gripping faster for the DAE method than for the Cundall-Strack model, while for longer times the Cundall-Strack-friction is inherently self-stabilizing. 104

7.18 Decay of the centre of mass height for the heap in Fig. 7.16 in Sauter diameter with DAE-friction (black) and Cundall-Strack-friction (gray). DAE-friction with half the timestep is shown in a dashed black line. For longer time spans the DAE method reaches force equilibrium, so the centre is creeping with constant velocity in accordance with Newton's first law that a system in force equilibrium can propagate at constant velocity. A lower timestep decreases the creep. 104

7.19 Time dependence of the kinetic energy per particle for the heap in Fig. 7.16 with DAE-friction (black) and Cundall-Strack-friction (gray). 105

7.20 With the Cundall-Strack model, the particle is embedded in a spring network, leading to persistent lattice vibrations. Residual rotational energy can be dissipated through damped oscillations in tangential direction. . . . 105

7.21 Unphysically stagnating mean kinetic energy for particles in a resting box, instead of the expected viscous or dry-friction decay. Spikes indicate sudden reordering of the configuration. 106

7.22 If the rotational degrees of freedom are (unphysically) disabled at 2.5 seconds, the energy decay meets physical expectations and decays towards zero (blue line). In addition, the system shows much less reordering than with physical rotation allowed (black line). 107

8.1 Residual rotation will lead to small changes in the contact orientation $\Delta\varphi$, and possibly unbalanced forces, inducing additional noise in the rectilinear degrees of freedom. 109

8.2 The rotation of a particle within other particles is influenced by the motion of the whole surrounding granular matrix rotation, which for rigid body rotation of the surrounding granular matrix can be expressed with an angular velocity ω_0. 111

8.3 Two particles leaning onto each other in an unstable equilibrium. 116

8.4 Oscillations in the two particle configuration decay faster for the damped case (black) than for the undamped case (blue) but remain slightly stronger in the long term. 117

8.5 The horizontal component in the centre of mass coordinates of the two particle problem deviates strongly from its initial position in the undamped case (blue), while the damped case (black) is essentially stable. 117

8.6 Oscillations in the vertical component of the centre of mass coordinates of the two particle problem are stronger in systems with rotation damping (blue) than in systems without (black), but the order of magnitude is the same in both cases. 117

8.7 The mean kinetic energy for the equilibrating particle configuration in a resting box shows is stagnating at high magnitude, with many large energy spikes from reordering of the particle configuration (blue line). With rotation damping, the transfer of energy into the rectilinear degrees of freedom is inhibited, and the kinetic energy in the stable state becomes zero (black line). The simulations were restarted with configurations from previous simulations. 118

8.8 As the rotation damping prevents additional noise in the rectilinear degrees of freedom, the drift in the centre of mass height can be exactly compensated, and the configuration will be stable (black line), compared with the non-stabilized solution (blue line). 118

8.9 Compared to the undamped approach (blue line) with a vertical centre of mass drift of about 10% of the mean particle diameter, the result of the stabilized formalism is perfectly stable (black line). 119

8.10 With rotational damping, the residual kinetic energy for the heap configuration in mechanical equilibrium is zero, as the centre of mass drift is perfectly compensated (black line), whereas the unstabilized configuration shows an unphysically stagnating kinetic energy with random fluctuations (blue line). 119

List of Tables

4.1 Gear corrector coefficients for second order differential equations with velocity dependent forces of order two to five. 53

4.2 Evolution of the force law and the parameters from the one-dimensional linear oscillator to the force law for two- and three-dimensional discrete elements. 55

6.1 Comparison between the variables for the friction formalism in one-, two-, and three dimensions. 90

7.1 Parameters for the interaction computation of 1m-long rod like particles. . . 91

8.1 Comparison of the static friction formalism and the rotation damping formalism in analogy to the static friction formalism. 115

Chapter 1

Phenomenology and theory of Friction

The basic principles of friction, like the dependency on the load, are taught in school. Unfortunately, many of them, like the roughness explanation or the larger magnitude of the static than of the dynamic coefficients of friction are outdated, misleading or simply wrong from todays research perspective. Developments in the field of tribology have gone unnoticed even in a larger scientific community and misunderstandings from the past are still being promulgated in contemporary courses and textbooks. This chapter gives an overview over some fundamental concepts of friction, in particular solid friction with application to granular materials. Proper understanding of friction allows to formulate criteria to judge the relevance of simulations and to deepen the understanding of other effects such as the role of disorder in granular systems.

The study of dry friction began with Leonardo da Vinci, more than 500 years ago. It is not clear from his works[3], if he did actual experiments or only thought experiments. However, as he wrote his conclusions into his personal notebooks, they did not have much impact on science and engineering of his time. It was only with Guillaume Amontons studies published in 1699[4] that the science of dry friction became the topic of public discussion. He formulated four "laws of friction" which now for the basis of the solid friction laws, also called Coulomb- or Coulomb-Amontons friction laws:
– Friction is proportional to the applied pressure,
– The resistance caused by friction is the same for different materials, as long as they are lubricated with grease,
– The resistance is roughly equal to one-third of the pressure,
– The resistance does not depend on the velocity and other conditions.
His explanations on the nature of friction were rough: Insufficient understanding of the microscopic nature of surfaces during his time meant, his laws could describe reality quantitatively, but became incorrect once more detailed information was required. Whereas Amontons dealt with greased surfaces, at the of the 18th century Charles-Augustine de

Coulomb begun to study "dry" surfaces. He systematically studied the dependency of solid friction on many factors, such as materials of the contacting bodies, surface conditions or contact area, and formulated the friction laws as they are still known today. Coulombs explanations for the friction phenomenon are usually referred to as "roughness hypothesis". Alternative explanations, such as the dependence of friction on adhesion between contacting surfaces, as demonstrated in experiments by Desagulier or Trievall were rejected as they were contrary to the microscopical understanding of their time. In the middle of the 20th century, the advent of new technologies such as microscopy or vacuum chambers allowed study and manipulation of surfaces on the atomic scale, which gave way to new approaches. Regrettably, the results of modern tribology (since the 1950s) are often ignored in the fields of mechanics and physics, and misconceptions from the past remain. For more detailed overviews on the history of friction, general introductions can be found in Dowson[5], Persson[6], Popov[7] and information on special topics in Gillmor[8], Hutchings[3] and Popova and Popov[9].

1.1 Purpose of the thesis

For a block with mass m and friction coefficient μ at rest on an inclined slope with angle α, as in Fig. 1.1, we can easily determine the static friction force. If the $\arctan(\alpha) < \mu$ and the normal force F^{N} is known, then we can compute an unique value for static friction as $F^{\mathrm{fric,stat}} = mg\sin(\alpha)$, the opposite of the downhill force. It is not possible to take the value of the dynamic friction force, $F^{\mathrm{fric,dyn}} = \mu F^{\mathrm{N}}$ because the block would creep the slope uphill.

In a heap of sand, such as in Fig. 1.2, we have thousands to millions of inclined contacts. Since the time of Coulomb, many attempts have been made to provide a friction formalism for many-body static friction, but they all fall short as they either have problems with physicality or are not applicable to problems with multiple contacts or in higher dimension.

The main objective of this thesis is to give a mathematically justifiable exact derivation of the conditions and magnitude of a multi-body static friction force in higher dimensions as a reaction to prescribed normal forces and friction coefficients. The solution should be well-defined, that is, the static friction force needs to be unique. Further, the formalism should be usable in numerical calculation methods with finite timesteps with no ad-hoc assumptions, consistent with the framework of numerical analysis.

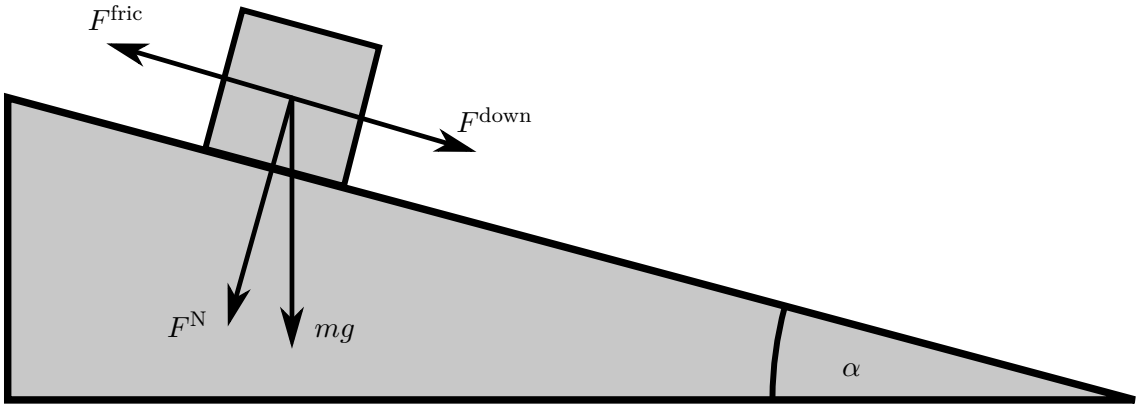

Fig. 1.1 For a block on an inclined slope the static friction force is not given as the dynamic friction force, but as the opposite of the downhill force.

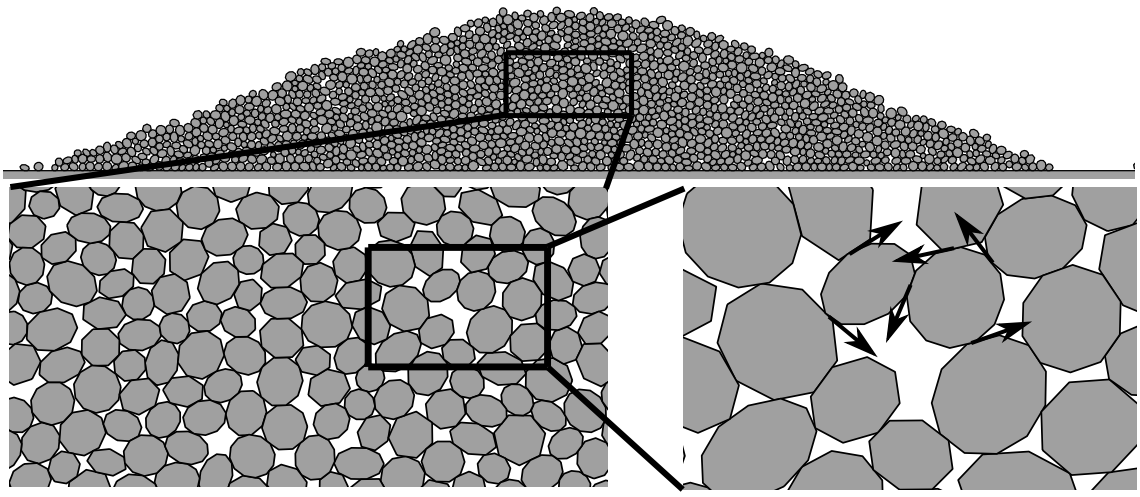

Fig. 1.2 For a system with millions of inclined contacts determining the correct static friction force is a non-trivial task.

1.2 Solid friction

Solid friction has hardly any dependence on the velocity v, is proportional to the normal load F^{N}, and the friction coefficient μ depends on the materials in contact. That sliding friction (in one dimension)

$$F^{\mathrm{fri}}_{\mathrm{sli}} = -\mu |F^{\mathrm{N}}| \mathrm{sign}(v) \tag{1.1}$$

is proportional to the normal force and the friction coefficient. We speak of "friction" when the contacting surfaces stay intact. Abrasion, gouging, ploughing or deposition from one surface to the other[1] all change the surface structure; they are called "wear" in this context. Usual friction coefficients are of the order of 1, see e.g. [10] and the tables therein, so friction can not be treated as a "small perturbation" in mechanics. For most materials, μ varies between 0.1 to 0.8, while for teflon-metal contacts $\mu = 0.01$ is reported, and for large loads or pure metal surfaces in vacuum the friction coefficient may even exceed 1.

Static friction (at $v = 0$) can not be formulated as an equation like eq. (1.1), but only with a relation as inequality

$$-\mu |F^{\mathrm{N}}| \le F^{\mathrm{fri}}_{\mathrm{stat}} \le +\mu |F^{\mathrm{N}}|. \tag{1.2}$$

For an object on the ground without any external forces, the friction acting on the ground will be zero. Pushing or pulling weak enough so that the object does not begin to move will result in non-zero friction. This means the static friction can be considerably smaller than the dynamic friction in eq. (1.1). Static friction is not a dissipative force, because the work integral $W = \int F^{\mathrm{fri}}_{\mathrm{stat}} \mathrm{d}x$ vanishes together with $\int \mathrm{d}x = 0$. Static friction is among the class of constraint problems, whose treatment is missing in many elementary engineering and science courses. So $F^{\mathrm{fri}}_{\mathrm{stat}}$ can only be determined from the external forces acting on a body: As long as the body does not move, its motion is constrained and the

[1] e.g. chalk on a blackboard

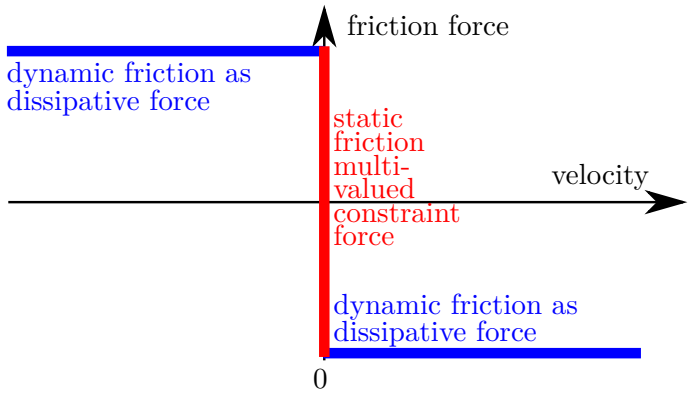

Fig. 1.3 Functional dependence of solid friction with dissipative, velocity independent dynamic regime and the range of possible values for static friction, which is not dissipative.

friction force is exactly the opposite of the external force. Position constraints between bodies cannot be modelled by velocity dependencies or inner degrees of freedom: They are a function of the relative accelerations at the contact point. For the velocity near zero, the jump in eq. (1.2) at least formally necessitates a treatment in the framework of ordinary differential equations with discontinuous right-hand sides pioneered by Filippov[2]. For problems with more bodies, when one erroneously implies dynamic friction instead of static friction, one often ends up with friction forces and velocities in the same direction. For such "Painlevé Paradoxes" (see section 5.3.5 below for a detailed explanation) the systems would in fact not move at all under the influence of too small external forces, static friction would enforce static behaviour. It is the erroneous assumption of motion, which implies a friction magnitude of $-\mu|F^{\mathrm{N}}|$, which creates the "paradox", neglecting that for a static configuration in eq. (1.2), the magnitude of the friction force has no lower bound. The static friction force is then a constraint force, and the exact computation of initial values can be rather cumbersome, requiring the solution of non-linear equations to avoid what is called "inconsistent initial values" in the field of Differential Algebraic Equations, see Hairer and Wanner[1] .

The understanding of solid friction has been mired due to confusion with friction laws for bodies in fluids which are always dissipative. Viscous friction $\propto v$ for slow (Stokes) flow can easily be treated in mechanics courses. Newton friction $\propto v^2$ occurs in inertia dominated flows (with vortices) and is analytically rather inconvenient to deal with due to the resulting non-linear equations. Nevertheless, at least for the case of $v \to 0$, it is clear that fluid friction vanishes. For a linear oscillator

$$ma + kx = 0, \tag{1.3}$$

the behaviour under different kinds of friction changes significantly. With a viscous, i.e. velocity-proportional damping

$$F^{\mathrm{damp}} = -\gamma\sqrt{km}v, \tag{1.4}$$

the energy will decay exponentially $\propto \exp\left(-\gamma\sqrt{k/2m}\right)$ (for $\gamma\sqrt{k/2m} < k/m$), but never reach zero. If instead a solid friction term is used

$$F^{\mathrm{fric}} = -\mu mg\,\mathrm{sign}(v) \tag{1.5}$$

(with a normal force mg), the amplitude goes to zero in a linear envelope and the energy becomes zero in finite time, see Fig. 1.4 for a linear oscillator with $m = 1, k = 1$, and for viscous damping with $\gamma = 0.3, \mu = 0.0$ (grey) and for dry friction damping with $\gamma = 0.0, g = 10, \mu = 0.3$ (black). For dry friction, the oscillation terminates before $t = 16$, for viscous friction in principle it continues into infinity. Analytical solutions for viscous and dry friction damping can be found in [11], chapter 8. The exact treatment of dry friction for $v = 0$ is mathematically rather tedious due to the non-smooth right hand

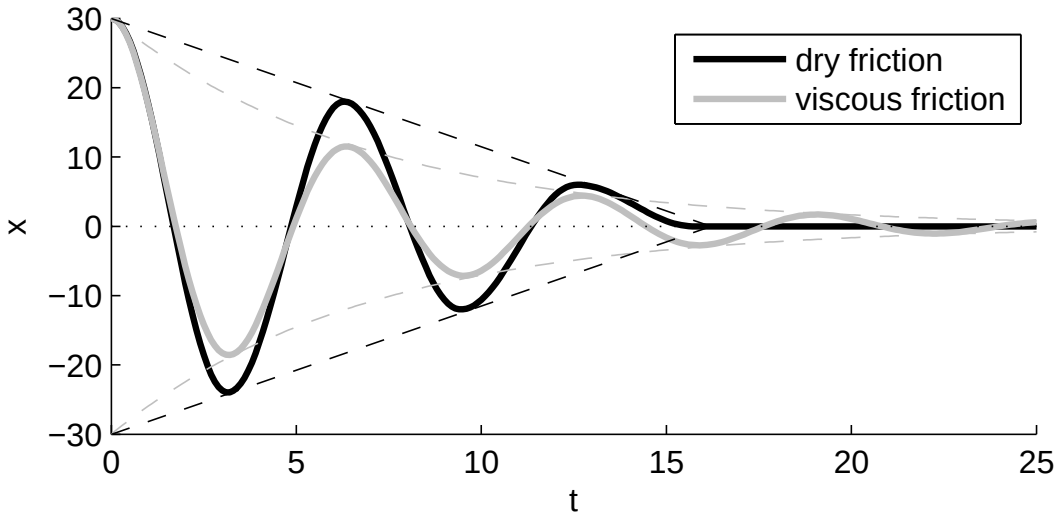

Fig. 1.4 Amplitude decay for a linear oscillator with viscous (grey) and solid (black) friction. Dashed lines indicate the respective envelopes, "exponential" for viscous friction and "linear towards zero" for dry friction.

sides, and will be treated in chapters 5 and 6.

The "faster" action of solid friction can be used to detect cracks in work pieces: Where an intact body would react with a decaying, drawn out singing sound when tapped, a cracked body emits only a short clank, because the surfaces in the crack are in contact under the influence of solid friction, which damps out the vibration much faster than the intact bulk would. For the cups in Fig. 1.5, the sound envelope in Fig. 1.6 for the cracked cup (below) follows a straight line better than the exponential which is suitable for the intact cup (above) with a four times longer decay. For this reason, it makes no sense to try to fit the dissipation of aggregates of frictional particles to properties of elasto-viscous solids: When the external forces become large, even if huge damping constants are chosen, the decay rates for the vibration or wave-propagation would not be the same.

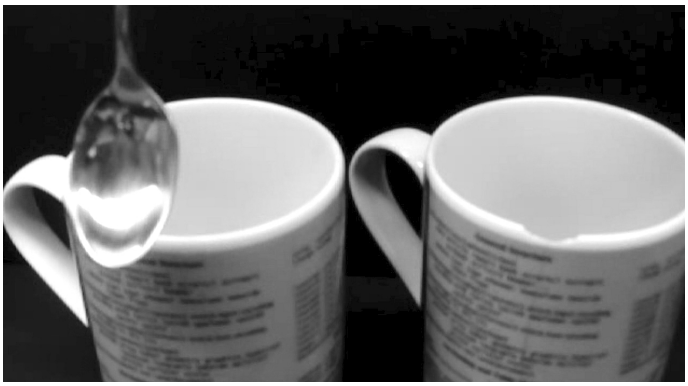

Fig. 1.5 Cups used in tapping for the sound data in Fig. 1.6. The left one is free of damage, the right one is chipped at the edge and has a crack running down to the bottom of the cup.

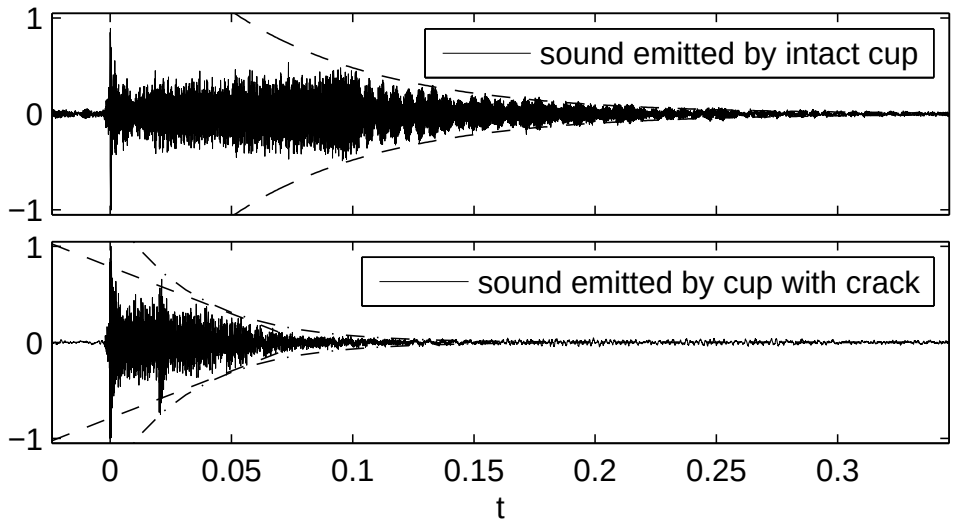

Fig. 1.6 Sound amplitudes emitted by the cups in Fig 1.5 when tapped with a spoon. The decay for the intact cup (above) can be fitted well with an exponential envelope. For the decay of the chipped and cracked cup, the data fits better to straight than exponential envelopes.

1.3 The roughness theory of friction

From the very beginning roughness had been discussed as a possible mechanism for friction, e.g. [12]. Interlocking of surface asperities allowed to describe friction as proportional to the load, but independent of the contact area. However this approach was already criticised by Coulomb[13] in 1809, where he gave a drawing of two blocks of wood with interlocking sinusoidal surfaces, see Fig. 1.7. While this looks like an explanation of static friction via interlocking and dynamic friction as resistance against the up-movement, possible down movement would result in a force in the direction of the movement (Fig. 1.7c), which contradicts the observation that friction always acts against the direction of velocities and external forces. One may try to save the roughness theory by introducing ad hoc

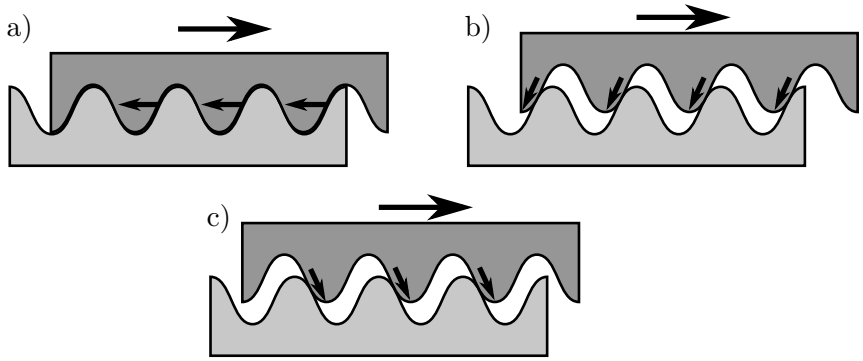

Fig. 1.7 Roughness theory with sinusoidal surfaces with an external force pulling to the right. a) static friction, b) dynamic friction, and c) asperities pushing in direction of motion.

asymmetries between up- and down-movement, but that leads to inconsistencies elsewhere. Surface asperities which lead to contact angles with sines of the order of 1 would be clearly visible on polished, optically smooth, surfaces like mirrors. Other indicators that roughness has not been important on the experimental side are that Amontons considered greased surfaces and that many tables for friction coefficients make no difference between surfaces which are polished and those which have been machined in another way. This may sound unintuitive in granular aggregates, where smooth round particles like glass beads or marbles show less bulk material strength than rougher and irregularly shaped beads or stones of the same size, but that is not an effect of sliding friction alone. Smooth, round shapes allow reorientation and displacement by rolling which is not possible for irregular shapes, and the related rolling friction is considerably weaker than sliding friction.

1.4 The adhesion theory of friction

Triboelectricity was an indicator that phenomena related to friction were not purely mechanical. From 1725 onward, Desagulier elaborated experiments which were originally conceived by Trievall[8], with lead spheres which were fused by pressing them together in a twisting motion[2]. The force needed to separate the spheres to overcome the adhesion was higher than the weight of the spheres. This was not only a demonstration of adhesion, but also (in tangential direction) for adhesion based friction. Friction is different from bulk material properties which may show a considerable proportionality over several orders of magnitude: The Young's modulus correlates with the yield strength ([15], Fig. 2.8f), the (measured) bulk modulus ([16], Fig. 5.9), and the melting point ([15], Fig. 2.11) ([16], Fig. 5.8), the yield strength correlates with the hardness ([15], Fig. 2.10), but none of these properties correlate with the friction coefficient ([16], Fig. 3.3). All coefficients of sliding friction obtained under laboratory conditions and atmospheres are between 0.1 and 1, while relatively large friction coefficients ($\mu \gtrapprox 0.8$) can be obtained on contacts with relatively soft (e.g. rubber), as well as very hard materials (SiC)[17]. This indicates that the mechanisms of friction on the surface are different than the interactions which determine the strength inside the bulk of the material. The understanding of quantum mechanical electron interactions and its consequences for chemistry and solid state properties paved the way for a new understanding of matter from the 1930s onwards. During that time, advances in technology allowed to control laboratory atmospheres sufficiently enough to perform experiments with surfaces with exactly the desired surface chemistry. Control of the surface chemistry became possible via vacuum or gas mixtures so that the metal surfaces in the experiments would not be affected by oxidation or adsorption of water molecules from the surrounding laboratory atmosphere. Additionally measurement accuracy for the forces increased together with the precision in optical methods (microscopy, interferometry) to actually control and quantify the roughness of the surfaces. This devel-

[2] A reproduction of Desaguliers figures can be found in [14].

opment was pioneered by Bowden and Tabor[18, 19, 20]. For the actual effect of roughness, Bailey and Courtney-Pratt in 1955 showed results with friction coefficients $\mu = 8$ between atomically smooth mica surfaces, i.e. one order of magnitude larger than ordinary friction coefficients [21, 22]. The only possible explanation was that the friction was mediated by surface electrons, i.e. adhesion, and roughness of conventional surfaces was in fact reducing the amount of contacting surface electrons. This means that smoother than "technical" surfaces give higher coefficients of sliding friction ([15], Fig. 4.14). Now the idea of roughness needed to be visited again, but with the reasoning reversed: Friction is mediated by surface electrons, and smoother surfaces allow the contact of more electrons between the surfaces. This also explains why friction depends on the load $\mu|F^{\mathrm{N}}|$: The actual area determines the bonds between the surface electrons of the bodies in contact, independent of the apparent area where the bodies only overlap, see Fig. 1.8.

Very strong adhesion and material transfer was observed between metal-crystal, see [22] chapter 7, and metal-graphite surfaces, [22] p. 349, with friction coefficients comparable to that (or higher than) for metal-metal surfaces: This indicates that the character of the interaction is not the same as the chemical bonds in the bulk (ion, metal, covalent and hydrogen bonds), but that there is a genuine electron interaction between the "unemployed" electrons on material surfaces. Local spots can reach elevated temperatures by frictional heating and interdiffusion of surface electrons can result in local compound formation in the surface layers.

The coefficient of friction is actually proportional to the adhesion, see [15] for a discussion in terms of adhesion energy. Various experiments which give contradictory results and a surprising variation of the coefficient of friction for similar pairs of materials are due to the different strength of the adhesion. It is therefore the affinity of the surface electrons which is responsible for the friction, see [15] Fig. 2.22ff with diagrams of various metal pairs. For some material pairs, like aluminium on iron, which have a bad electron affinity, [15] Fig. 4.6, the friction coefficient is independent of the load. For material pairs with good electron affinity, like aluminium on aluminium, [15] Fig. 4.9, the friction coefficient may actually quadruple with the increase of the load: While this is difficult to explain with the roughness theory, it is clear from the point of the adhesion theory. A higher load brings more surface electrons into contact, but only if these electrons have a reasonable

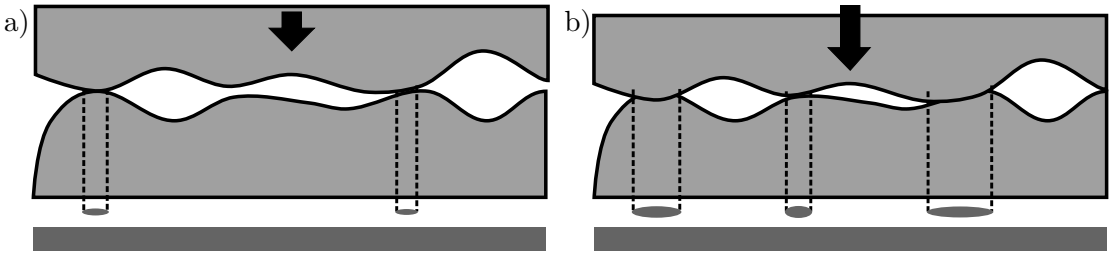

Fig. 1.8 Surface roughness for a body under smaller load in a) and larger load in b). The effective real contact area is drawn as ellipses below, and the apparent contact area is drawn as rectangles below the ellipses.

affinity to form chemical bonds. While roughness is not the cause of friction, asperities on the surface nevertheless play a role: They are the reason why the friction force is not exactly opposite to the sliding direction, but a variation of up to 2 angular degrees is possible, [15] Fig. 4.4. It should also be mentioned that some metals are "greased" by their oxides, i.e. the friction for surfaces is reduced (e.g. for Pb, Sn, Al), where the oxide is harder than the metal itself, but not for other metals where the oxide layer is softer (e.g. Ni,Nb,Co,Cu), [15] Fig. 2.25.

1.5 Static vs. dynamic friction coefficients

A common (and rather insincere) way in lectures to "prove" that static friction coefficients are larger than dynamic friction coefficients is to use brute force: Violently jerking a block forward with a force gauge, and when the gauge flicks back after the initial acceleration into equilibrium position this serves as a "demonstration" that the coefficient for static friction is higher than the coefficient for dynamic friction. Of equally dubious nature is to define the first value obtained during an experiment as the static friction value, before surface asperities or contaminant layers have worn off[23]. Unintended data contamination can occur due to the oscillatory response if the apparatus is not stiff enough. Experiments in the framework of the adhesion theory of friction under controlled atmospheres (vacuum, inert gases, vanishing air humidity) suggest that the static and dynamic coefficients of friction are the same, as long as surface chemistry and geometry do not change[15, 24, 18]. On the other hand, in the presence of air humidity or other gases which modify the surface, the friction increases, albeit weakly, with the time of stick as

$$F_{\mathrm{stat}}^{\mathrm{fri}} = F_0 + kt^{1/10} \tag{1.6}$$

([15], Fig. 4.10). Further dependencies are given in [25]. Tribology handbooks tend to give only one coefficient of friction for most material pairs, see for example [10]. More traditional tables give a static and a (lower) dynamic friction coefficient, e.g. [26], but the data is usually compiled from different sources, without guarantee that the material pairs were exactly the same. Of course, other changes of the surface chemistry like rusting or corrosion, or reordering (like for rubber or gel) will also lead to an increase of the friction force over time, and this will also affect adhesion.

Additionally to the time-dependence of static friction, there is a velocity-dependence for dynamic friction which is not covered by eqs. (1.1, 1.2). In general, the friction decays slowly with the velocity as

$$F_{\mathrm{sli}}^{\mathrm{fri}} = cv^{-1/10}, \tag{1.7}$$

as given by [15] Fig. 4.11. This also runs contrary to any mechanical "roughness" explanation, because higher velocities imply higher deformation rates and therefore an increase in friction, not a decay. From the point of the adhesion theory, there is no big problem.

The "grip" of the electrons is much faster than any mechanical movement or deformation of the surface: This is not the mechanical timescale for friction, for faster sliding velocities, the surfaces will be in stronger vibration with contacts being closed and released.

For some polymers, the coefficient of static friction can be smaller than the dynamic coefficient of friction. Only for polymers[10] lists two different coefficients of friction, with the dynamic coefficient of friction consistently larger or at least as large as the static coefficient of friction. In this case, a block intermittently creeps down a slope. For the tripod shown in Fig. 1.9 slow stick-slip motion occurred for angles $10^\circ \leq \alpha \leq 12^\circ$. Below these angles, the tripod was at rest, and above continuous, accelerated sliding was observed. The stick-slip is not reproducible, for each repetition of the experiment the tripod will stop or accelerate at different positions of the slope. Small vibrations have practically no effect on the sliding speed. The α translate into a range of static friction coefficients of $0.18 \leq \mu \leq 0.21$, which is in the lower range compared with the literature values for nylon on steel [10, p. 73] which nevertheless lists *dynamic* friction coefficients $0.25 - 0.32$, which are mostly higher than static friction coefficients for the same material pair. When the angle of the slop is below 10°, the system reverts to "ordinary" static friction. (For the glass surface of a mirror, the creep of the nylon tripod could be observed at even higher angles.)

Neither the stick-slip in the experiment nor the tabulated values can be explained by a roughness theory. This stick-slip happens because, pedantically speaking, most polymers are not proper solids. This is already obvious from the fact that many polymers will show negative thermal expansion, but they will contract when heated, due to entropic reasons. One can assume that the polymer chains have sufficient freedom to reorder near the surface so that the bonds with the opposite material can be broken due to thermodynamical fluctuations. At least there is no contradiction to the experimental reality, when we put the experiment in the freezer, the creep was slowed down. Nevertheless, this may not necessarily indicate temperature-dependent thermal activation, but it can also be an effect of the lower air humidity: visible condensation on the steel surface speeded up the creep. The weird friction behaviour of polymers brings us to the question: When is a solid a solid, so it can exhibit Coulomb friction? In nanotechnology, electron force microscopy allows to trace Coulomb friction for solid surfaces down to the length scale of nm for "proper" solids. Glass is, pedantically speaking, a fluid with infinite viscosity, it has not undergone a fluid-solid transition like crystals do, the atoms are only frozen in their position. Nevertheless, glass exhibits solid friction, because the atoms are fixed in their relative positions (different from polymers, where the macromolecules can reorder), so this seems to be the decisive criterion. Accordingly, ceramics which are mixtures of glasses and crystals also exhibit solid friction. So the character of friction is not determined by the size of the particles only: There may be macromolecules which are larger than some grains in nano-powders, but the grains will behave like a solid, e.g. form heaps (because their atoms are in fixed positions relative to each other), while the macromolecules won't.

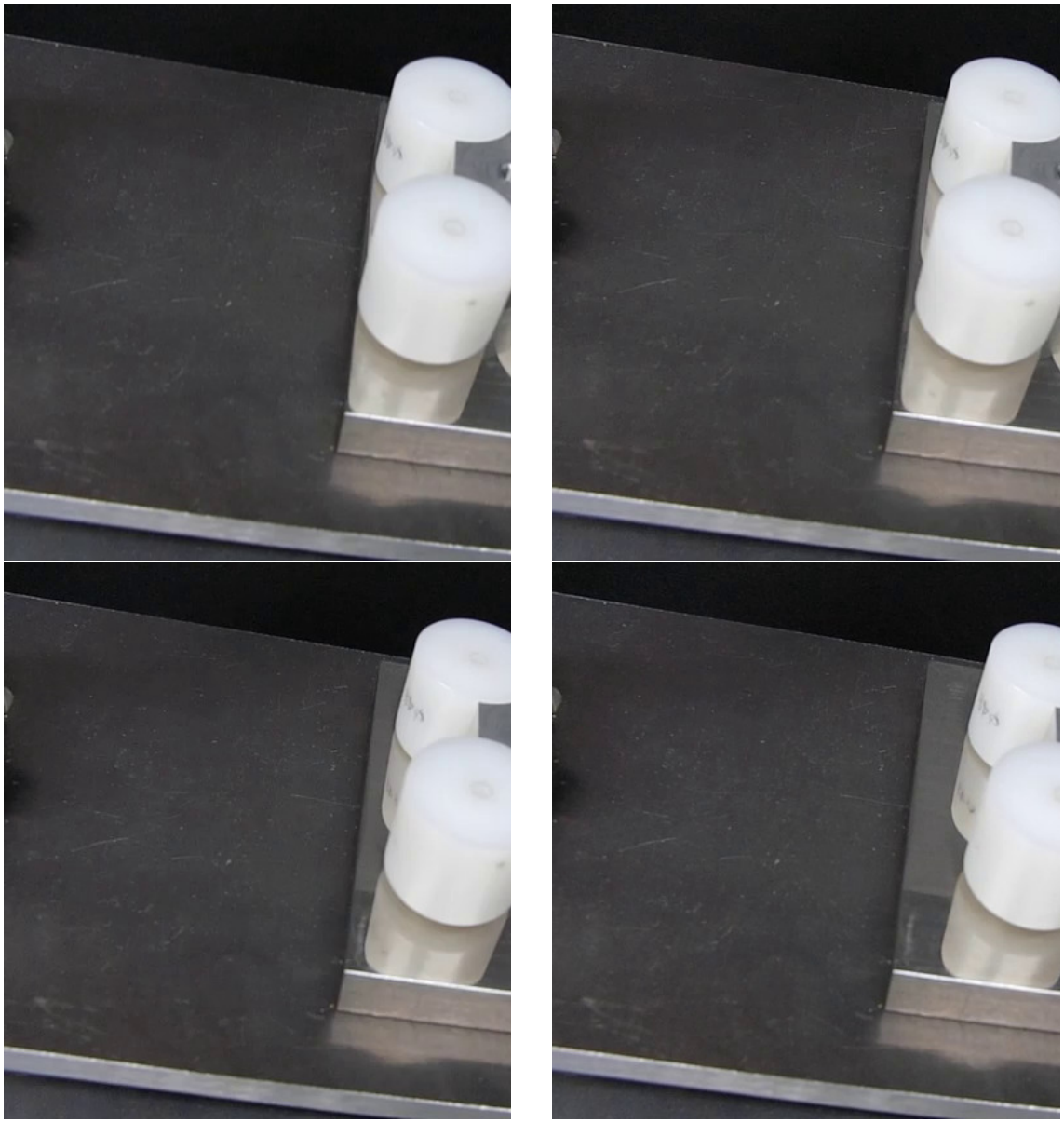

Fig. 1.9 Creep under stick-slip motion (frames at 0, 10, 20 and 40 s) of a tripod of assembled nylon cylinders with spherically curved ends on an inclined slope made from polished stainless steel.

1.6 The geometry of friction

The mechanisms of adhesion described above in the section on "The adhesion theory of friction" lead to the functional description of the Coulomb friction law via eqs. (1.1,1.2). Nevertheless, sliding friction, as in Fig. 1.11 a), is not the only relative motion of solid surfaces. Rolling friction, see Fig. 1.11 b), was already discriminated from sliding friction in Leonardo da Vinci's Codex Madrid [3]. If the rotation axis is perpendicular to the contact area, then pivoting (or drilling or boring) friction is acting, see Fig. 1.11 c). On top of that, these three kinds of friction may occur in combination. All three can exist as static or dynamic friction and have the same functional dependence as in eq. (1.1,1.2), for

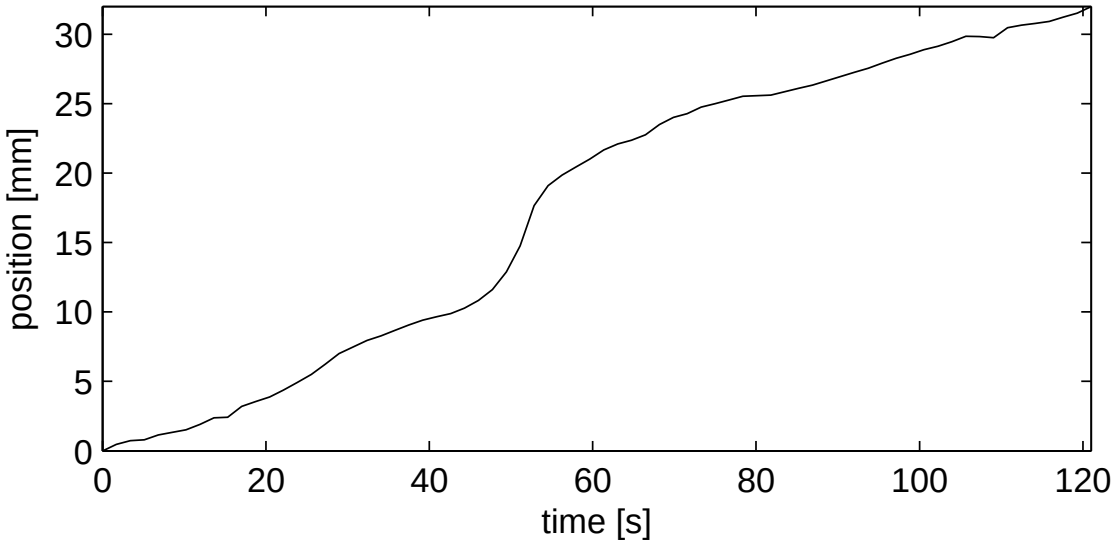

Fig. 1.10 Time evolution of the stick slip motion from Fig. 1.9 with an average velocity of $2.6 \cdot 10^{-4}$ m/s.

rolling and sliding with radii, or with torques. In terms of maximal dissipation, sliding friction is the strongest, followed by drilling and finally rolling. Rolling friction coefficients in dimensionless units range from the order of 0.03 (large value for car tyres) over 0.01 for spheres and cylindrical objects down to 0.001 [10], one to two orders less than for sliding friction. Pivoting friction is rarely treated. The values of the coefficient depend much more than for sliding or rolling on the surface at the contact area and there is further an influence by the surface curvature due to the distribution of the load and the roughness: Rougher surfaces lead to a stronger influence on contact regions further from the rotation axis. Worst of all, the detailed preparation of the surfaces influences the result. On surfaces of steel or duralmin (which were smooth for the eye but had been prepared by rotary machining tools) with pivoting hemispheres made of various materials (nylon, chrome, stainless steel) deviations of more than 30% for clockwise and counter-clockwise rotation were found. This is a much larger than what one expects for sliding contacts in different

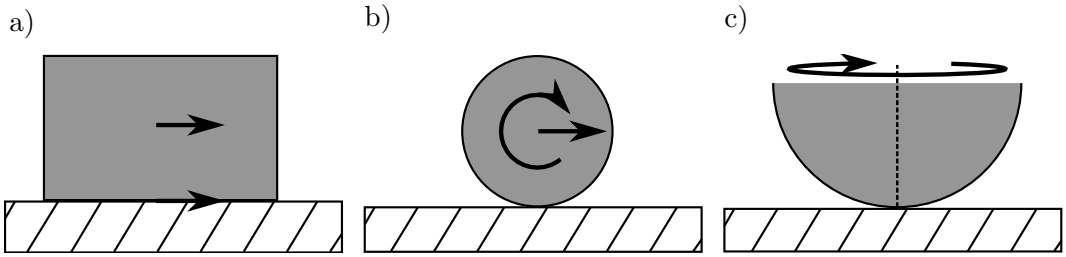

Fig. 1.11 Sketch of sliding friction where the relative velocity at the contact is the same as the relative velocity of the centres of mass in a), rolling friction where the velocity at the contact is zero and the relative velocity of the centres of mass is finite with an axis of rotation parallel to the contact surface in b), as well as pivoting friction where the axis of rotation perpendicular to the contact surface in c).

directions, or what we obtained for the sliding coefficients of friction for the same pairings. Only with polishing the machined steel and duralmin, the deviation could be reduced, but the experimental inaccuracies were still so disheartening large that the experiments were discontinued. There is no claim that better experiments are impossible, but that for freely moving bodies like sand grains or stones, the pivoting component is practically not controllable. The disorder effects will dominate and a tabulation of coefficients is futile. Moreover, the rougher the surfaces become, the larger the effect of interlocking will be, until the surface geometry and wear will have a larger effect than the actual friction.

1.7 Size scales in friction

In "More is different"[27], Anderson philosophized about the hierarchical structures in physics, how the scaling up in size introduces new effects and concepts. This thinking about emergence of phenomena with increases in size is also useful when one considers friction. Temperature does not exist for single electrons, but comes into play for atoms by the Arrhenius law. Coulomb friction does not exist for atoms and molecules in gases and fluids, only for solids. So for different size scales, we have to be aware that different aspects in frictional behaviour will play a role. Moreover, different disciplines will also have different focus due to other conditions. Mechanical engineers as a rule have very good control about the experimental conditions and materials, because mechanical engineering and material science were made so that e.g. stainless steel has quantitatively predictable behaviour. In rock mechanics, on the other hand, practitioners have to make do with the materials "at hand", even if the granite they want to deal with turns out rather porphyric in a geological formation.

The boom in Nanotechnology has boosted the interest in adhesion and friction tremendously, because with decreasing length scales, their relative strength increases, up to the point where mechanisms become inoperative when they are miniaturized. Worse, substances which act as lubricants in the macroscopic world may increase friction in the scale of micro-motors [28, Fig. 16]. So some things change, others stay the same, like the existence of load-displacement-curves [28, Fig. 18].

Friction can still be described by friction coefficients, but the preparation of the surface has a huge influence: When in vacuum, metals with "ordinary surfaces" retain their "everyday-"coefficients of friction between $\mu = 0.4$ and $\mu = 0.6$, for sputter-cleaned surfaces, the friction coefficient increase by up to a factor of nearly 3 [29, Fig. 1.5]. For the visualization of atoms, respectively atomic orbitals, the envelope of theoretically computed (accumulated) electron densities can be used, while for nano-surfaces, the potential minimum of the surface electrons is more meaningful [30, p. 493 and references therein]. Nevertheless, there is a potential barrier which must be overcome in the normal load for "optimal" overlap of electron orbitals: Accordingly, in the nano-world, the friction coefficients decrease with the load [29, Fig. 1.9] when the electrons are too far away from the

potential minimum. Surface roughness can be measured with an accuracy below 1 nm: [28, Fig. 12]. On the other hand, when one can start measuring length scales below 1 nm, atomically smooth surface in the nano world become measurable as hills and valleys of the atomic potentials [31, Fig. 4], so sometimes computer simulations become necessary to understand what one has actually measured.

1.8 Organization of the thesis

In this chapter, we have outlined the basic phenomenology of friction as far as it is relevant for many-particle systems. In chapter 2, we will discuss the sense and non-sense of existing models for solid friction, from regularizations to formalisms based on rigid bodies and dynamical systems. Chapter 3 gives a brief description of the phenomenology of granular media as an example of frictional many-body systems and how their static and dynamic behaviour is related to Coulomb friction. Chapter 4 introduces the basics of the discrete element method in two and three dimensions, which is required for the later implementation of the static friction formalism into simulations of granular particles. It further discusses stability issues arising from the geometrical models. In chapter 5 we introduce the formalism of differential algebraic equations as the language of constraint problems like our case of static friction. We outline our static friction approach for a single contact in a fixed coordinate system and describe the necessary adaptations for numerical implementation. The extension of the formalism from fixed coordinate systems to translational invariant coordinate systems and the adaptation to many-body many-contact situations are discussed in chapter 6. In chapter 7 the friction formalism is applied to several problems and the results compared with other friction approaches. We examine numerical inconsistencies from the geometrical modelling in chapter 8 and outline a novel damping formalism for the rotational degrees of freedom as a means to stabilize the simulation. Finally, chapter 9 gives a summary of the friction formalism and the results of the verification.

Chapter 2

Existing models for solid friction

Friction opposes the motion of a body: For dynamic friction in eq. (1.1) this means, that the friction is directed against the velocity. For static friction in eq. (1.2), there is no explicit velocity dependence. The friction force opposes the external force (i.e. the acceleration) as a constraint without energy dissipation: Because the time integral over the displacement vanishes, there is no related work. Static friction can be considerably smaller than the extrema set by dynamic friction. As long as there are no external tangential forces, it may be exactly zero. Dry friction cannot be treated as a "small perturbation": For dynamic friction, the friction coefficients are between 0.1 to 0.8, i.e. of the order of 1, while static friction is a constraint of motion and changes the overall dynamics of a system.

Modelling of static friction has been an ongoing topic over several decades, however the jump in the force at zero velocity has lead to problems until now. Many of the available models are empirical, based on observations and experiments, and therefore only valid for the scope of their own testing conditions. Other models have been developed with simulation in mind, or derived from pure mathematical treatment of discontinuous equations. Some models are capable of computing static friction for a single particle with a single contact. If more particles and contacts are treated as a problem of statics with given normal forces, the resulting equations usually become statically indeterminate, there are more unknowns than equations. The remainder of this chapter gives an overview of some models as well as their draw-backs

2.1 Viscous and "regularised" models

The main issue of static friction is that eq. (1.2) is multivalued, so that only the solution range is given. There is a considerable temptation to replace the value at or near $v = 0$ by a functional value: Typical regularizations have been made via viscous friction [32, 33] as in Fig. 2.1 b) as long as the velocity is small. Regularizations using $\arctan(v)$, as in e.g. Popov[7], belong to the same class of models. Also, instead of a continuous function,

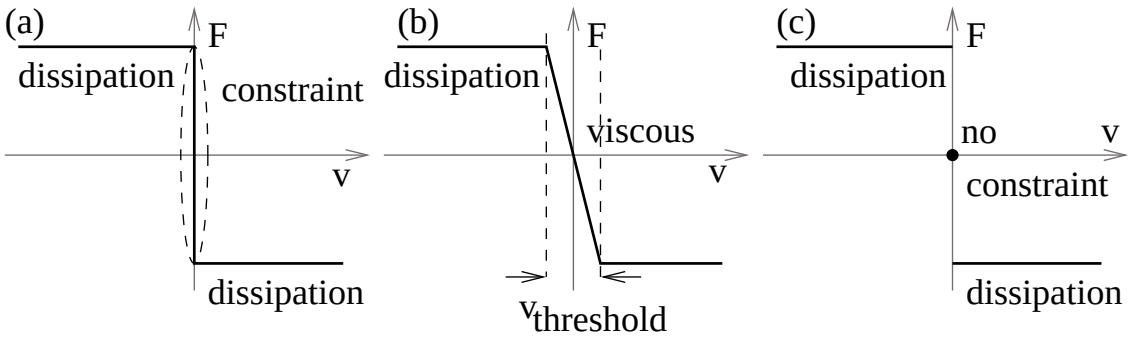

Fig. 2.1 Functional dependence of solid friction with dissipative, velocity independent dynamic regime and the range of possible values for static friction (emphasized by dashed line), which is not dissipative at all (a) as well as "regularizations" with viscous friction (b) and zero static friction (c).

eq. (1.1) has been interpreted in the sense of

$$\text{sign}(0) = 0 \rightarrow F_{\text{sli}}^{\text{fri}} = 0 \tag{2.1}$$

as in Fig. 2.1 c). Such regularizations are futile on physical grounds: They cannot even fix a block on a slope, as there will always be finite slip with an on average constant velocity.

2.2 Cundall-Strack model

The most urgent need for at least a plausible treatment of tangential forces arose in the field of discrete element modelling (DEM) for granular materials, because without static friction, DEM-particles flow like a gel. Such an assembly can withstand normal forces, but cannot retain realistic free slopes. Cundall and Strack[34] incremented (respectively cut off) in each time-step τ the tangential force according to

$$f^{\text{tan}}(t) = \begin{cases} f^{\text{tan}}(t-\tau) - k_{\text{tan}}\tau v^{\text{tan}}, & |f^{\text{tan}}(t)| \leq \mu F^{\text{N}} \\ \text{sign}\left(f^{\text{tan}}(t-\tau)\right)\mu F^{\text{N}}, & |f^{\text{tan}}(t)| > \mu F^{\text{N}} \end{cases} \tag{2.2}$$

where v^{tan} is the tangential velocity, and k_{t} the "tangential stiffness" of a "spring". Typical prefactors are multiples of the Young's modulus Y, like $k_{\text{t}} = 2/7\,Y$ derived for collisions of spherical particles [35]. For many problems, the algorithm is quite robust against a variation of k_{t} around 1, i.e. with a strength comparable to the normal forces so that plausible angles of repose can be obtained for polygonal particles[36]. Due to the cut-off μF_N in the second case of eq. (2.2), this approach is sometimes called "breaking tangential spring". While static friction is mimicked inasmuch as there can be a finite tangential force for zero tangential velocity, there are disadvantages: First of all, parameters may affect the simulation outcome, as for a too small $k_{\text{t}}(< 0.01)$, the "grip" is delayed compared to physical systems, while for a too large $k_{\text{t}}(> 2)$, the timestep must be reduced and the

approach becomes computationally more expensive. Another flaw is that the force law in the upper case of eq. (2.2) is effectively an undamped linear oscillator: A block on a slope below the critical friction angle will slide into the equilibrium position and then oscillate around it indefinitely. Damping with the tangential velocity

$$f^{\mathrm{tan,total}} = f^{\mathrm{tan}} - \gamma_{\mathrm{t}} \sqrt{k_{\mathrm{t}} m} v^{\mathrm{tan}}, \tag{2.3}$$

can be introduced with a dimensionless constant γ_{t} and the reduced mass m of the contacting particles. A further cut-off has to maintain $f_{\parallel,\mathrm{total}} \leq \mu F_N$. The disadvantage of eq. (2.3) is not only the additional parameter γ_{t}: Damping terms $\propto v_{\mathrm{t}}$ are for oscillators where the position is the degree of freedom, not for the "spring force" in eq. (2.2) for an oscillator with the velocity as variable. Damping and "spring force" are therefore out of phase and only relatively small prefactors γ_{t} can be used. Damping occurs over several (unphysical) oscillations and no "critical damping" can be introduced. A consolation is that the approach with eq. (2.2,2.3) is rather robust, so for any variation around $\gamma_{\mathrm{t}} \approx 0.05$ and $k_{\mathrm{t}} \approx 0.5Y$, the simulation results will hardly change. Conceptually, the Cundall-Strack model replaces a constraint force (which cannot perform work) with a degree of freedom (which can store or release energy). In a vibrated system, the "grip" will fail if the forces get too large.

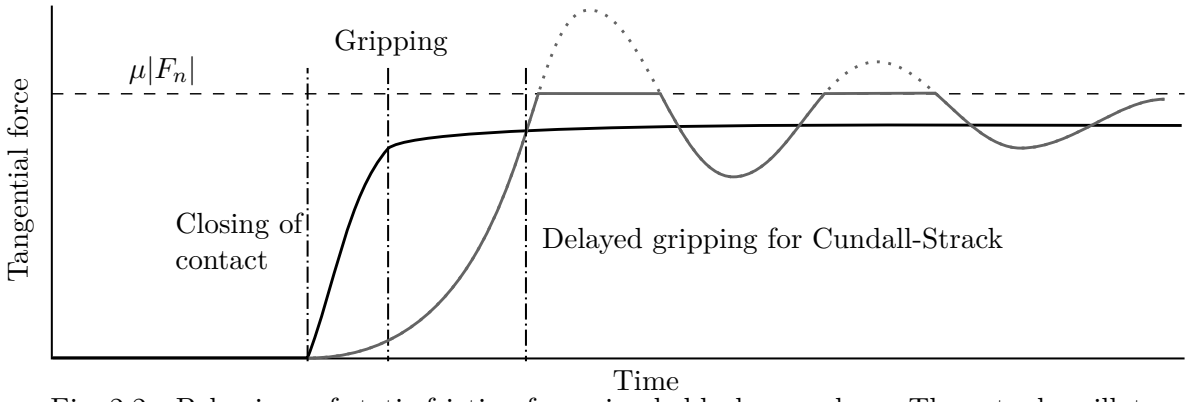

Fig. 2.2 Behaviour of static friction for a simple block on a slope. The actual oscillatory behaviour of the Cundall-Strack model is shown in a dashed line, while its cut-off behaviour is shown with a thin black line. The behaviour of the exact friction is shown as thick black line. The delayed grip of the Cundall-Strack model can be seen immediately after the onset of friction.

2.3 Contact dynamics

Contact dynamics was developed by Moreau[37, 38] as generalization of Newtonian kinematics from the field of "convex analysis" in a framework of differential inclusions. The solution for the tangential forces ("Coulomb graph", i.e. friction) as for the normal forces ("Signorini graph", impacts, stationary normal forces) have to be computed for a convex hull formulation according to eq. 2.14. Newtonian kinematics, which is based on derivatives

$$a = \dot{v} = \ddot{x} \tag{2.4}$$

had to be generalized for a non-smooth variation of $a(t)$, $v(t)$ and $x(t)$. While the approach is mathematically well founded, there are also downsides: The sound velocity is infinite, so that issues of shock propagation (with finite velocities) cannot be treated. As the limit of infinitely rigid particles is simultaneously the limit of infinitesimal small strains of particles with finite Young's modulus, the physical relevance is unclear. The evaluation of "elastic" properties of material assemblies seems to be limited as well, as jumps in the stress-strain diagrams of the bulk have been reported [39]. Other researchers have worked with similar rigid body approaches with a simultaneous solution of normal and tangential forces[40]. For discrete element problems, the contact dynamics approach has been extensively used by F. Radjai and co-workers[41, 42, 43, 44].

Unfortunately, this approach is not suitable if at first the normal forces should be determined based on material laws and afterwards the magnitude of Coulomb friction based on the kinematic situation. In this thesis a solution of the many-particle many-contact problem should be found in the framework of Newtonian kinematics, which yields a well-defined and unique solution. Moreau's contact dynamics does not fulfil such a requirement in two important aspects. First of all, an extension of Newtonian dynamics needs to incorporate accelerations due to jumps in the velocity. While this is mathematically possible, these generalized solutions may affect the physicality of the result. Another problem is Moreau's "sweeping process"[45], which is a kind of optimization approach based on mechanical principles. Apart from the fact that its explanations in the literature have been rather opaque (to say the least)[46, 37], it has never been demonstrated that the approach is actually unique. That both normal forces and tangential forces for rigid particles are treated simultaneously means that perturbations in the system propagate independently in orthogonal direction at infinite velocity. The physical situation is certainly that the tangential force is a reaction to the normal force, as has been explained in chapter 1.

2.4 Formulation as linear complimentary problem

In linear complementary problems, a solution is obtained for a global optimization problem with additional conditions. Friction related constraint problems and solvers have been studied in this framework [47, 48, 49, 50] for considerable time. A multi-body solution for N contacts has been sketched formally[48] by Stewart as

$$\boldsymbol{M} \cdot (\boldsymbol{v}^{l+1} - \boldsymbol{v}) = \sum_{j=1}^{\mathrm{N}} (\boldsymbol{n}^{(j)} c_n^{(j)} + \boldsymbol{D}^{(j)} \beta^{(j)}) + h\boldsymbol{k}, \tag{2.5}$$

where $\boldsymbol{M}$ is a positive definite, symmetric inertia matrix, $\boldsymbol{v}$ the generalized velocities, $\boldsymbol{n}^{(j)}$ the normal vector for the j-th contact, $c_n^{(j)}$ the average normal contact force for the j-th contact, the matrix $\boldsymbol{D}^{(j)}$ is formed by the vectors spanning the friction space at the $j-th$ contact in generalized coordinates, $\beta^{(j)}$ are the coefficients for the frictional impulse, h is the step-size of the iteration and $\boldsymbol{k}$ is the vector of the generalized external forces. Unfortunately, it is not clear from Stewarts' works whether the matrix $\boldsymbol{D}^{(j)}$ and the concept of friction space are physically meaningful or even well-defined in systems in higher dimensions and with rotational degrees of freedom. The friction space can not be a linear vector space, as that would imply independent equations. It either is a space of conditional, i.e. not independent inequalities without physical criteria to solve them, or leads to static indeterminate solutions of overdetermined static contacts and, again, no solution criteria, see Fig. 2.3. The increment of the generalized coordinates $\boldsymbol{q}$ is given by

$$\boldsymbol{q}^{l+1} - \boldsymbol{q}^{l} = h\boldsymbol{v}^{l+1}. \tag{2.6}$$

For these equations Stewarts' solution requires a set of constraints:

$$\begin{aligned}
\boldsymbol{n}^{(j)\top} \boldsymbol{q}^{l+1} &\geq \alpha_0^{(j)}, \quad c_n^{(j)} \geq 0, && (2.7)\\
\lambda^{(j)} \boldsymbol{e}^{(j)} + \boldsymbol{D}^{(j)\top} \boldsymbol{v}^{l+1} &\geq 0, \qquad \beta^{(j)} \geq 0, && (2.8)\\
\mu^{(j)} c_n^{(j)} - \boldsymbol{e}^{(j)\top} \beta^{(j)} &\geq 0, \qquad \lambda^{(j)} \geq 0, && (2.9)
\end{aligned}$$

where $\alpha_0^{(j)}$ is the scalar for locating the boundary of the j-th half-plane, $\lambda^{(j)}$ a parameter with no meaningful physical interpretation, $\mu^{(j)}$ the coefficient of friction for the j-th contact, and $\boldsymbol{e}^{(j)}$ a column vector of ones. In addition he has three complementary conditions,

$$\begin{aligned}
\left[\boldsymbol{n}^{(j)\top} \boldsymbol{q}^{l+1} - \alpha_0^{(j)}\right] c_n^{(j)} &= 0, && (2.10)\\
\left[\lambda^{(j)} \boldsymbol{e}^{(j)} + \boldsymbol{D}^{(j)\top} \boldsymbol{v}^{l+1}\right] \beta^{(j)} &= 0, && (2.11)\\
\left[\mu^{(j)} c_n^{(j)} - \boldsymbol{e}^{(j)\top} \beta^{(j)}\right] \lambda^{(j)} &= 0. && (2.12)
\end{aligned}$$

While the existence of solutions for such a multiple-contact linear complementary problem was shown, there is an inherent ambiguity for the case of several, non-collinear contacts in

static friction. The explicit resolution of the ambiguity has not been addressed. Explicit equations were only formulated for one-dimensional strings of particles, which leads to the same solution as the approach from sec. 2.7 by Hairer and Wanner[51] for chains of blocks[16].

Due to the necessary global optimization with constraints, a physical, smooth variation of forces cannot be guaranteed and jumps of the forces will lead also to numerical problems with finite-difference time integrators. Stewart's relatively recent textbook on the dynamics with inequalities[52] does not mention many-body systems at all (the geometrically most involved problem is a rigid sphere with two oblique contacts). For these reasons, the approach does not appear to be generalizable for arbitrary many-body configurations.

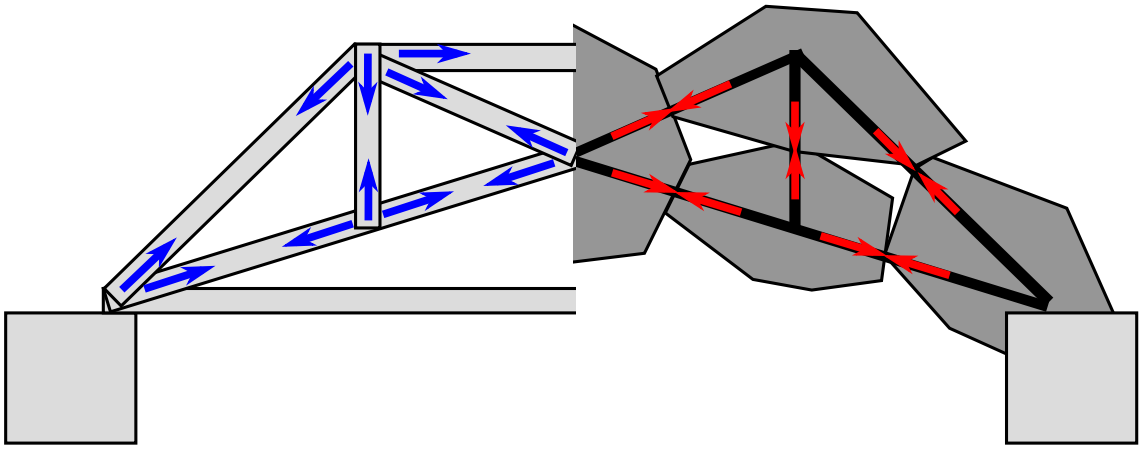

Fig. 2.3 Static friction for particles with many contacts leads to static indeterminate problems for the centres of mass. A problem of overdetermined trusses under pulling strain is equivalent to a granular assembly under compressive strain.

2.5 Leine and Nijmeijer

Leine and Nijmeijer[53] have described various approaches for dealing with non-smooth mechanical systems (in particular friction, in parts also for rigid normal contacts) in a mathematical framework with particular attention to aspects of non-linear dynamical systems. Nevertheless, a generalization of their approaches to higher dimensions and multi-particle contacts seems difficult, the authors have not made such attempts themselves or sketched any strategies. Their formalism makes use of an absolute space, with a clearly defined zero velocity, which will not be available for simulations of many bodies with numerical noise. Therefore, this approach as well seems to be limited to single body problems.

2.6 Differential inclusions

For an ODE with non-smooth right hand side $f(x,t)$ in

$$\dot{x} = \frac{f(x,t)}{m} \tag{2.13}$$

the $\epsilon - \delta$ continuity criterion cannot be applied for existence and convergence proofs. Filippov[2] constructed solutions within the framework of "differential inclusions" at (x_0, t_0) with a jump for $f(x_0, t_0)$ from solutions "from the left" $f(x_0 - \epsilon, t_0) = f_I$ and "from the right" $f(x_0 + \epsilon, t_0) = f_{II}$ in their "convex hull"

$$f(x_0, t_0) = (1 - \lambda) f_I + \lambda f_{II}, \quad 0 \leq \lambda \leq 1, \tag{2.14}$$

see Fig. 2.4. Problems with static friction eq. (1.2) belong to this class of problems, where at $x \doteq 0$ the value for the friction force lies in a range of $[-\mu F^{\mathrm{N}}, +\mu F^{\mathrm{N}}]$.

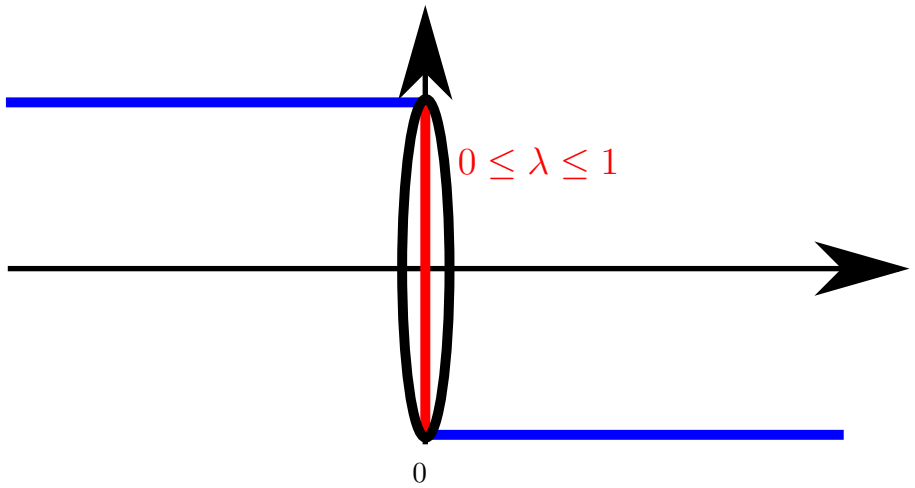

Fig. 2.4 The Filippov-solution for ODEs with non-smooth righthand sides is constructed in the convex hull of solutions "from the left" and "solutions from the right". It leads to an accumulation of stable fix points that is suitable to describe mechanical equilibria for static friction.

The conventional theory for one-dimensional second order autonomous ODEs allows only three types of attractors from the roots of the characteristic polynomial foci (see e.g. Kaplan and Glass[54]): circular attractors, nodes and saddle points in their stable and unstable, as well as their degenerate forms. ODEs with non-smooth right hand sides (which can be considered as superposition of certain non-autonomous systems) have more possible attractors, in particular some which are relevant for the phase flow systems with dry friction: Accumulation points of stable nodes (fix points) describe the stability of the final state of frictional oscillators.

Filippov had obtained his differential inclusions "by construction" and in an earlier work[55] explicitly made reference to an oscillator with viscous and dry friction. While

the approach itself is mathematically impeccable, the actual application to numerical simulations in the presence of rounding- and discretisation errors is less clear, as velocities are rarely ever "exactly zero".

Newer, more abstract approaches to differential inclusions [56, 57, 58] are more focused on the set theory of possible solutions and not suitable for numerical (finite difference) solutions with trajectories, in contrast to Filippov's approach.

2.7 Hairer and Wanner

The approach which comes closest to the idea presented in this thesis is that of Hairer and Wanner[51]: For a single oscillator they determine the roots (zero crossings) in the velocity, give a criterion for static friction and evaluate the static friction in the convex hull of the possible dynamic friction values. They describe their approach explicitly as a numerical "Filippov-solution". The generalization for a one-dimensional chain of particles is straightforward[16], but until now, there was no formalism that would give a smooth and unique solution for higher-dimensional geometries. Nevertheless, a drawback of their approach is the usual, "fixed" coordinate system of ODE-theory and the implementation for solvers with adaptive timesteps. The formulation for arbitrary relative coordinates, the generalization to the case of two dimensions and arbitrary many contacts, as well as the adaptations to use with constant timesteps and the discussion of the numerical stabilization will be discussed in chapters 5 and 6.

2.8 Stribeck friction

From our standpoint, Stribeck friction is actually a modification of Coulomb friction for finite velocities, the jump at $v = 0$ and the possibility of a finite friction value for vanishing velocity is not affected. Because Stribeck friction is relevant for many technical problems, we mention it here to show that our approach can also supply a solution for this case. The friction force is a superposition of solid friction μF^{N}, viscous friction $\sigma_v v$ and a decay from a high friction "overshoot" value near $v = 0$, $F^s(v)$, which is often attributed to the "higher coefficient of static friction", but may as well be due to cohesion effects caused by lubricants at the contact (Fig. 2.5),

$$F^{\mathrm{fric}}(v) = \mu F^{\mathrm{N}} \mathrm{sign}(v) + \sigma_v v + F^s(v). \tag{2.15}$$

The effect of the normal pressure is more complicated than for dry friction, because it also affects the thickness of the lubrication film. The effect of the film thickness is described in the Stribeck curve, see Fig. 2.6.

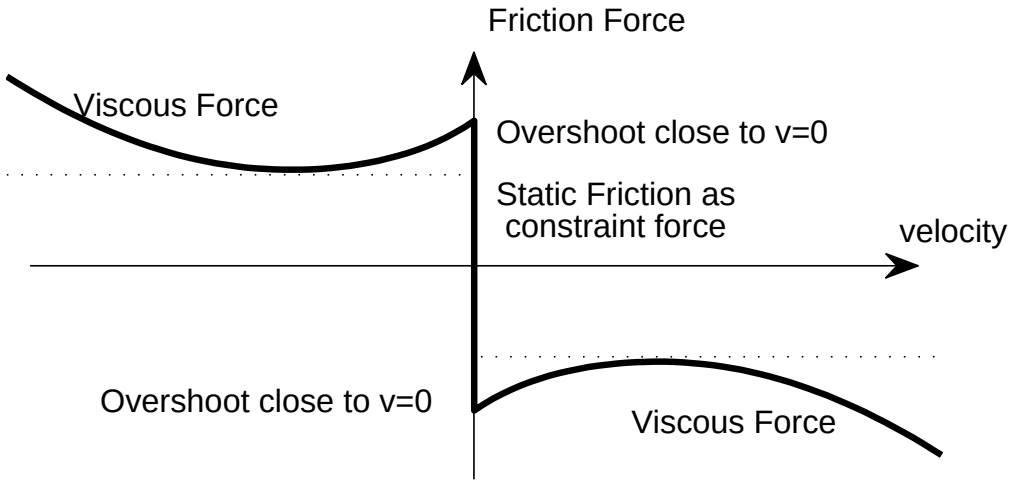

Fig. 2.5 Dependence of the Stribeck friction on the velocity for a given load. The lubricated surfaces will have a different plateau than the dry friction of the same materials.

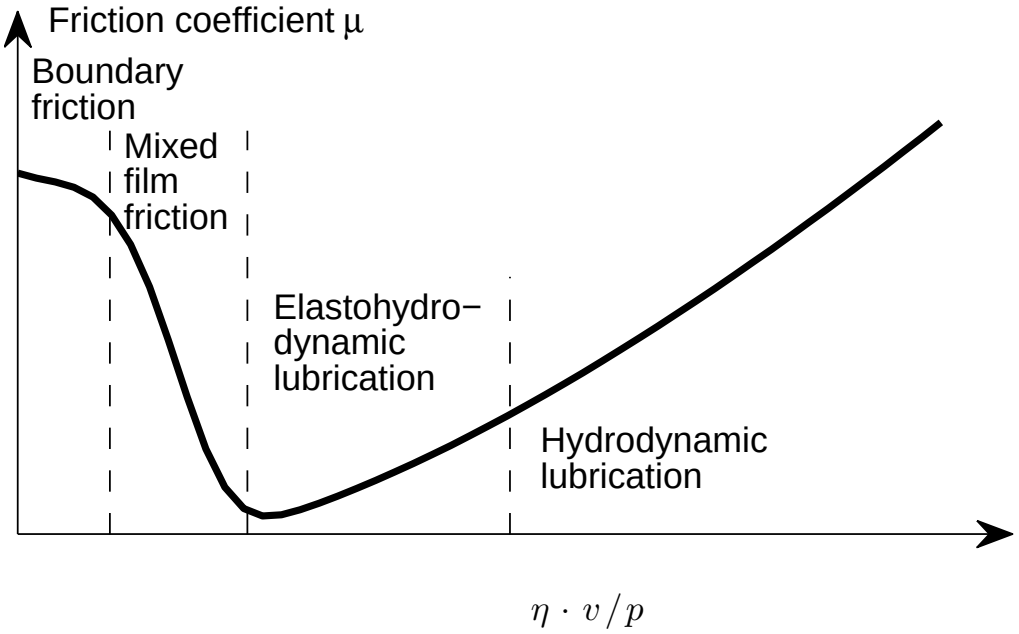

Fig. 2.6 Stribeck curve with the different lubrication regime plotted over the Stribeck number (dynamic viscosity η · sliding speed v / pressure p), to which the film thickness is more or less proportional.

2.9 Heuristic models

The static friction models discussed in this chapter so far were all analytic models, that is they tried to justify themselves through micromechanical modelling. On the other end of friction models are heuristically motivated approaches. Instead of being physically motivated they are designed to match experimental results as accurate as possible without any justification for their parameters.

The Dahl model[59, 60] is an empirical generalisation of Coulomb friction. It was originally developed by Dahl based on experiments with ball bearings where he found, that for small displacements objects would return to their original position. He likened his model to spring-like elastic behaviour between bristles on the two surfaces, see Fig. 2.7. For small displacements the deformation was elastic and the displacement hysteretic, while for larger displacements, the deformation of the interface would become plastic, resulting in permanent displacement,

$$\frac{\mathrm{d}F}{\mathrm{d}x} = \sigma \left| 1 - \frac{F^{\mathrm{fric}}}{F_C}\mathrm{sign}(v) \right|^i \mathrm{sign}\left(1 - \frac{F^{\mathrm{fric}}}{F_C}\mathrm{sign}(v) \right), \tag{2.16}$$

where F^{fric} is the friction force, F_C the Coulomb friction, x the displacement, σ the stiffness coefficient and i a material dependent parameter determining the shape of the stress-strain curve. Dahls model is also called an internal state model as the friction force F^{fric} describes the internal state at the point of contact.

In its original form the Dahl model suffers from oscillatory behaviour, which means it is insufficient for treatment of static friction. The so called LuGre[1][61] transforms Dahls equation into a state equation. The friction force is regularized with an internal elastic state variable z,

$$F^{\mathrm{fric}} = \sigma_0 z + \sigma_1 \frac{\mathrm{d}z}{\mathrm{d}t} + \sigma_2 \frac{\mathrm{d}x}{\mathrm{d}t}. \tag{2.17}$$

σ_0 is a stiffness constant, σ_1 is a damping parameter for small relative movements, and σ_2 is a damping parameter for large relative movements in the sense of a viscous damping. The time evolution of z is given by the state equation

$$\frac{\mathrm{d}z}{\mathrm{d}t} = \frac{\mathrm{d}x}{\mathrm{d}t} - \frac{z}{g(\mathrm{d}x/\mathrm{d}t)} \left| \frac{\mathrm{d}x}{\mathrm{d}t} \right|, \tag{2.18}$$

where $g(\mathrm{d}x/\mathrm{d}t)$ is a kind of Stribeck curve. Further extensions of the original Dahl equation eq. (2.16) exist. None of these heuristic models yield static friction, i.e. a finite value of friction which prevents the relative motion of two contacting surfaces relative to each other. That means that they are unsuitable to describe a force equilibrium at zero velocity. contain true static friction. That is, for static contacts, the models will not describe force equilibrium and zero velocity.

[1]Named after the cities in which it was developed, *Lu*nd and *Gre*noble.

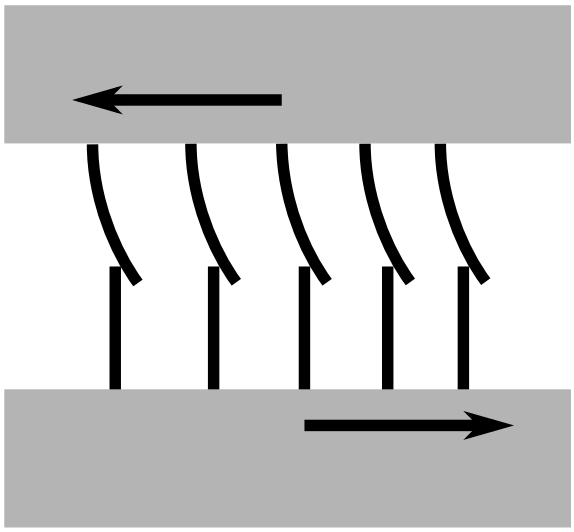

Fig. 2.7 Influenced by the roughness notion of friction, the Dahl-model tries to replace constraint forces via spring-like bristles on the contact interface. The bristles mimic hysteretic displacement or plastic deformation with oscillatory behaviour, but completely ignore the atomic nature of the surface interactions.

Chapter 3

Granular media as a frictional many-body systems

The friction problem in granular media differs from technical multi-body systems in several aspects. Granular particles can be placed and arranged freely, i.e. the relative positions are not subject to constraints as they are for machine elements. As a consequence, many stabilisation approaches and considerations from mechanical engineering do not apply to granular materials. Surface roughness is controlled in technical applications by grinding or polishing the surfaces. Surface roughness in granular media is arbitrary and unknown: Particles in the same aggregate can both be rough and smooth. Material parameters, such as the friction coefficient are easy to control in machinery by choice of standardised materials, while for granular materials, even for single grains, the surfaces are often chemically inhomogeneous.

3.1 Classification of granular materials

Granular materials are assemblies of solid, macroscopic particles. They interact mainly with collisions which exert force in normal direction and solid friction which exerts force in tangential direction. They are among the most common substances found in nature and technical applications. As sand or gravel they make up the soil we stand on,as powders and grains they are the constituents of many foodsand medicines,and even for massive-scale objects like asteroids and planetoids in asteroid beltsor planetary ringssome researchers try to develop theories in a “granular framework”. Some of the more common examples of granular particles at different sizes are shown in figure 3.1. However varied granular media might be, they all share the same fundamental nature: While there is disorder at the level of individual grains, at macroscopic level they can form ordered structures, be rigid like solids or flow like liquids.

Fig. 3.1 Some examples of granular media. Clockwise from top-left to bottom-left: Flour has approximately same sized grains of $d_{\text{particle}} \sim \mathcal{O}(10\mu\text{m})$, aggregates show no disorder; similarly rice grains have similar sizes $d_{\text{particle}} \sim \mathcal{O}(\text{mm})$), but their aggregates show large disorder in orientation; rocks have some variation in size ($d_{\text{particle}} \sim \mathcal{O}(\text{dm})$), but also a very notable variation in shape; size dispersion can reach large levels in nature($d_{\text{particle}} \gg \mathcal{O}(\text{m})$).

Broadly speaking, granular materials are characterised by macroscopic parameters like density, angle of repose flow velocity, etc. Granular aggregates can be characterised by states like granular solids (soil, heaps) or granular liquids (debris flow), or even granular gases (pneumatic transport). While the elastic force is "scale invariant" between grains, depending on their size there are effects from different forces: Particles below 100μm are subject to humidity, air-drag, or electro-static interactions, their agglomerates are commonly referred to as powders[1]. For particles with diameters between 100μm and about 1cm, cohesion due to agglomeration of water molecules on their surfaces comes play a role in humid environments[2]. Particles above that size are not affected much by temperature changes at macroscopic level, their main interactions are elastic forces in normal direction and Coulomb friction in tangential direction.

Granular media consist of large numbers of particles. A single teaspoon full of sugar, for example, can contain around a million particles. This makes quantitative treatment of all particles individually very difficult. While continuum methods are widely used in material sciences and fluid dynamics to deal with the large number of constituent atoms in solids or liquids, the variation in size and scale is much larger in granular media. Phenomena,

[1]The exact limit varies from reference to reference, but the order of magnitude is roughly the same.

[2]For experiments with acrylic beads in a rotating acrylic drum, we found different behaviour at different air humidities: At usual air humidity, the aggregate showed avalanching, but the whole aggregate slid like a single block down the drum wall when air humidity fell below 10% in winter. That means, that even for cm-sizes particles, the friction coefficient can be affected by the humidity of the surrounding air.

which are of interest in granular media may occur on length scales well below where the continuum assumption becomes valid, such as the surfaces of particles.

Fig. 3.2 Sharp-edged rocks due to fracturing (left), stones in a river bed washed smooth by water (right).

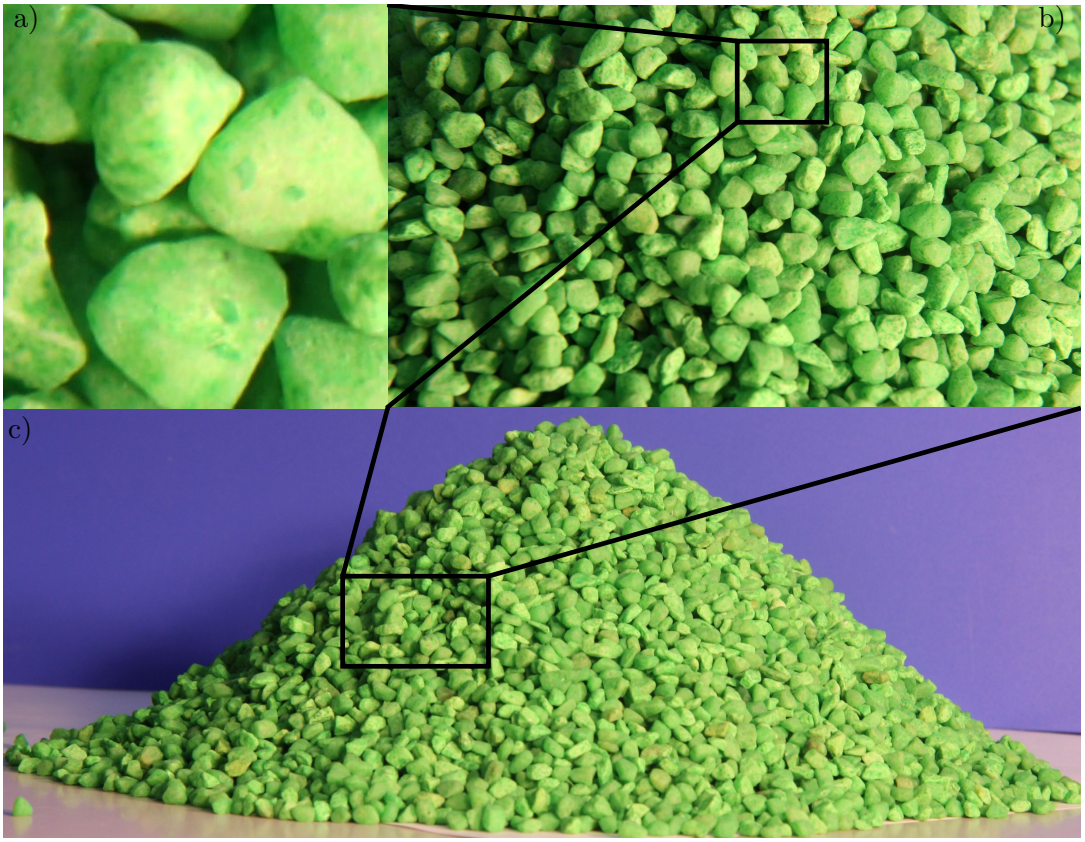

Fig. 3.3 Relevant size scales in granular media: a) contacts and particles ($d_{\text{contact}} \lesssim d_{\text{particle}}$), b) representative volume (micro-structure) ($d_{\text{micro}} \gtrsim d_{\text{particle}}$)., c) macro-structure, ($d_{\text{macro}} \gg d_{\text{particle}}$).

Beyond size dispersion, granular media also show shape dispersion. Sand and stones on a river bed can be washed smooth, but individual particles will have their own shape, elongated and deformed. Rocks and gravel, found for example in rockslides, are sharp-edged from breakage and fracture and will have a more blocky shape with flat sides, see Fig. 3.2. The shape of granular particles has significant influence on their behaviour under friction. While particles with flat sides will slide or rest, depending on the friction forces, a round particle can escape sliding friction by rolling. In general, one can say that the more a particle deviates from round shape, the stronger will the "grip" of friction on that particle be.

Excluding considerations on the atomic scale, the fastest interactions of granular particles are collisions between grains: momentum transfer and the "grip" of dry friction occur almost instantaneously. The longest timescales in laboratory environments usually are of the order of weeks, while in rock mechanics and geology, the timescales may be years and decades for reordering, or centuries to thousands of years for weathering and fracture of rocks to millions of years for formation planetary features. In numerical simulations, the required computation time, i.e. the choice of the timestep, depends on both the largest and the smallest timescale of the system in consideration[16], as the individual interactions have to be resolved, while at the same time the simulation needs to finish in reasonable time to see its results.

3.2 Dynamics and interactions between granular particles

In dry granular media, in the absence of a surrounding liquid medium, particles interact only through visco-elastic forces in normal direction and through non-linear Coulomb friction (eqs. (1.1, 1.2)), in tangential direction. The inherent dissipative nature of these interactions leads to a rapid decay of the (kinetic) energy in granular agglomerates. In granular solids, this effect is, for example, exploited in sandbags or gabions (stone filled baskets) to protect military bases against gun fire. In granular gases, minuscule initial inhomogeneities in density can grow into clusters of multiple particles (see e.g. [62] and figure 3.4), or multiple particles may merge into fewer but larger particles in a process called sintering. On the other hand, particles that are subject to high stress may fracture and break into multiple smaller particles (as sketched in Fig. 3.5a)).

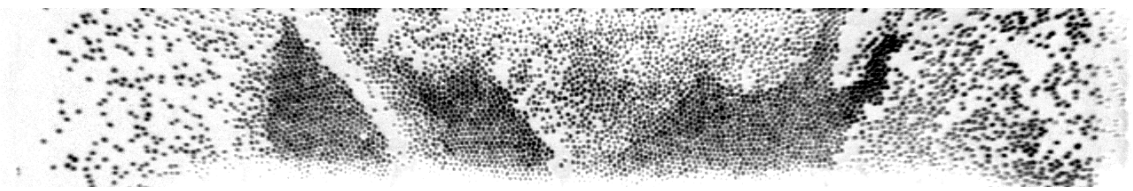

Fig. 3.4 Clustering of mustard seeds into stripes in a horizontally vibrated submonolayer[62].

The dynamics of granular particles is governed by a competition between rolling and sliding. Round particles prefer to roll (Fig. 3.5b), as the energetic costs of rolling are much lower than those of sliding. Elongated particles will prefer to slide Fig. 3.5c), as the energetic costs to lift their centres of mass over their sides are significantly higher than the costs of sliding. In general, the dynamics of granular assemblies result from a combination of rolling and sliding, depending on the particle shapes. The shape dependent dynamics influence the frictional behaviour of particles. As elongated particles are more prone to sliding, they experience more solid friction, whereas the "grip" of solid friction is reduced in the case of round particles. Non-convex particles can show entirely different behaviour. Concavities on their surfaces can interlock (Fig. 3.5d)), which restricts their degrees of freedom and particles may temporarily (or permanently, depending on the configuration) move as one. For granular aggregates, that means, that the dynamics of individual particles affect the properties of the entire bulk. For example, aggregates of angular particles show weaker bulk material strength than aggregates of round particles with the same particle hardness[63].

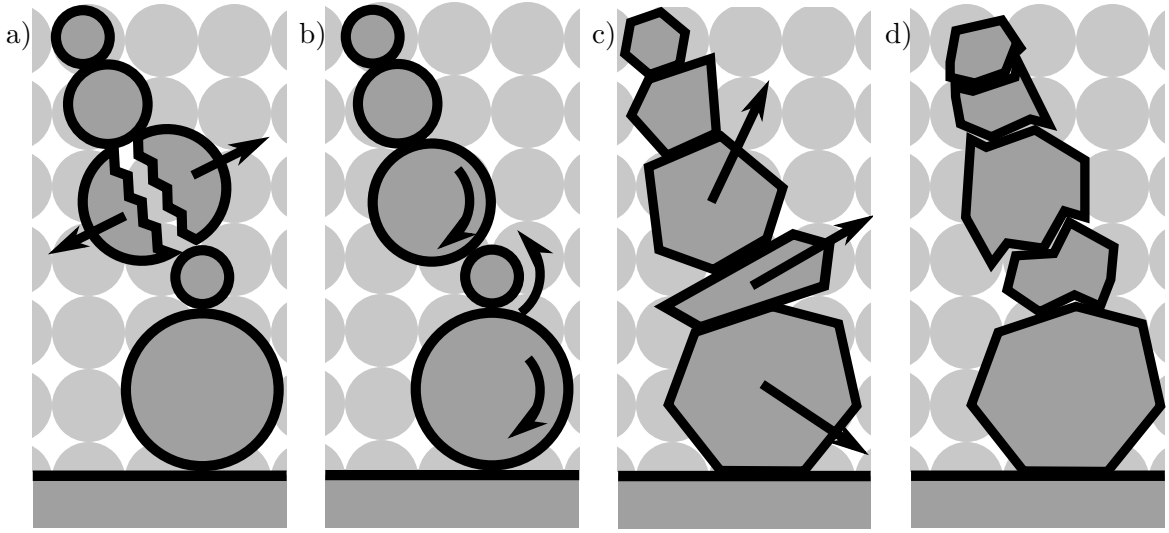

Fig. 3.5 Sketches for a) fracturing of bigger particles into smaller particles, b) rolling as the preferred method of motion of round particles, c) sliding of elongated particles, and d) interlocking due to irregular shape.

3.3 Granular solids

When granular particles are stationary with respect to each other and their environment, such as in a heap of sand, their agglomerates can be considered as solids. Within those granular "solids", forces are not transmitted continuously, but along discrete paths, also called "force chains". This allows some unusual behaviour for particle aggregates, such as formation of stable arches or saturation of vertical pressure inside containers.

3.3.1 Elasticity and plasticity

A medium is considered to be elastic when its deformation is reversible. Classical solids have a preferred low-energetic crystal packing. After small deformations, the atoms will return into their equilibrium position. For dry granular materials, elasticity is almost negligible, limited to stresses of about $10^{-5}\mathrm{N/m}^2$[64]. Above this limit, rearrangements of the bulk are irreversible, friction and dissipation give granular materials almost perfect plastic behaviour. A bean bag used in juggling, for example, will simply sit on the floor when dropped, instead of jumping or rolling away, as normal dissipation and friction forces quickly dissipate any kinetic energy gained in the drop. On the other hand, individual granular particles are almost perfectly rigid on the micro-scale where the deformation from collisions is many orders of magnitude lower than the diameter of the particles, which justifies the "hard-particle" approach for modelling.

3.3.2 Granular heaps

Unlike fluids, granular particles are able to form heaps with straight slopes, whose angles, all other parameters being the same, depend entirely on the friction coefficient and the shape of the particles. Without cohesive forces, building a static heap will not be possible with round particles. As their mobility is notably higher than for elongated particles, they will simply roll away and the heap will dissolve. On the other hand, with polyhedral particles, it is even possible to build stable heaps on tilted, polished mirrors, see Fig. 3.6, as their form allows a much stronger "grip" of solid friction. Sand heaps sitting on inclined mirrors are a striking example that surface roughness does not play the dominant role in friction: It is difficult to imagine a surface smoother than that of a polished mirror. If slipping is possible between the ground and the particles, then slipping will also influence the formation of the heap, otherwise the heap is mainly formed by avalanches on the slope surfaces.

Fig. 3.6 Heap of polyhedral particles built on a tilted polished mirror. Neither the smoothness of the mirror nor its inclination prevent the heap from being stable.

Formation of heaps on smooth (but frictional) surfaces can be used for verification of DEM simulations: If the slopes are not straight or if auxiliary walls or surface roughness on the ground are needed, then there is a problem with the modelling. For round particles, that error is already their shape which prevents the "grip" of static friction and the particles will simply roll away. While this problem is often "circumvented" by using unrealistically high rolling friction coefficients or turning rotation off altogether, this kind of modelling is inconsistent with classical mechanics. If the fundamental behaviour of the constituents of the simulation is unphysically manipulated, then any outcome has to be taken with caution. In the same manner improper modelling of friction forces may cause issues with the formation of the heap, or its stability after formation. Friction models that do not account for static friction may not properly compensate the forces between particles and lead to residual velocity that slowly dissolves the heap. If static friction in a simulation of a heap is (unphysically) disabled, then the heap will very fast disintegrate and flow apart in a liquid-like manner (Fig. 3.7).

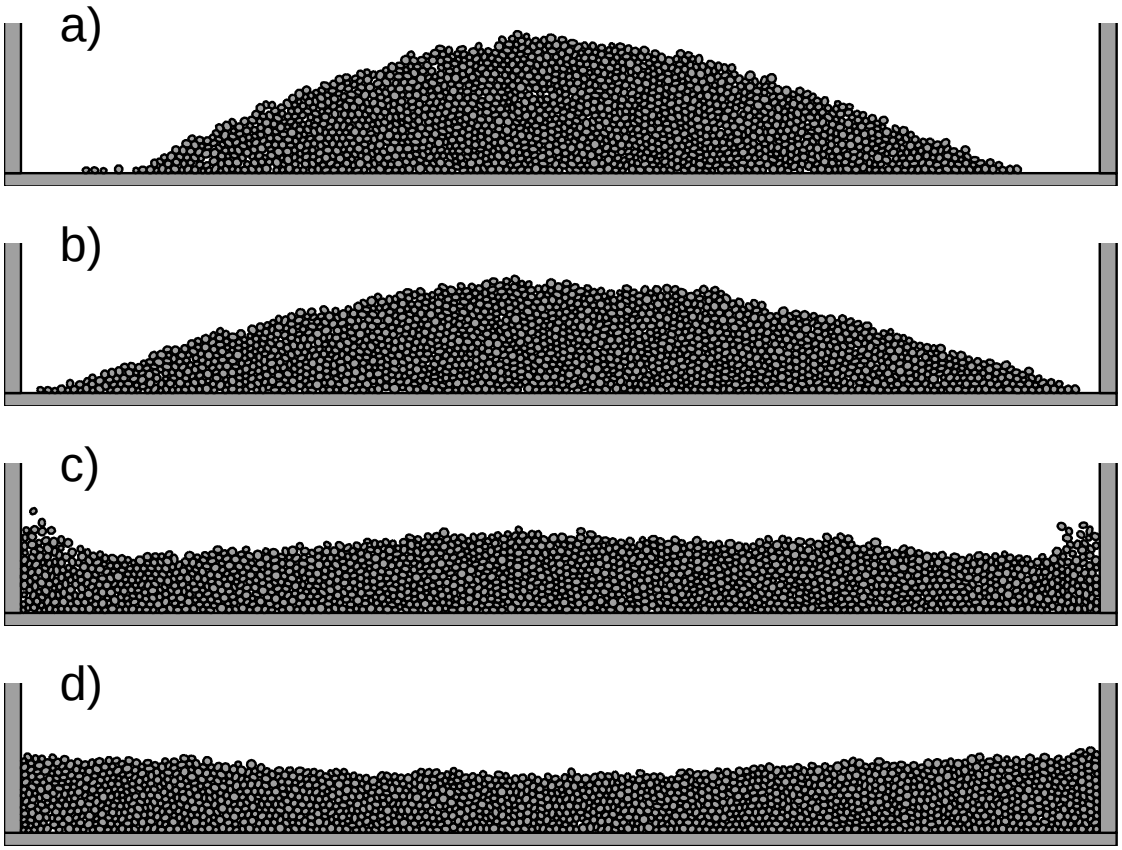

Fig. 3.7 Snapshots of the heap build under the influence of friction a). Then friction is turned off and the heap flows apart b)-d). While the behaviour looks viscous, in contrast to Newtonian fluids, such an assembly can withstand static normal stresses.

3.3.3 History effects in granular media

In the 19th century, Maxwell suspected a "historical element" in the pressure on embankments on walls, i.e. an influence of the construction history. This was later confirmed by Darwin, who found pressure differences up to 30%[65], depending on how he created his assemblies. Theoretical descriptions by contemporaries like Boussinesq[66], while confirming the historical element, were mired with flawed assumptions, such as infinitesimal dropping height of particles, so as to not disturb the existing aggregate. Maxwells results were forgotten for a considerable time. Researchers from different fields, such as civil and chemical engineering, prepare their assemblies in different ways and consequently obtain different results, even for such simple properties as the density distribution (Fig. 3.8). It was only very recent that the historical element had been rediscovered, first in simulation by Matuttis[67], and shortly after with an experimental verification by Vanel[68].

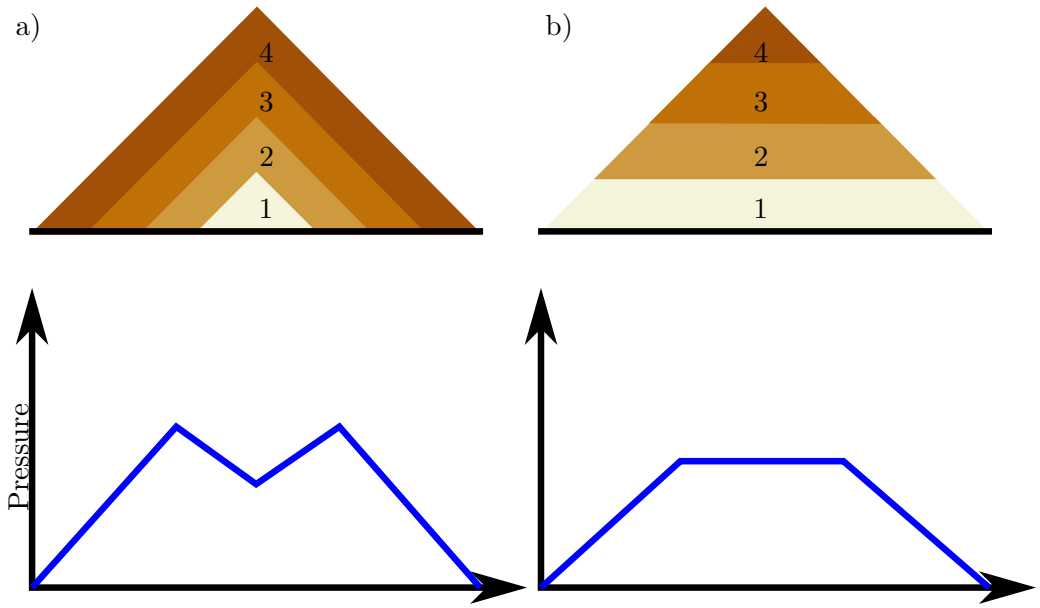

Fig. 3.8 Sketch of the pressure distribution inside granular heaps formed in different ways showing the importance of history effects in granular media. In a) the heap is formed by dropping material from the top, the pressure distribution shows a dip in the centre. In b) the material is piled up in layers. The resulting pressure profile is flat.

3.3.4 Reynolds dilatancy

In 1885, Reynolds introduced the concept of dilatancy[69], that is, volume expansion of densely packed granular materials under the influence of external stresses. When external stress forces the particles to disentangle from a dense initial configuration, the resulting state will be less dense (see Fig. 3.9). A well-known example is that of wet sand becoming dry when one is walking on the beach, e.g. Fig. 3.10. Under the weight of the person, the sand grains are pushed into a less dense configuration, and as a result, water drains from the surface into newly opened pore space below. This effect also highlights another

fundamental difference between grains and atoms. Whereas atoms favour one crystal packing over another, and are able to transit from an energetically high 'wrong' packing to a preferred lower energetic 'right' packing, a granular system is purely mechanical and almost perfectly plastic, friction and dissipative normal forces prevent free movement of the particles, and no relaxation into other states is possible without external forces. It is possible for the aggregate to be less stable in its dilatant state due to the decreased number of contacts between its particles.

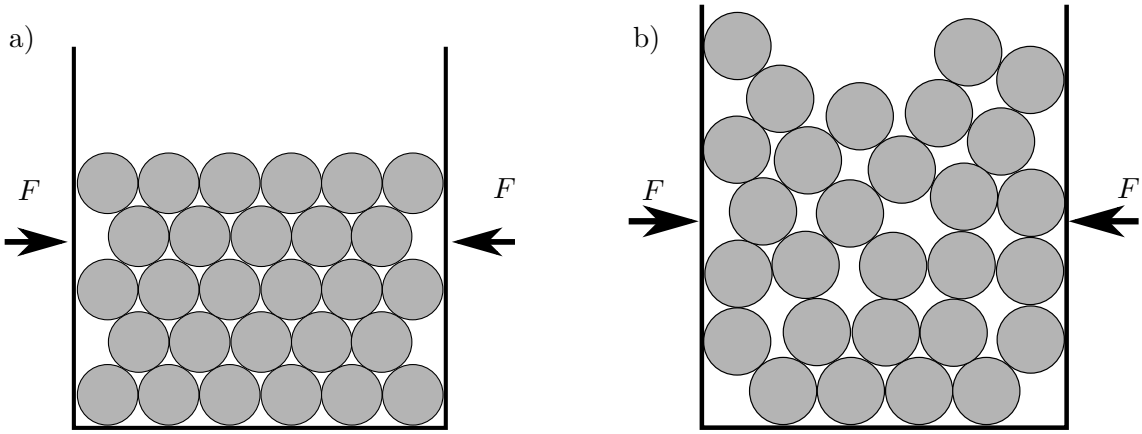

Fig. 3.9 Particles in a close packing a) occupy a less dense packing b) after the application of external stresses.

Fig. 3.10 Macroscopically, sand drying under the feet, visible as bright spot, on the beach is one of the most well known examples of dilatancy.

3.3.5 Forces distribution inside granular assemblies

If one fills a cylinder with granular particles, then the pressure inside this cylinder will not linearly increase with depth, like with a fluid, but rather saturate[70, 71]. In 1895 Janssen[72] derived his silo-equations under the assumption that the frictional interaction with silo walls supports the bulk of the material, even for particles not in contact with walls. The weight of the particles is deflected laterally through force networks until its force is finally absorbed by frictional and dissipative interaction with the walls. The forces in granular assemblies are distributed along discrete force networks (e.g. Fig. 3.11, left, for particles inside a box), allowing granular particles to deflect their downward force horizontally. This leads to the formation of stable arches (Fig. 3.11,right) that only become stronger with increasing pressure from above, as the strength of the particle interaction increases, for as long as the support on the sides is stable.

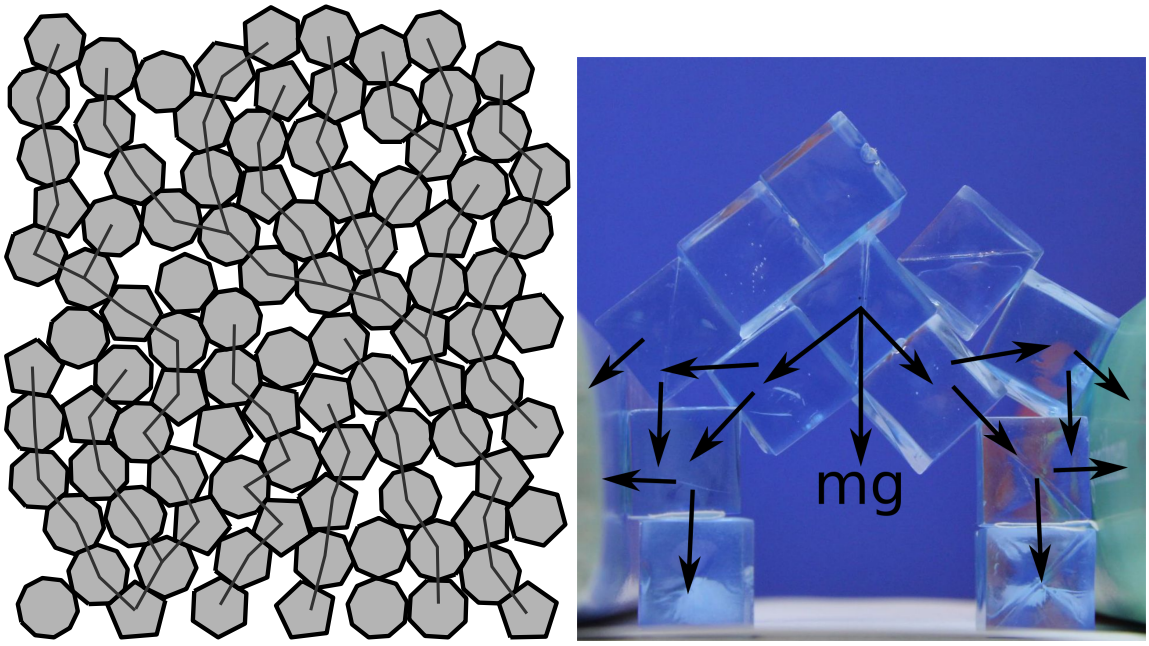

Fig. 3.11 Left: Force network within a static granular configuration. Lines represent the normal forces transmitted along discrete contacts. Right: Granular force networks can result in stable arches by redirecting the particle weight into static walls.

3.4 Granular flow and granular "liquids"

Unlike ordinary solids, granular media are able to flow, but unlike ordinary liquids, due to the silo-effect mentioned in the previous chapter, their flow rate is constant, independent of the filling height of their container, a direct consequence of the force networks in their bulk, see sec. 3.3.5. This advantage of sand-clocks over water-clocks has been exploited since at least the third century AD[73] to measure time with hourglasses, like in Fig 3.12. On geological scales, granular flows, such as landslides or debris flows, are some of the largest events to alter the surface of the planet, see e.g. [74] and the references therein. While granular flows resemble classical liquids on a macroscopic scale, the micro-mechanical behaviour shows notable differences. For a granular flow the energy dissipation due to friction does not decrease with the velocity, and if the angle of the slope drops below a critical angle, the frictional interaction between the particles and the particles with the ground will eventually cause the flow to stop.

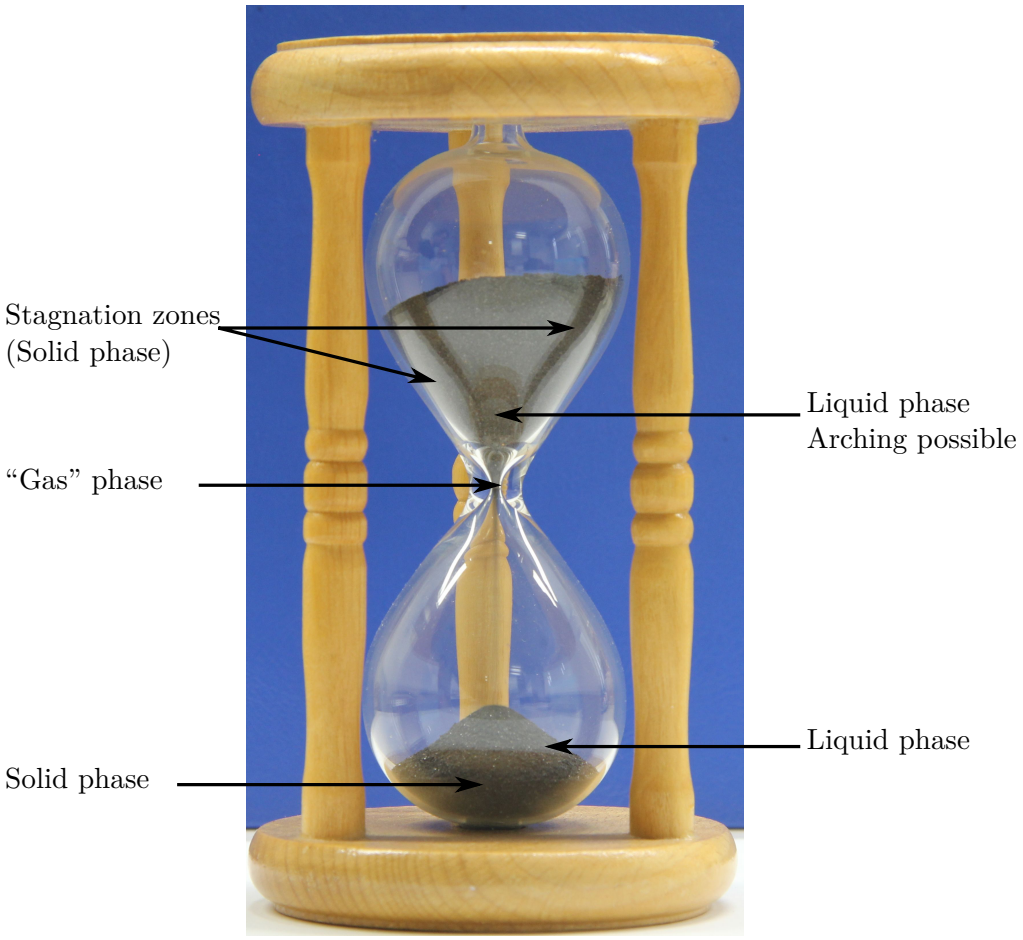

Fig. 3.12 Hourglasses show three states of matter for granular media: In the upper part, the particles form a solid, further down, near the orifice, they flow in a liquid-like manner. Past the orifice, the particles fall with little interactions with other particles with a large mean free path, resembling a "gas". In the bottom, on the top, the particles condense into a solid like heap, with regular granular avalanches down the slopes.

In addition, the lateral redistribution of forces with force chains and the formation of granular arches has significant influence on the rheology of granular flows. If a fluid is poured into a hopper, it either flows through or it doesn't (if the funnel is too small and the capillary forces are too large). For granular particles, if the outlet is too small (about 5 particle diameters are considered to be the critical size), the nearly immediate formation of stable arches will clog the opening. In other words, static Coulomb friction can cause a complete breakdown of granular rheology. The typical solution in industrial applications is to apply sideways forces on the hopper, either by vibrating the apparatus or by simply hitting the outside with a hammer[75]. When the mean interaction time between granular particles increases and the density of the aggregate is so low that interactions are mainly binary collisions, the medium is usually called granular "gas". Granular gases play a role in phenomena such as aeolian transport. They are not considered in this thesis.

3.4.1 Rheology

Phenomenologically, granular flows are viscoplastic, like mud or foam. Before motion sets in, a friction dependent flow threshold needs to be overcome, and the flow itself obtains viscous-like behaviour through shear-rate dependence. A number of attempts exist to develop continuum theories for granular hydrodynamics[76] in analogy to the Navier-Stokes equations, but the uncertainty of time and length scales, together with the strong force fluctuations with minimal density fluctuations hamper their general application: Spacial averages in granular flows show much larger fluctuations than for ordinary liquids. Microscopic models of granular flows in simulations are, for simplicity's sake, predominantly based on round particles, with rather obvious consequence for their dynamics: Due to the lower energetic costs of rolling and no need to work against gravity, round particles will have significantly more mobility than elongated or polyhedral particles. The same applies for the implementation of friction. Incorrect friction force models may lead to wrong flow threshold or reduced energy dissipation, and give the particles more mobility than they would have in corresponding experiments, see for example the discussion in sec. 7.4. As consequence, the flow in these simulations will be, among other things faster and more spread out, compared to experiments and observations with realistic materials, see e.g. experiments with glass beads and aspherical sand by Forterre and Pouliquen[77] or Baxter[78]. Attempts have been made to mimic irregularly shaped particles by using clusters of spheres[79] or unrealistically high rolling friction coefficients[80], though the problems with unphysicality of these models remain. Treatment of friction remains similar questionable: While the lack of proper friction modelling can be less problematic for permanently excited configurations as opposed to static configurations, some effects can only be modelled with severe restrictions, or not at all. Consequently many researchers have resorted to mimic friction with rough surfaces or abandon it all together[81].

For the flow of granular particles, Bagnold found in 1954[82] that the velocity v of the particles scales with the depth of the flowing layer y as

$$v(y) = \frac{2}{3} I_0 \frac{\tan\theta - \mu_1}{\mu_2 - \tan\theta} \sqrt{\Phi \cos\theta} \left(\frac{h^{3/2} - (h-z)^{3/2}}{d^{3/2}} \right) \sqrt{gd}, \tag{3.1}$$

where I_0 is the in the rheology of dense granular flows, θ the angle of the layer with respect to the horizontal direction, Φ the volume fraction, h the height of the flowing layer and d the grain size. μ_1 and μ_2 are not the coefficient of Coulomb-friction, but parameter that summarize various energy dissipation mechanism and sometimes the arctan-dependence of the slope angle. For the use of two different (μ_1, μ_2) one has to keep in mind that the larger value represents the "angle of maximal stability" and the smaller value represents the "average angle of repose". From this equation one can derive the inclination in which a steady and uniform flow is possible as $\theta \in [\arctan(\mu_1), \arctan(\mu_2)]$, which is in agreement with observation[83]. In addition one finds that the critical angle for the flow to occur is dependent on the thickness of the layer. The Bagnold velocity profile is sketched in Fig, 3.13 a). Movement of a particle avalanche as a singe block due to the constraints of static friction leads to a different velocity profile, see Fig. 3.13 b).

Hydrodynamic considerations can not fully capture the phenomenology of granular rheology, so depending on the shape of a hopper, totally different flow patterns are possible, even for the same grains. If the walls of a hopper are sufficiently steep and smooth, then the entire aggregate is in motion, which is referred to as mass flow (sketched in Fig. 3.14 a). This does not mean, the flow profile is uniform throughout the aggregate. With increasing depth of the aggregate, increasing velocity differences will appear between the flow in the centre and the flow at the silo walls. However, if the walls are too flat or too rough,

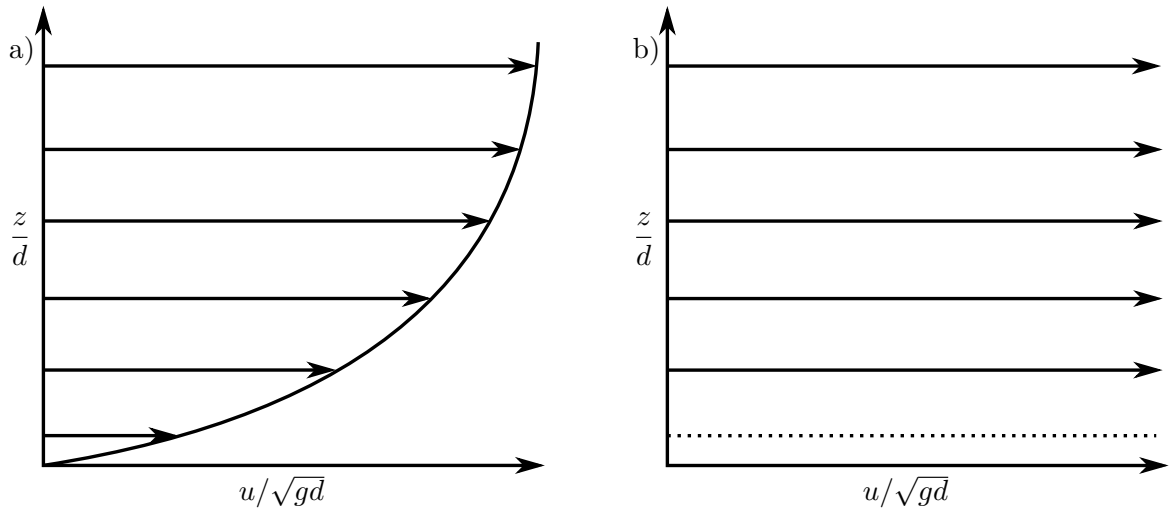

Fig. 3.13 Figure a) shows the Bagnold velocity profile for a particle flow down an inclined plane. Figure b) shows the velocity profile for an avalanche sliding down as a single block under the effect of inter-particle static friction. At the interface between the avalanche and the surface a particle layer with $v = 0$ is possible.

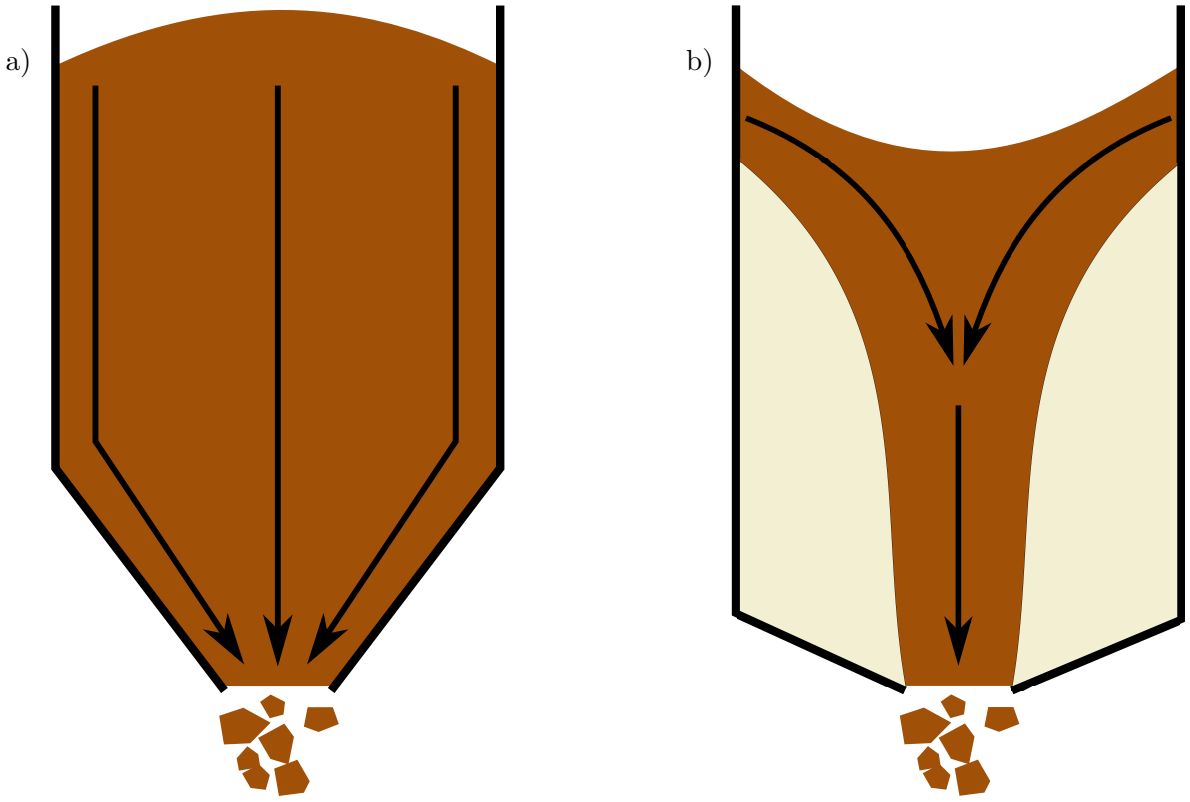

Fig. 3.14 Flow profiles: a) Massflow and b) Plugflow with dead zones of immobile particles (marked in beige)

then plug flow occurs (sketched in Fig. 3.14 b). Initially, only the particles in a narrow cone above the opening are moving. Particles outside this cone, with respect to their distance to the hopper walls, remain at rest until the cone has been emptied of particles. Those "dead zones" can propagate all the way to the top of the granulate, so that a clear depression is visible in the surface of the granulate. In general, the situation is less clear, than Fig. 3.14 may suggest. Dead zones might appear only in the bottom part of the silo, so that observation gives no indication of the flow profile, or they might occur asymmetric, even in symmetric containers, so that the flow profile becomes eccentric. Plug flow and mass flow can appear in mixed forms where some areas develop into dead zones and others show mass flow. Mass flow is particular susceptible to clogging, where stable arches form over the opening of the silo, depending on the size of the opening. Plug flow can easily lead to segregation in the dead zones, where particles may remain for a long time (i.e. first one in $\neq$ first one out).

3.4.2 Segregation

Granular materials show a particular unique feature, that is, they segregate under the influence of external force according to their size, shape or mechanical properties like friction or hardness. The probably most well known example is the so-called "Brazil nut" effect, in which a larger particle inside an assembly of smaller particles will rise to the

top when subject to vertical vibration[84]. While this seems counter-intuitive due to the increase in potential energy for the large particle, the explanation is rather simple: Smaller particles can easier penetrate into gaps below larger particles that are created by vibration, and slowly push the larger objects upward. In geophysical situations, this effect can be observed in rockslides and debris flow, where larger rocks and objects tend to ride on top and in front of of smaller objects[85].

To date, the influence of friction on granular segregation is only partially understood: Experiments have shown that an increase of the coefficient of friction can invert the segregated structure[86], some simulations reported a non-monotonous dependence of the segregation rate on the friction coefficient[87], while others associate convective motion with friction thresholds[88]. Unfortunately, in all these simulations, friction had been modelled as a purely dynamic force and the results should be taken with a grain of salt.

3.4.3 Liquefaction

Landslide-like processes usually occur when slopes have been stable for a long time. From the point of view of simulations, this means that a numerical model is required that can accurately reproduce long-term stability without any drift in the position. Undamped, or non-dampable oscillatory behaviour in the force laws (such as the Cundall-Strack friction model, see sec. 2.2) weaken the static phase. Oscillations in the force law can lead to resonances that can, without any physical cause, trigger slope failure or liquefaction, that is, the switch from a static phase to a liquid phase. Similar, models that store dissipated kinetic energy in a degree of freedom can release that energy as shock forces, destabilizing the static state. To simulate systems with external oscillatory forces (such as in earthquakes), friction needs to be modelled as a constraint force without any delay in its grip as optimal mechanism for energy dissipation. If an incorrect friction model introduces noise into such the simulation, the result will be unreliable. There are many cases where accurate modelling of liquefaction is necessary. In the shipping industry, for example, bulk carriers form large parts of the world merchant fleet ([89] 2016 values), as many goods

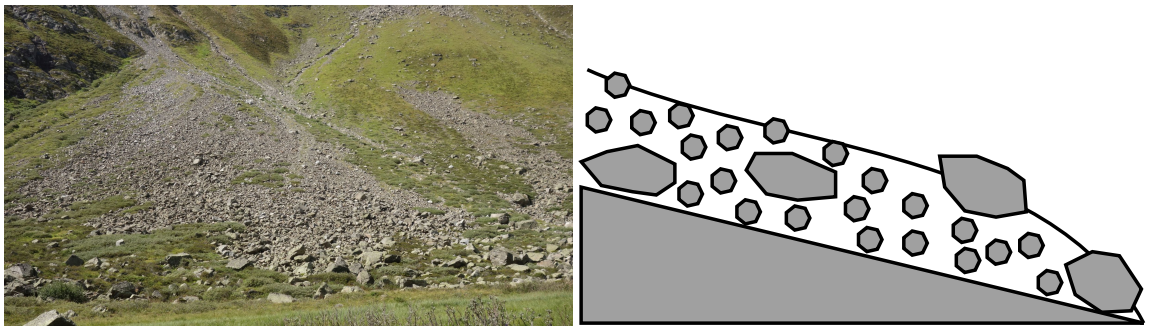

Fig. 3.15 Granular segregation in particle flows, such as rockslides, pushes larger particles to the outsides and the top of rockslides as smaller particles can easily penetrate below larger ones.

can only be transported in granular form, such as grains or ores. Cyclic forces from waves can easily set the cargo in motion and endanger the vessel[90]. In geological applications, liquefaction occurs during strong earthquakes[91, 92]: cyclic forces decrease the material strength of the ground, which can lead to damage of sub-surface and above-surface structures.

Chapter 4

The Discrete Element Method

The standard simulation method for granular materials is the discrete element method (DEM). Grains are modelled directly by grain shapes, without a need of homogenizing a volume element to a continuum. Granular shear is then just the relative slip between adjacent grains, while continuum approaches need again a "discretisation" to obtain shear bands. For round particles, the effect of solid friction is subdued, as particles can "escape" the grip via rolling. For the DEM in general, relative and not absolute velocities must be used. For polygonal particles in particular, forces are not central forces, so that torques must be included in the calculation, and the contact orientations can have arbitrary directions. A stable simulation in mechanics in general and with an exact implementation of Coulomb friction in particular, requires a force law with a smooth variation of the force magnitude, the force direction and the force point (for the computation of the torques). Time integration schemes are finite-difference methods, that are derived under the impression of smoothness of the forces. In case of jumps in the magnitude, position or direction of the forces, the simulation will not be stable.

Beyond the short outline of the force law in this section, details (about efficient computations, physical justification, treatment of penetrating overlaps and problems for shapes with curved boundaries other than circles) can be found in Matuttis et al.[16]. An extension for non-convex polygons is given in [93].

4.1 Rigid body kinematics in two dimensions

The common approach for discrete-element simulations uses a "hard particle, soft contact" method, i.e. the kinematics of individual particles is that of rigid bodies, but the force is calculated as a "penalty" based on the overlap between the particles. While the time integration is performed for the centres of mass, the friction computation requires the relative velocities and accelerations at the contact as sketched in Fig. 4.1. They can be computed from the corresponding rigid body relations for the relative velocity of a point P (which will later be the contact point) with respect to another point C (which will later

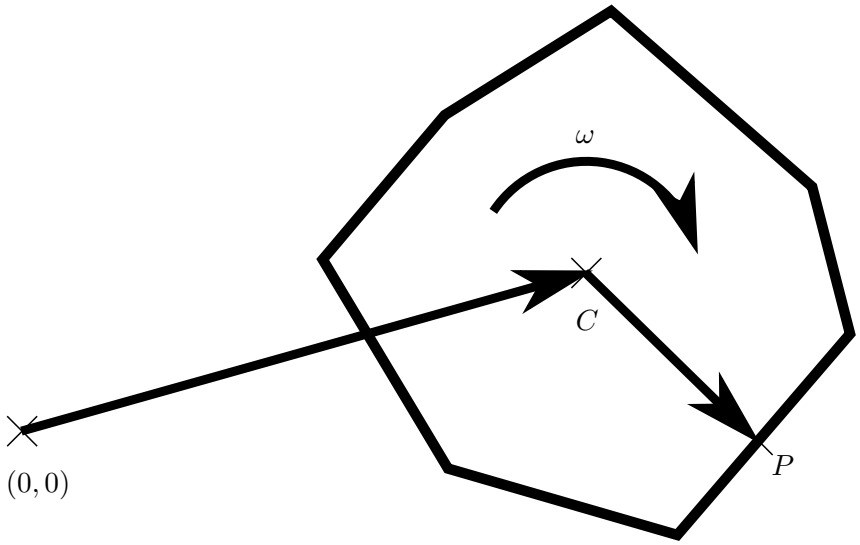

Fig. 4.1 Relative movement of a point P computed from another point C for rigid body kinematics.

be the centre of mass). For an angular velocity $\boldsymbol{\omega}$ around a point C at position $\boldsymbol{r}_C$, the velocities and accelerations can be obtained via the time derivatives. Using the vector $\boldsymbol{r}_{CP}$ pointing from C to P as well as the velocity $\boldsymbol{v}_C$ and acceleration $\boldsymbol{a}_C$ of point C, it is possible to represent the position vector $\boldsymbol{r}_P$ of the material point P, its velocity $\boldsymbol{v}_P$ and acceleration $\boldsymbol{a}_P$ as

$$\begin{aligned} \boldsymbol{r}_P &= \boldsymbol{r}_C + \boldsymbol{r}_{CP} && (4.1)\\ \boldsymbol{v}_P &= \boldsymbol{v}_C + \boldsymbol{\omega} \times \boldsymbol{r}_{CP} && (4.2)\\ \boldsymbol{a}_P &= \boldsymbol{a}_C + \dot{\boldsymbol{\omega}}\, \boldsymbol{r}_{CP} + \boldsymbol{\omega} \times [\boldsymbol{\omega} \times \boldsymbol{r}_{CP}]. && (4.3) \end{aligned}$$

For two dimensions, with angular velocity $\boldsymbol{\omega} = (0, 0, \omega)$

$$\begin{aligned} \boldsymbol{\omega} \times [\boldsymbol{\omega} \times \boldsymbol{r}_{CP}] &= \begin{pmatrix} 0 \\ 0 \\ \omega \end{pmatrix} \times \left[\begin{pmatrix} 0 \\ 0 \\ \omega \end{pmatrix} \times \begin{pmatrix} r_x \\ r_y \\ 0 \end{pmatrix} \right] && (4.4)\\ &= \begin{pmatrix} 0 \\ 0 \\ \omega \end{pmatrix} \times \begin{pmatrix} -\omega\, r_y \\ \omega\, r_x \\ 0 \end{pmatrix} && (4.5)\\ &= \begin{pmatrix} -\omega^2\, r_x \\ -\omega^2\, r_y \\ 0 \end{pmatrix} = -\omega^2 \begin{pmatrix} r_x \\ r_y \\ 0 \end{pmatrix}. && (4.6) \end{aligned}$$

Accordingly, for a two-dimensional polyhedral simulation, the relations eqs. (4.1-4.3) can be simplified with the vector $\boldsymbol{r}_{\overline{CP}}^{\perp} = (-r_y, r_x, 0)$ orthogonal to $\boldsymbol{r}_{CP}$ as

$$\begin{aligned} \boldsymbol{r}_P &= \boldsymbol{r}_C + \boldsymbol{r}_{CP} && (4.7)\\ \boldsymbol{v}_P &= \boldsymbol{v}_C + \omega\, \boldsymbol{r}_{\overline{CQ}}^{\perp} && (4.8)\\ \boldsymbol{a}_P &= \boldsymbol{a}_C + \dot{\omega}\, \boldsymbol{r}_{\overline{CP}}^{\perp} - \omega^2 \boldsymbol{r}_{CP}. && (4.9) \end{aligned}$$

These are the analytically exact relations for $\boldsymbol{r}_P, \boldsymbol{v}_P, \boldsymbol{a}_P$ based on the actual $\boldsymbol{r}_C, \boldsymbol{v}_C, \boldsymbol{a}_C$ and $\boldsymbol{r}_{CP}$. If $\boldsymbol{v}_P$ is approximated by finite difference approximations for $\boldsymbol{v}_C$, $\boldsymbol{a}_C$ and $\boldsymbol{r}_{CP}$ from the current and previous timestep, the numerical noise increases considerably and accuracy of the algorithm decays [94].

4.1.1 Elastic forces in normal direction

When rigid particles collide, their deformation is assumed to be neglectable and their shape preserved. The most simple model of a particle is a sphere, or a disc in two dimensions. Contacts can be identified very simple, i.e. if the sum of their radii exceeds the distance from their centres, and their penetration depth δ is larger than zero. A number of elastic contact force models have been derived from elastic theory for interactions between round particles, such as

- Hookean (linear dashpot) contacts, where the elastic force is proportional to δ, or
- Hertzian (viscoelastic) contacts, where the elastic force is proportional to $\delta^{3/2}$.

While round particles are computationally simple and allow to simulate systems of millions of particles, they are unphysical their dynamics will be dominated by rolling due to lower mechanical resistance and energetic costs. To fully capture the dynamics of granular particles, it is preferable to use non-round or polygonal shape instead. For polygonal particles, the overlap area is approximately proportional to δ, it is therefore practical to chose the magnitude of the elastic force as proportional to overlap area A (Fig. 4.2) as a measure of what would be the deformation in physical particle. This allows to reproduce all force regimes independent of the contact geometry. The overlap area can be computed from the intersection points S_1, S_2 and the force point P as the centroid of the overlap polygon. The tangential direction $\mathbf{t}$ (the direction of friction) is defined as the connecting line (S_1, S_2) between the intersection points, so the normal direction $\mathbf{n}$ is also fixed. Alternative definitions with weighted averages of (S_1, P) and (P, S_2), give negligible differences for sufficiently hard particles and small penetration depth.

Another important parameter is the particle hardness, i.e. a measure of its deformation or overlap, given by the Young's modulus. In two dimensions it corresponds to 1m long rod-like particles of the same cross section with the same numerical values for the Young's

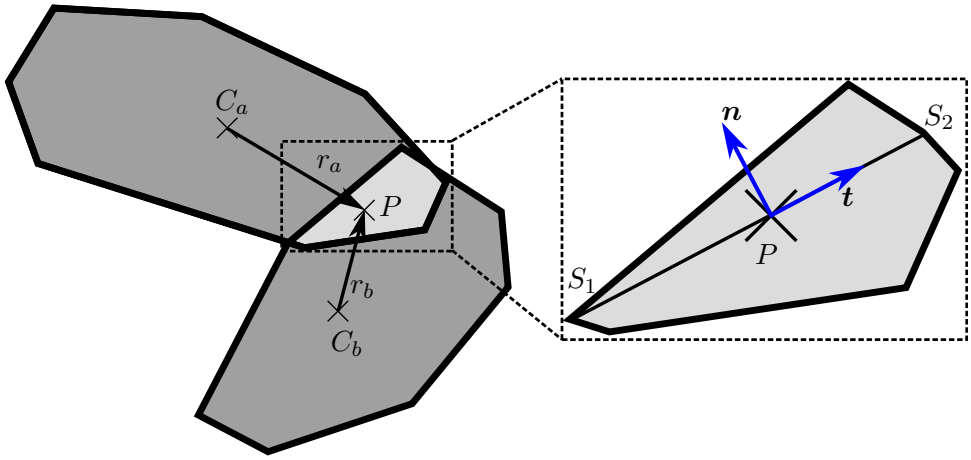

Fig. 4.2 Contact geometry for two polygonal particles (dark shading), showing their overlap (light shading), the polygons' centres of mass C_a, C_b, the centre of mass of the overlap polygon P and the contact vectors $\boldsymbol{r}_a, \boldsymbol{r}_b$ from C_a, C_b, to P (left). The inset (right) indicates the normal ($\mathbf{n}$) and tangential ($\mathbf{t}$) contact direction, given by the intersection points of the outlines. The overlap is considerably exaggerated compared to the 1/1000 of a linear particle extension for the simulations in this thesis.

modulus Y^{3D} with units [N/m^2]. The introduction of the "characteristic length"

$$l = 4\frac{|\boldsymbol{r}_a||\boldsymbol{r}_b|}{|\boldsymbol{r}_a| + |\boldsymbol{r}_b|} \tag{4.10}$$

for the contact vectors $\boldsymbol{r}_a, \boldsymbol{r}_b$ (see Fig. 4.2) between the centres of mass C_a, C_b and the contact point P allows to define the force in units of [N]. The definition of l in eq. (4.10) fixes the wave propagation in an assembly of space-filling rectangles to the sound velocity of the continuum material, $c = \sqrt{Y/\rho}$. With the two-dimensional Young's modulus Y, the overlap area A and the characteristic length l, the elastic normal force between to particles can be written as

$$F^{\mathrm{el,N}} = Y\frac{A}{l}. \tag{4.11}$$

4.1.2 Dissipative forces in normal direction

In collisions of granular particles part of their kinetic energy of their relative motion is dissipated. In analogy to the damped harmonic oscillator one can define a dissipative term for contacts proportional to the change of the overlap,

$$F^{\mathrm{diss,N}} = \gamma\sqrt{m_{\mathrm{red}}Y}\frac{\dot{A}}{l} \tag{4.12}$$

with a dimensionless damping constant γ and the reduced mass m_{red} of the contacting particles,

$$\frac{1}{m_{\mathrm{red}}} = \frac{1}{m_a} + \frac{1}{m_b}, \tag{4.13}$$

obtained from the masses m_a, m_b.

While for a linear oscillator the elastic and damping forces vary continuously, for approach and separation, the evolution of the damping force is not continuous: During approach and separation the damping force jumps to maximal values because the relative velocity is maximal(Fig. 4.3). As the elastic forces are minimal during the beginning and the end of a collision, this jump in the total normal force is significant. While the jump at approach can be somewhat justified, as impacts are non-smooth processes (as can be understood from the sound at impacts), the jump at separation to an attractive force violates the initial assumption that a repulsive interaction between particles should be modelled. If the jump in the force is larger than what the integrator can compensate, noise will be introduced into the force balance and the simulation may be destabilized. One can deal with this discontinuity by introducing "cut-offs", limiting the total force at separation,

$$F^{\mathrm{diss,N}} = \begin{cases} -F^{\mathrm{el,N}} & \text{for} \quad (F^{\mathrm{tot,N}} \cdot F^{\mathrm{el,N}}) < 0, \\ F^{\mathrm{diss,N}} & \text{else,} \end{cases} \tag{4.14}$$

and the dissipative force at approach,

$$F^{\mathrm{diss,N}} = \begin{cases} \mathrm{sign}(F^{\mathrm{diss,N}})|F^{\mathrm{el,N}}| & \text{for} \quad |F^{\mathrm{el,N}}| > |F^{\mathrm{diss,N}}|, \\ F^{\mathrm{diss,N}} & \text{else.} \end{cases} \tag{4.15}$$

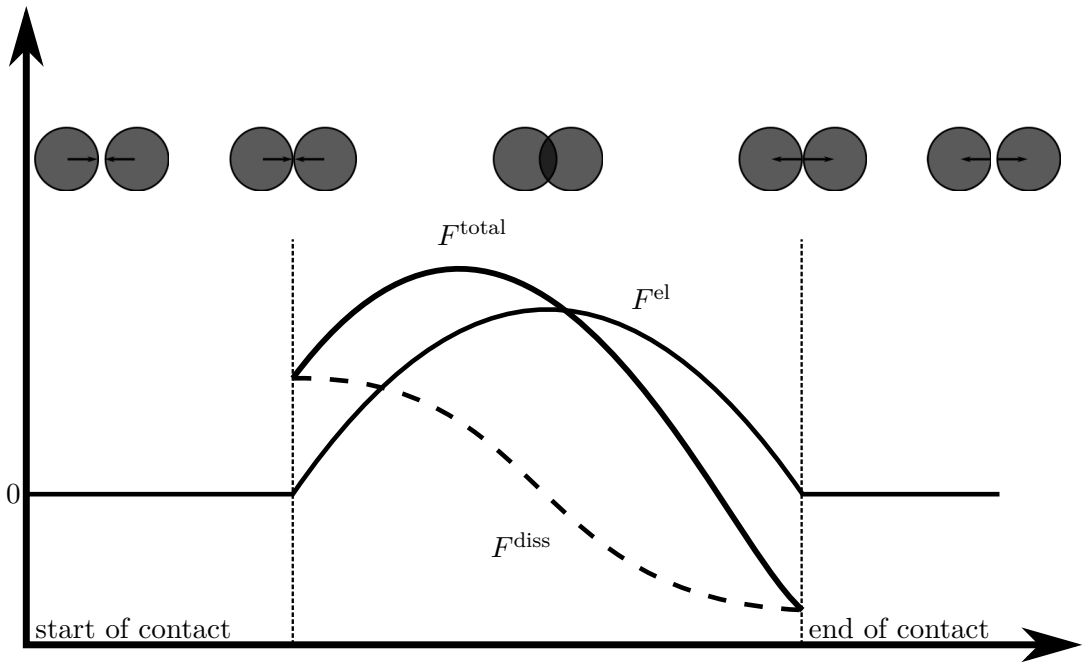

Fig. 4.3 Unphysical jumps in the force evolution for the elastic and dissipative force during approach and separation.

4.1.3 Tangential forces

For dry granular particles, the tangential interaction is primarily determined by Coulomb friction, of which the basic phenomenology has been introduced in chapter 1. Several different numerical models for static friction have been detailed in chapter 2. However, these models are either based on regularisation or can not be applied for arbitrary many-contact situations. Exact treatment of Coulomb friction will be the topic of chapters 5 and 6.

4.1.4 Total force and torque

To obtain the total force acting upon a particle the elastic and dissipative forces can be summed up with respect to their normal and tangential directions,

$$\boldsymbol{F} = \begin{pmatrix} F_x \\ F_y \end{pmatrix} = (F^{\mathrm{el}} + F^{\mathrm{diss}}) \begin{pmatrix} \boldsymbol{n}_x \\ \boldsymbol{n}_y \end{pmatrix} + F^{\mathrm{fric}} \begin{pmatrix} \boldsymbol{t}_x \\ \boldsymbol{t}_y \end{pmatrix} \tag{4.16}$$

The torques are computed from the normal and tangential forces, and for non-round particles even in the absence of tangential forces, as

$$\boldsymbol{T}_{a,b} = \boldsymbol{r}_{a,b} \times \boldsymbol{F}. \tag{4.17}$$

In the general case where there are no symmetries in the particle- and contact situation, there is no "actio=reactio" principle for the torques, different values for two particles in contact are not unphysical, i.e. $\boldsymbol{T}_a \neq \boldsymbol{T}_b$.

4.1.5 Threshold for "zero velocity"

In numerical (floating point) simulation, complicated expressions which are evaluated to exactly zero (or are rounded to zero due to underflow) hardly ever occur. Numerical precision of integrators and models will almost always lead to deviation from zero for relative positions, velocities, accelerations, etc.. We therefore must define a threshold for negligible (numerically zero) velocity based on the overlap computation. For the overlap area A_{cont} with a length of the contact line $l_{\mathrm{cont}} = (S_1, S_2)$ in Fig. 4.2, a penetration depth can be defined as

$$d_{\mathrm{pen}} = \frac{A_{\mathrm{cont}}}{l_{\mathrm{cont}}}. \tag{4.18}$$

For the BDF-integrators, the timestep τ must allow to resolve at least $1/10$ of l_{cont} or d_{pen} for contacts with forces of relevant size, else the simulation will become unstable due to the noise in the position computation. Accordingly, smaller length scales can be neglected, so that we obtain a threshold velocity as

$$v_{\mathrm{thresh}} = \frac{1}{10} \frac{\min(d_{\mathrm{pen}}, l_{\mathrm{cont}})}{\tau} \tag{4.19}$$

which is independent of particle parameters. Too large a prefactor will not do any damage, as it will only lead to more conditional tests in the friction formalism, whether case 3 in sec. 5.3.2 is valid or not, but it will not enforce the static friction condition.

4.2 Modelling errors

The common approach for discrete-element simulations (DEM) uses a "hard-particles, soft-contacts" model, where the forces are computed from the geometrical overlap of the undeformed shapes, while the equations of motion for individual particles are integrated out under the assumption of rigid particle shapes. As the contacts are not point-like, but extended, the particle rotation affects the magnitude and direction of the inter-particle forces.

Within a timestep τ, the orientation of the contacts can change by an angular increment $\Delta\varphi$ (Fig. 4.4) due to noise-like error in the orientation. Even if the overlap area may remain the same, the direction fluctuation leads to inconsistencies in the computation of the force equilibrium. As consequence, velocity dependent damping for the rectilinear degrees of freedom can no longer compensate the residual motion and the noise in the angular degrees of freedom spreads towards the rectilinear degrees of freedom.

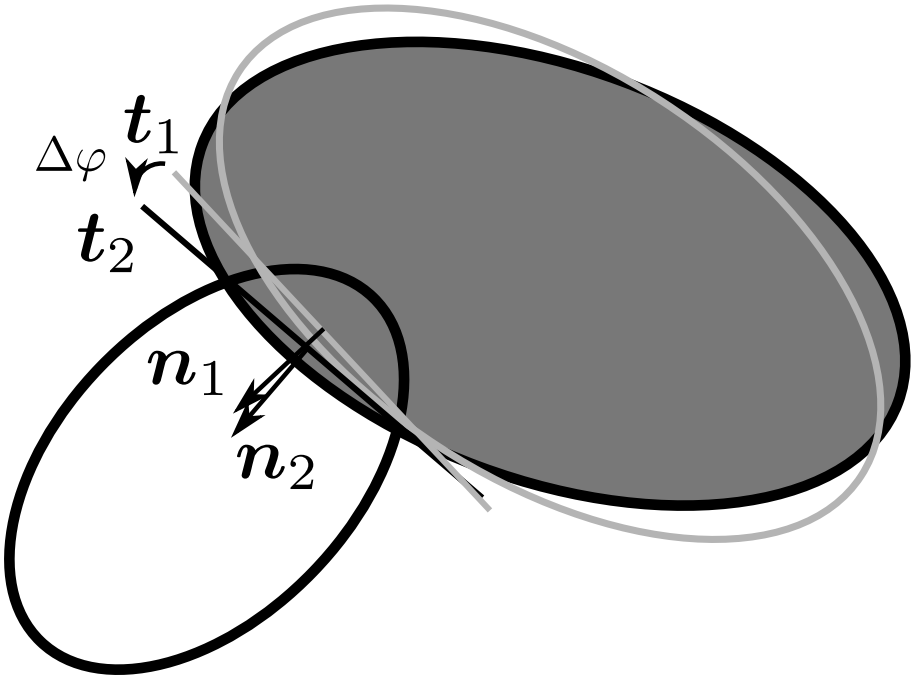

Fig. 4.4 In mechanical equilibrium, the forces and torques in a DEM-simulation should be balanced. Residual angular motion can induce small changes in the contact orientation $\Delta\varphi$. As consequence, the contact forces change, equilibrium is no longer maintained and the rectilinear degrees of motion experience noise.

Simulations of particle configurations which should give static configurations reveal in the actual simulation persistent, small, noisy vibration amplitudes around the equilibrium

positions[95]. This vibration influences granular assemblies like an external excitation, so for e.g. a granular heap or a granular assembly in a box, the height of the centre of mass decays during the whole simulation time, instead of the expected decay of the kinetic (vibration) energy to zero. The imperfect force balance around the equilibrium of position and orientation induces a fluctuating numerical error on the scale of the timestep and the particle overlap. While slip between particles scales with the timestep (see Fig. 7.18 in ch. 7) it is unfeasible to reduce the timestep and computational cost only to deal with that noise. For elongated particles, the effect occurs already for elastic forces alone, for round particles only when tangential forces (friction) are present.

4.3 Numerical integration

In two dimensions, the dynamics of granular particles are determined by two translational and one rotational equation of motion for their centre-of-mass coordinates,

$$\frac{\mathrm{d}\ddot{\boldsymbol{r}}}{\mathrm{d}t} = \frac{1}{m}\boldsymbol{F}, \tag{4.20}$$

$$\frac{\mathrm{d}\ddot{\varphi}}{\mathrm{d}t} = \frac{1}{I}T, \tag{4.21}$$

where the $\boldsymbol{F}$ is the entirety of all forces acting on the particle, including the interaction forces described in sec. 4.1.1 and the gravitational force, T is the entirety of the torques acting on the particle, including contributions from the tangential forces and contributions from shape, m and I are the mass and the moment of inertia, and $\boldsymbol{r}$ and φ are the rectilinear and angular coordinates of the particle. We obtain the time evolution of eqs. (4.20,4.20) by numerical approximated with the backward-difference formulae (BDF) in the Gear predictor-corrector form. The BDF method is an implicit method, its advantages for our purpose are higher stability and accuracy, and the ability to deal with stiff differential equations without generating additional noise compared with other numerical integration schemes. It is stable up to fifth order, beyond that they are guaranteed to have no convergence. In this work we mostly use a second order BDF (BDF2) approach, with a step

$$y_{n+1} - \frac{4}{3}y_n + \frac{1}{3}y_{n-1} = \frac{2}{3}\tau f(t_{n+1}, y_{n+1}). \tag{4.22}$$

In addition, some of our simulations also use a fifth order BDF (BDF5) for comparison.

4.3.1 Gear Predictor-Corrector Scheme

To solve the equations of motion we use the backward difference formulae (BDF) in the Gear predictor-corrector form. The BDF integrator does not require to separate the equations of motion into non-linear systems of equations, and is robust against small oscillations in the solution. Use of the Gear predictor corrector form requires three separate processes: computation of predicted coordinates and derivatives based on the values from

the previous timestep, evaluation of the forces, and correction of the predicted values based on the change in forces.

If $\boldsymbol{r}_n$ is the scaled n-th time derivative of a position vector $\boldsymbol{r}_0$,

$$\boldsymbol{r}_n = \frac{\tau^n}{n!}\frac{\mathrm{d}^n \boldsymbol{r}_0}{\mathrm{d}t^n}, \tag{4.23}$$

then we can predict the time-evolution for for the next timestep $t+\tau$ by simple application of the Taylor series,

$$\begin{pmatrix} \boldsymbol{r}_0^P \\ \boldsymbol{r}_1^P \\ \boldsymbol{r}_2^P \\ \boldsymbol{r}_3^P \\ \boldsymbol{r}_4^P \\ \boldsymbol{r}_5^P \end{pmatrix}(t+\tau) = \begin{pmatrix} 1 & 1 & 1 & 1 & 1 & 1 \\ 0 & 1 & 2 & 3 & 4 & 5 \\ 0 & 0 & 1 & 3 & 6 & 10 \\ 0 & 0 & 0 & 1 & 4 & 10 \\ 0 & 0 & 0 & 0 & 1 & 5 \\ 0 & 0 & 0 & 0 & 0 & 1 \end{pmatrix} \begin{pmatrix} \boldsymbol{r}_0^P \\ \boldsymbol{r}_1^P \\ \boldsymbol{r}_2^P \\ \boldsymbol{r}_3^P \\ \boldsymbol{r}_4^P \\ \boldsymbol{r}_5^P \end{pmatrix}(t), \tag{4.24}$$

based on the assumption, that the forces will not change. With the predicted values $\boldsymbol{r}_i^P$ the new accelerations can be computed. The corrector step then computes the final coordinates and derivatives based on the predictor step,

$$\begin{pmatrix} \boldsymbol{r}_0 \\ \boldsymbol{r}_1 \\ \boldsymbol{r}_2 \\ \boldsymbol{r}_3 \\ \boldsymbol{r}_4 \\ \boldsymbol{r}_5 \end{pmatrix}(t+\tau) = \begin{pmatrix} \boldsymbol{r}_0^P \\ \boldsymbol{r}_1^P \\ \boldsymbol{r}_2^P \\ \boldsymbol{r}_3^P \\ \boldsymbol{r}_4^P \\ \boldsymbol{r}_5^P \end{pmatrix}(t+\tau) + \begin{pmatrix} c_0 \\ c_1 \\ c_2 \\ c_3 \\ c_4 \\ c_5 \end{pmatrix}(t)\Delta\boldsymbol{r}. \tag{4.25}$$

The coefficients c_i depend on the order of the integrator and are given in table 4.1. Second order Gear predictor.corrector integrators are also called BDF2, while fifth order Gear predictor-corrector schemes are referred to as BDF5. $\Delta\boldsymbol{r}$ is the difference between the predicted and corrected p-th order derivatives for a p-th order differential equation. For the second order equations of motion, $\Delta\boldsymbol{r}$ is the difference in acceleration, respective forces.

Table 4.1 Gear corrector coefficients for second order differential equations with velocity dependent forces of order two to five.

Order	c_0	c_1	c_2	c_3	c_4	c_5
2	0	1	1			
3	1/6	5/6	1	1/3		
4	19/90	3/4	1	1/2	1/12	
5	3/16	251/360	1	11/18	1/6	1/60

4.3.2 Choosing the timestep

As the normal force is modelled in analogy to a harmonic oscillator, we can estimate an oscillation frequency for a contact between two particles as

$$\omega = \frac{1}{l}\sqrt{\frac{Y}{\rho}}, \tag{4.26}$$

where l is the characteristic length, Y the Youngs' modulus of the material and ρ is the density. For a collision of particles, the contact time then is

$$\tau^{\mathrm{col}} = \pi l \sqrt{\frac{\rho}{Y}}. \tag{4.27}$$

For BDF solvers, the simulation remains stable if the contact is resolved with ten or more timesteps, so the optimal timestep will be

$$\tau^{\mathrm{opt}} \sim \frac{1}{10}\tau^{\mathrm{col}}. \tag{4.28}$$

4.4 The discrete element method in three dimensions

This section briefly explains the a polyhedral approach to three-dimensional DEM simulations as a generalisation of the two-dimensional approach in section 4.1. A more detailed explanation is found in [16] or [95]. The variation of the force parameters (magnitude, force point, direction) is smooth, so the force model is suited for implementation with numerical integrators. An overview of the change in relation and parameters from one- to three dimensions is given in table 4.2.

4.4.1 The elastic force in three dimensions

The elastic force is a generalisation from two dimensions, as in eq. (4.11), to three dimensions. Instead of the overlap area, we now use the volume V of the overlap polyhedron to compute the elastic force as

$$|F^{\mathrm{el,N}}| = Y\frac{V}{l}, \tag{4.29}$$

with the Young's modulus Y and the overlap length l is the same as in the two dimensional case, eq. (4.10), with the lengths of the vectors $\boldsymbol{r}_1$ and $\boldsymbol{r}_2$ connecting the centres of mass of the interacting particles with the force point. Also in three dimensions, the simulation remains stable if the collision is resolved with 10 or more timesteps, so the optimal timestep is the same as in two dimensions, eq. (4.28). As the force point, we chose the centroid C_0 of the overlap polyhedron. If there are no penetrating contacts, then the overlap polyhedron of two convex polyhedrons will be convex itself. The intersection of the particle surfaces form a "contact line" of the overlap polyhedron, see Fig. 4.5 a). The area enclosed within

Table 4.2 Evolution of the force law and the parameters from the one-dimensional linear oscillator to the force law for two- and three-dimensional discrete elements.

	1D	2D	3D
	chains of particles	2D surfaces of 3D rods	3D particles
		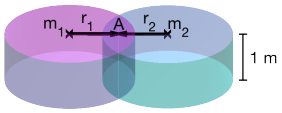	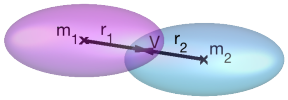
characteristic length l	$\lvert x_2 - x_1 \rvert$	$\frac{4\lvert \boldsymbol{r}_1 \rvert \lvert \boldsymbol{r}_2 \rvert}{\lvert \boldsymbol{r}_1 \rvert + \lvert \boldsymbol{r}_2 \rvert}$	$\frac{4\lvert \boldsymbol{r}_1 \rvert \lvert \boldsymbol{r}_2 \rvert}{\lvert \boldsymbol{r}_1 \rvert + \lvert \boldsymbol{r}_2 \rvert}$
stiffness	k [N/m]	Y^{2D} [N/m]	Y^{3D} [N/m^2]
Strain	x	$\frac{A}{l}$	$\frac{V}{l}$
Damping	$\gamma\sqrt{mk}$	$\gamma\frac{\sqrt{mY^{\mathrm{2D}}}}{l}$	$\gamma\sqrt{m\frac{Y^{\mathrm{3D}}}{l^3}}$
Strain rate	$v = \dot{x}$	$\dot{A}$	$\dot{V}$
$c^{\mathrm{sound}}\left[\sqrt{\frac{\mathrm{N}}{\mathrm{kg/m}}}\right]$	$\sqrt{\frac{kI}{m/l}}$	$\sqrt{\frac{Y^{\mathrm{2D}}}{\varrho^{\mathrm{2D}}}}$	$\sqrt{\frac{Y^{\mathrm{3D}}}{\varrho^{\mathrm{3D}}}}$

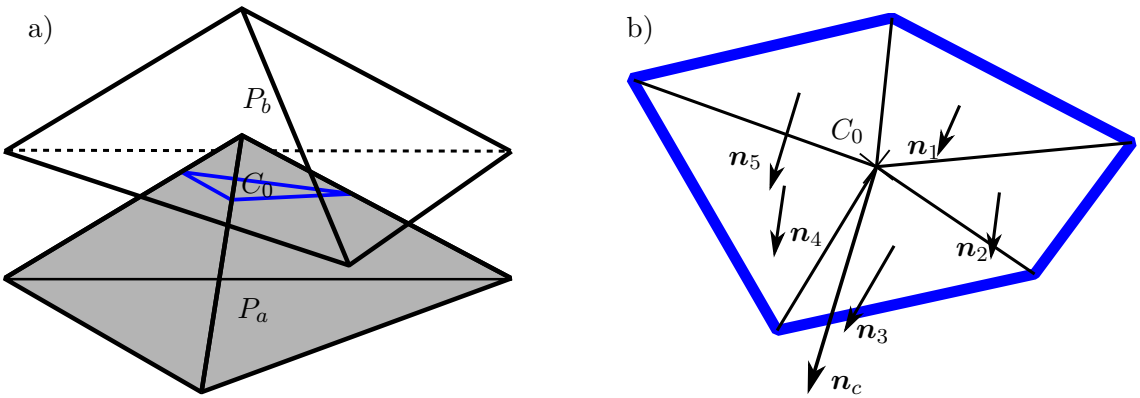

Fig. 4.5 Sketch of the contact geometry between three-dimensional discrete elements, in equivalency to the two-dimensional case in Fig. 4.2. a) Sketch of the contact line (blue) of two intersecting tetrahedra P_a and P_b and the centroid of the overlap tetrahedron C_0. b) Contact area of a different overlap polyhedron, separated into several triangles around the centroid C_0. The normal direction of the overlap area can be determined by the area weighted average of the normal directions of the triangles.

the contact line can be split into k triangles oriented around the centroid. We can then determine a unique normal direction $\boldsymbol{n}_c$ of the contact as the area weighted average of the normal vectors of each individual triangle,

$$\boldsymbol{n}_c = \frac{\sum_{i=1}^{k} A_i \boldsymbol{n}_i}{\sum_{i=1}^{k} A_i}, \tag{4.30}$$

which gives us the direction of the force, see Fig. 4.5 b).

Finally, the torques acting on particles a and b are given by the total force $\boldsymbol{F}$ and the contact vectors,

$$\boldsymbol{T}_a = \boldsymbol{r}_a \times (+\boldsymbol{F}), \tag{4.31}$$

$$\boldsymbol{T}_b = \boldsymbol{r}_b \times (-\boldsymbol{F}). \tag{4.32}$$

4.4.2 Normal and tangential directions of the force point

In analogy to the two-dimensional case, the normal direction $\boldsymbol{n}$ in three dimensions is defined as the weighted average of the normals of the contact triangles. The tangential direction is the vector rejection between the contact normal and the direction of the contact velocity. Then, the tangential velocity is the projection of the relative velocity onto the tangential contact plane $\mathcal{T}$,

$$\boldsymbol{v}_{\text{rel}}^{\text{tan}} = \text{P}(\boldsymbol{v}_{\text{rel}}|\mathcal{T}), \tag{4.33}$$

based on the relative velocities at the contact point,

$$\boldsymbol{v}_{\text{rel}} = \boldsymbol{v}_a - \boldsymbol{v}_b, \tag{4.34}$$

and likewise the tangential acceleration

$$\boldsymbol{a}_{\text{rel}}^{\text{tan}} = \text{P}(\boldsymbol{a}_{\text{rel}}|\mathcal{T}) \tag{4.35}$$

as the projection of the relative acceleration, with the relative accelerations at the contact point,

$$\boldsymbol{a}_{\text{rel}} = \boldsymbol{a}_a - \boldsymbol{a}_b. \tag{4.36}$$

As the contact geometry defines only the normal direction $\boldsymbol{n}$, the vectors spanning the tangential space are undefined, and we can freely choose two linear independent vectors in $\mathcal{T}$ as the spanning set, see Fig. 4.6. The obvious choice is to take the direction of the relative tangential acceleration as one of the spanning vectors,

$$\boldsymbol{t}_1 = \frac{\boldsymbol{a}_{\text{rel}}^{\text{tan}}}{|\boldsymbol{a}_{\text{rel}}^{\text{tan}}|}. \tag{4.37}$$

The remaining vector $\boldsymbol{t}_2$ is then the unit vector perpendicular to $\boldsymbol{t}_1$ and $\boldsymbol{n}$. With that, we now have three unique, linear independent vectors spanning the three-dimensional contact-space.

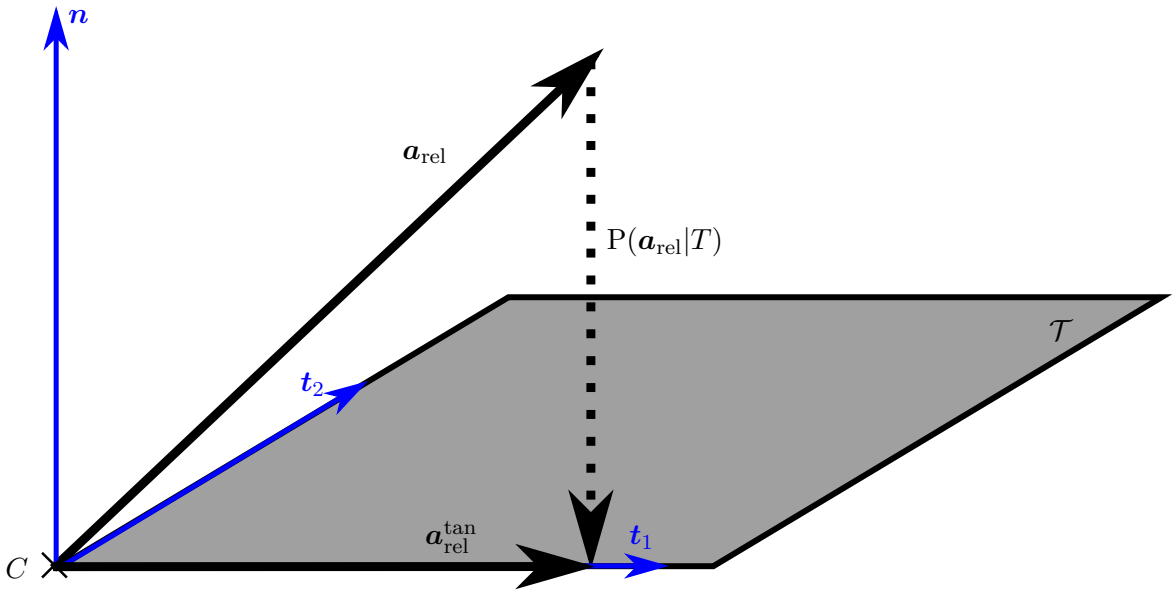

Fig. 4.6 The projection $P(\boldsymbol{a}_{\text{rel}}|\mathcal{T})$ of the relative acceleration $\boldsymbol{a}_{\text{rel}}$ into the contact plane $\mathcal{T}$ is unique, and therefore the direction of the static friction is unique too.

Chapter 5

Constraint forces and the character of static friction as a constraint

In this chapter, we revisit friction from the standpoint of a numerical realization of the unequality constraint, eq. (1.2). Whereas for non-zero velocity, dynamic friction is a dissipative force, at zero velocity, static friction is a multi-valued, non-dissipative constraint force. We introduce the mathematical framework of Differential Algebraic Equations (DAE) which is the mathematical framework for a "numerically exact" treatment of static friction. We then develop the formalism for static Coulomb friction for a single particle by means of the frictional linear oscillator as example.

5.1 Differential algebraic equations

In numerical analysis, constraint problems are treated under the name of differential algebraic equations (DAE). Loosely speaking, for ordinary differential equations (ODEs), the state of motion is computed from the forces, while for DAEs, the forces are computed from the state of motion, i.e. the constraints. Because we make use of the terminology and concepts for DAEs in our problem of static friction, this section gives a short overview with the point pendulum as example. This will allow the reader to trace the similarities in the derivation of constraint forces for bilateral constraints (given by an equality, as for pendulum length) and unilateral constraints (given by an inequality as for the static friction).

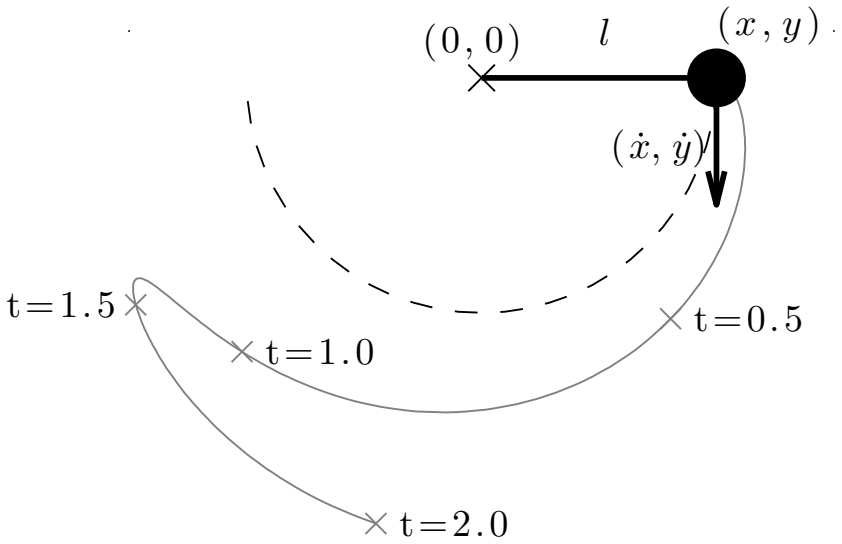

Fig. 5.1 Pendulum with the centre in the origin, with position vector (x, y) and velocity vector $(\dot{x} = v_x, \dot{y} = v_y)$ and the theoretical trajectory (dotted line) as well as an unphysical (due to inconsistent initial values) trajectory (grey, solid line).

5.1.1 Point pendulum

For the point pendulum in Fig. 5.1 with the centre at the origin, the trajectory has to fulfil the constraint function

$$g(x, y) = x^2 + y^2 - l^2 = 0, \tag{5.1}$$

for the coordinates x, y and the pendulum length l. The x, y in $g(x, y)$ are not the momentary position values but the whole field of coordinates $(x(t), y(t))$ which fulfil the condition $g(x, y) = 0$.

Such "bi-lateral" constraint as in eq. (5.1), i.e. equalities, are easier to deal with than "uni-lateral" constraints with inequalities like the static friction in eq. (1.2) where the bilateral equations have to be derived yet. Eq. (5.1) can be rewritten as scalar product of vectors $(x, y) = \mathbf{x}$ as

$$g(\mathbf{x}) = \mathbf{x} \cdot \mathbf{x} - l^2 = 0, \tag{5.2}$$

in vector analysis notation to improve the readability. Constraint equations $g(\dots) = 0$ are written with a zero right hand side so right hand sides of the higher time derivatives of $g(\dots)$ vanish accordingly. (In contrast to derivatives of individual coordinates, derivatives of constraint equations do yield new independent equations.) The time derivative for $g(\mathbf{x})$ in eq. (5.2) yields

$$\dot{g}(\mathbf{x}) = \mathbf{x} \cdot \dot{\mathbf{x}} = 0. \tag{5.3}$$

This means that the vector $\mathbf{x}$ for the position must be orthogonal to the velocity vector $\dot{\mathbf{x}}$. While physically obvious, it is gratifying to see how the condition can be obtained by purely formal manipulation. Another time derivative is necessary to obtain conditions for

the constraint forces $\tilde{\mathbf{f}}$,

$$\ddot{g}(\mathbf{x}) = \ddot{\mathbf{x}} \cdot \mathbf{x} + \dot{\mathbf{x}} \cdot \dot{\mathbf{x}} = 0. \tag{5.4}$$

With the external forces $\mathbf{f}$ and constraint forces $\tilde{\mathbf{f}}$, Newton's equation becomes

$$\left(\mathbf{f} + \tilde{\mathbf{f}}\right) = m\,\ddot{\mathbf{x}} \tag{5.5}$$

Inserted into eq. (5.4) this yields twice the kinetic energy,

$$\left(\mathbf{f} + \tilde{\mathbf{f}}\right) \cdot \mathbf{x} = -m\,\dot{\mathbf{x}} \cdot \dot{\mathbf{x}} = -2T^{\text{kin}}. \tag{5.6}$$

The time derivative of the kinetic energy with eq. (5.5) is

$$\dot{T}^{\text{kin}} = m\,\ddot{\mathbf{x}} \cdot \dot{\mathbf{x}} = -\left(\mathbf{f} + \tilde{\mathbf{f}}\right) \cdot \dot{\mathbf{x}} \tag{5.7}$$

Because the constraint forces cannot perform work (d'Alembert's principle of virtual work) or affect the kinetic energy, one has

$$\tilde{\mathbf{f}} \cdot \dot{\mathbf{x}} = 0, \tag{5.8}$$

which means constraint forces and velocities are orthogonal, $\tilde{\mathbf{f}} \perp \dot{\mathbf{x}}$. Due to the orthogonality between velocity and coordinate vector in eq. (5.3) the constraint forces must be parallel, i.e. proportional to the coordinate vector,

$$\tilde{\mathbf{f}} = \lambda \mathbf{x}. \tag{5.9}$$

Inserted in eq. (5.6), this yields

$$\lambda = \frac{-\mathbf{f} \cdot \mathbf{x} - m\,\dot{\mathbf{x}} \cdot \dot{\mathbf{x}}}{\mathbf{x} \cdot \mathbf{x}}. \tag{5.10}$$

So the constraint force is proportional to the kinetic energy and to the external forces as well as inverse proportional to the pendulum length.

5.1.2 Drift away from the constraint

Next, the equations of motion for the pendulum are integrated with constraint forces from eq. (5.9,5.10) via the adaptive integrators from MATLAB's[96] ode-suite[97]. First, the low-order ode23 (order 2 and 3, Bogacki-Shampine[98]) is used. For $m = 1$, $g = 9.81$ and initial conditions $v_0 = (0, 0)$, $x_0 = (1, 0)$: The pendulum length is not constant, a numerical drift occurs in the 3rd digit, see Fig. 5.2. It is rather disconcerting that not only is the drift nearly the same for both absolute tolerances $\epsilon = 10^{-3}$ and $\epsilon = 10^{-5}$, but for smaller ϵ one gets a higher drift, i.e. larger error. Reference runs with the higher order ode45 integrator (Dormand-Prince [99]), in Fig. 5.3 are even more unsettling: The timestep τ is slightly reduced (as is to be expected for higher order methods) but for the same error

tolerances, the drift Δl is two orders of magnitude larger, up to $\Delta l = 0.1$ for a radius $r = 1$ in the time interval from $t = 0$ to $t = 0.4$. It sounds paradox that a higher order method gives a lower accuracy. Programming errors can't be the reason, as only the names of the integrator were exchanged. Nevertheless, it should not be forgotten that accuracy considerations assume smooth input data (forces, velocities, …). Constraint forces are noisy when the constraint is even slightly violated due to the ever present numerical noise. This noise is fed back into the time integration, so that (explicit) high order integrators are affected by the noise (deviation from smoothness of the input data) in high order. Lower order integrators, as a rule, show a more benign behaviour.

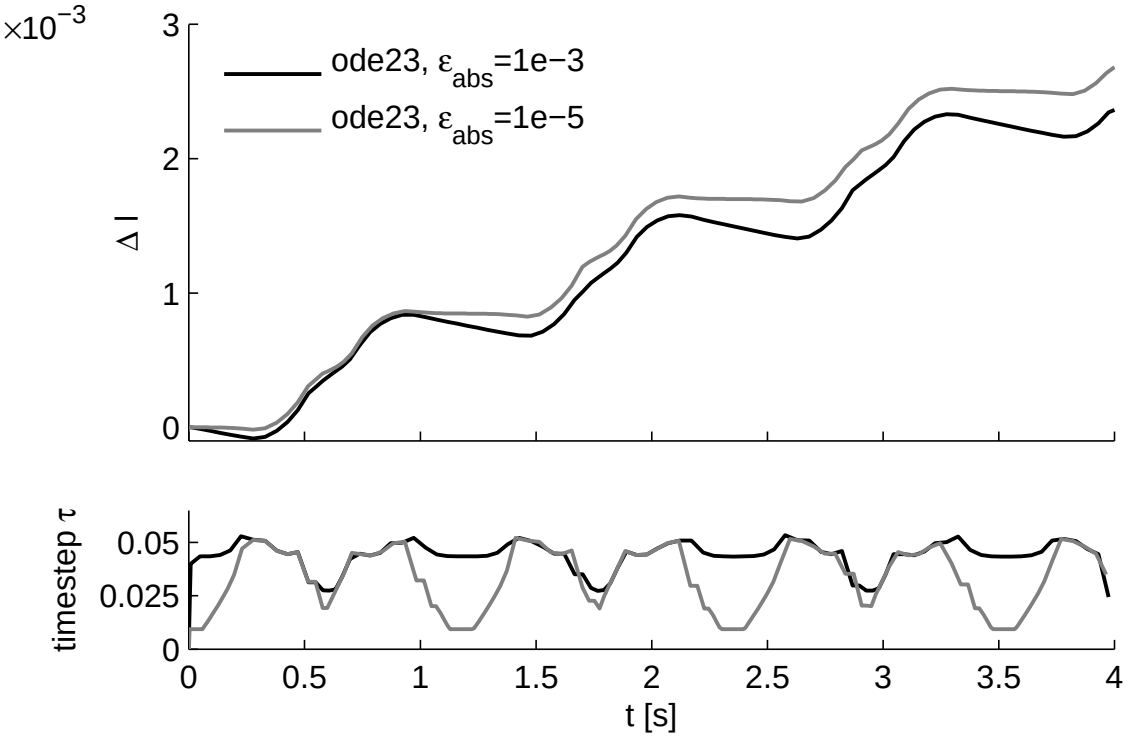

Fig. 5.2 Drift Δl for MATLAB's ode23 (above) and respective timestep τ (below) for the radius of the pendulum problem away from $l = 1$ with different tolerances ϵ_{abs} : The integration with the smaller tolerance shows the larger drift.

5.1.3 Stiffness and time integrator

Integrators which are less affected by such noise are the (implicit) stiff integrators. The otherwise rather technical text of Hairer and Wanner[1] introduces stiffness of ODEs rather un-technically as "problems where explicit solvers don't work". Some of the reasons that may lead to stiff ODEs are:

Stability is more important than accuracy: Variation of the timestep has little influence on the solutions of stiff problems with stiff solvers.

Multiple time-scales in the problem. Problems involving several different time-scales, like

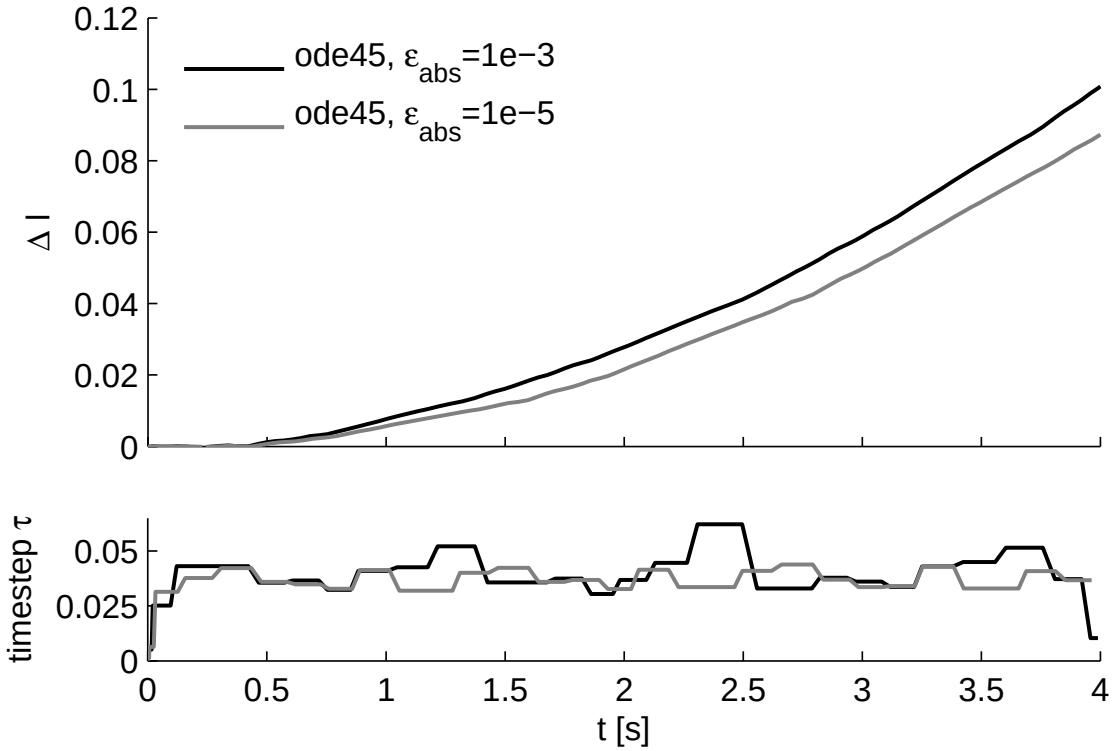

Fig. 5.3 Drift Δl for MATLAB's ode45 (above) and respective timestep (below) for the radius of the pendulum problem away from $l = 1$ with different tolerances ϵ_{abs} : The integration with the smaller tolerance shows the smaller drift.

a ball bouncing on the floor as in Fig. 5.5, often lead to stiff ODEs. Stiff solvers may be able to ignore some of the time-scales altogether.
Stiff solvers work better than non-stiff solvers. While this pragmatic definition sounds tautological, it has long been used in numerical analysis, e.g.[1].
Implicit solvers which are efficient for stiff problems are often called "stiff solvers", with additional criteria[1] for numerical stability.

For the purpose of this work, the central point is that DAEs are always stiff problems, and the issue is not one of accuracy (getting a numerical solution which is close to an exact solution) but of stability (getting a numerical solution which fulfils the constraint at all). Accuracy tolerances ε of adaptive integrators only monitor the deviations between solution components, but not the conformity to the constraint eq. (5.4). Drift depends on the numerical noise, which fluctuates rather randomly so that a higher drift with smaller tolerances ε as in Fig. 5.2 becomes possible. From eq. (5.2) to eq. (5.3), the pendulum length l has been dropped so the time integrator cannot prevent the drift away from the original length. While the deviation of the pendulum length Δl increases up to only 10%, the deviation from the orthogonality spikes up to $\Delta\alpha = 30°$ (30%).

When not mentioned otherwise, the Backward Difference Formula (BDF, "Gear Predictor corrector")[100] of second order (BDF2) is used for the time integration as it produced

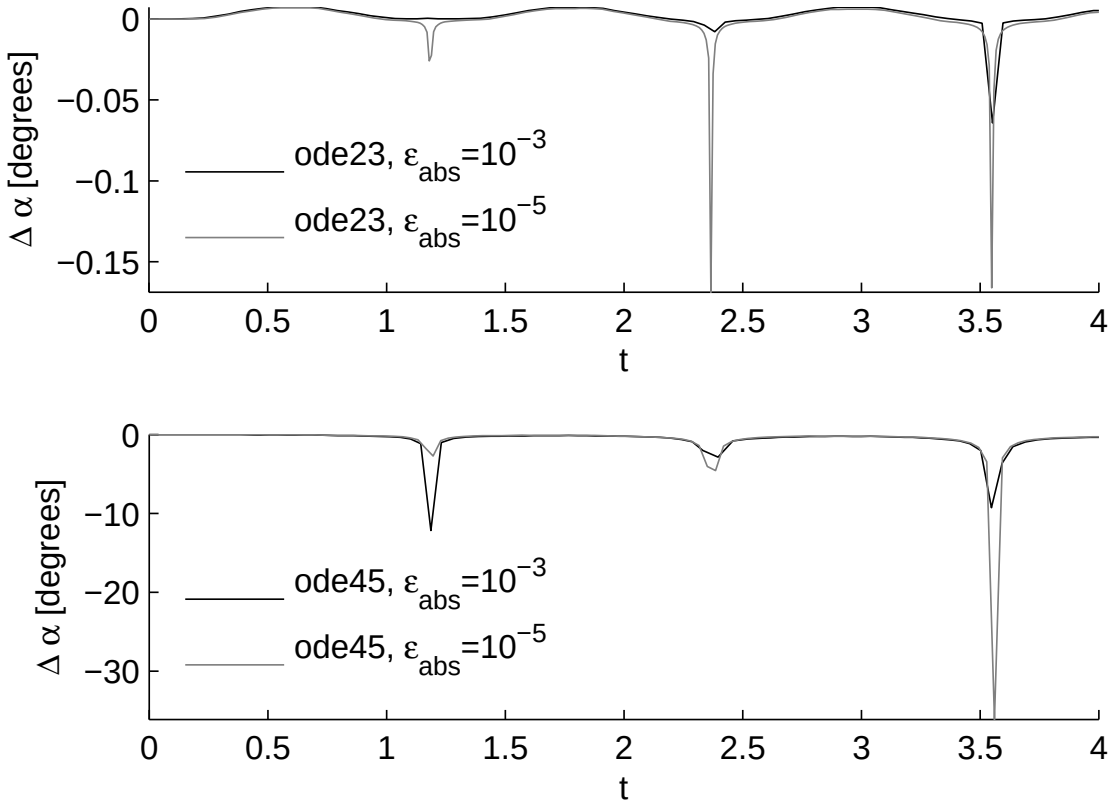

Fig. 5.4 Drift $\Delta\alpha$ of the angle between position and velocity vector from 90° for MATLAB's ode23 (above) and ode45 (below) with different error tolerances.

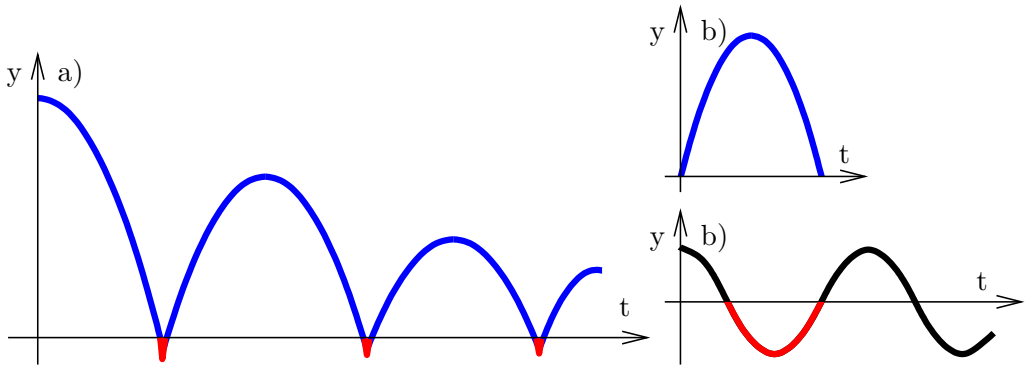

Fig. 5.5 a) The bouncing ball as an example for a problem with multiple timescales. The free-flight parabola b) can be integrated with higher timestep than the linear oscillations during bouncing off the floor c).

minimal drift compared to other BDF-methods[1]. BDF-integrators are implicit as well as stiffly stable. The predictor-values are only intermediate values for force calculation, computed under the assumption of constant forces from the previous timestep, only the corrected values (computed based on the change of the forces) are physical quantities. For

[1]BDF-methods are multistep-methods. Higher order methods use more previous timesteps, with a larger "distance" from the current position and a correspondingly higher deviation of the constraint, so nothing is gained by using higher order methods for this problem.

a timestep τ, explicit integrators of order τ^n insert noise of the order τ^{n+1}. This noise excites eigen-oscillations of contacting particles, so a timestep must be chosen which can resolve these oscillations. In contrast, a beneficial property of "stiffly stable" integrators (like that of the BDF-family) is that they "find" the equilibrium positions without additional oscillations and can in principle be used with much larger timesteps: This is the reason why stiffly stable integrators are used for constraint problems, which often have very high oscillation frequencies. The analytical relation of Newtonian kinematics

$$a = \dot{v} = \ddot{x} \tag{5.11}$$

for accelerations, velocities and positions holds for finite difference approximations (time integrators) only in the limit of infinitesimal timesteps, while each time integrator based on finite differences replaces eq. (5.11) with its own finite difference approximations.

5.1.4 Numerical stabilization of the constraint

It is possible to stabilize the DAE-solution so that the drift away from the constraint is limited. A classical approach by Baumgarte[101, 1] was to introduce parameters $\gamma^{\text{stab}}, \kappa^{\text{stab}}$ so that a linear oscillator around the constraint,

$$\ddot{g}(x) + \gamma^{\text{stab}}\dot{g}(x) + \kappa^{\text{stab}}g(x) = 0, \tag{5.12}$$

leads to a damped oscillation back to the constraint as sketched in Fig. 5.6 a). The difficulty with this approach for many particles and contacts is to find appropriate $\gamma^{\text{stab}}, \kappa^{\text{stab}}$ to make the implementation effective, not just conserve random oscillations. Therefore, the more recent, more controllable approach is to take the projection[102, 103, 1] of the solution into the subspace of the constraint function: In that case, taking a vector of length l would correspond to "stabilization by projection of the position" and taking a velocity orthogonal to the position vector would be "velocity projection" as in Fig. 5.6 b). Compared to the error in the position $\epsilon(x)$, the error in the velocity is magnified by the timestep $\epsilon(v) \approx \epsilon(x)/\tau$, so velocity stabilization is more important than position stabilization. For proofs that the accuracy order of the integrator is not affected by the stabilization by projection, see Hairer and Wanner[1] and references therein.

5.1.5 Inconsistent initial values

When one intentionally specifies velocities which violate the orthogonality condition with the position vector from eq. (5.3), the simulation result becomes unstable and usually either diverges to infinity as in Fig. 5.1 (grey line) or converges to zero. This situation for DAEs is called "inconsistent initial values" in numerical analysis. The computation of consistent initial conditions can be rather complex: When the constraint equations are non-linear, the solution of a non-linear system becomes necessary, as in the example by Hairer et al.

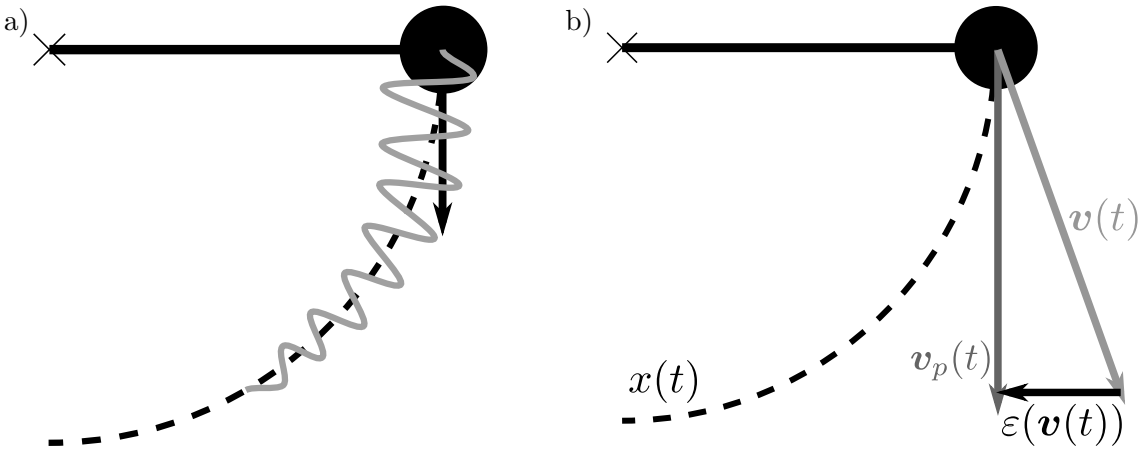

Fig. 5.6 Exact constraint (dashed) with stabilization after Baumgarte in a) and velocity projection in b).

[1], where Newton iterations have been used to solve the resulting equations. For ordinary differential equations, any combination of initial values can be chosen. Various numerical issues of DAEs in comparison to ODEs, like stability as well as the problem of "inconsistent initial values" are summarized in the article "Differential-algebraic equations are not ordinary ODEs" (ordinary differential equations) by L. Petzold[104].

5.2 The dynamical system

It will turn out later that the discrimination between static and dynamic friction is based on the dynamical system, i.e. the flow in phase space (with position- and velocity coordinates). Coulomb friction introduces a "non-smooth right hand side", so we review here the basic properties of dynamical systems of ordinary differential equations with "smooth" right hand sides. An ordinary differential equation (ODE)[2] with vectorial y, $\dot{y}$, f,

$$\dot{y} = f(y,t) \tag{5.13}$$

is called autonomous if $f(y,t) = f(y)$, i.e. the "right hand side" does not depend on time, else it is called non-autonomous. For physics, Newton's equation of motion is of second order and is represented as first order equation for

$$y = \begin{pmatrix} x \\ \dot{x} \end{pmatrix} = \begin{pmatrix} x \\ v \end{pmatrix} \tag{5.14}$$

[2]Conventionally in mathematics, Leibniz' notation is used to denote x as the independent and y as the dependent quantity, while in physics, Newtons notation is used to denote x as the dependent and t as the independent quantity. This leads to confusion about the character of x if mathematics and physics notation is used in the same text, and therefore a hybrid notation is chosen with y as the dependent variable which may depend on $x(t)$, $\dot{x}(t)$ and t. The most notable examples which use this notation are the books by Hairer and Wanner[51, 1] and the MATLAB-documentation.

so that

$$\dot{y} = \begin{pmatrix} \dot{x} \\ v \end{pmatrix} = \begin{pmatrix} v \\ a \end{pmatrix}. \tag{5.15}$$

In physics, linear oscillations without external force correspond to autonomous systems in mathematics, while with external forces they correspond to non-autonomous systems. The flow of the differential equation in mathematical terminology is the totality of curves[105]

$$\Phi(t) = \begin{pmatrix} x(t) \\ \dot{x}(t) \end{pmatrix}, \tag{5.16}$$

which can be obtained as individual solutions of the ODE $\varphi(x, v, t)$ with various initial conditions (x_0, v_0, t_0). As a rule, there is no mathematical limitation to the choice of (x_0, y_0, t_0). Limitations have usually been made based on physical considerations, i.e. causality or energy decay instead of increase. The flow $\Phi(t)$ of a differential equation is also called its "dynamical system". Any solution curve $\varphi(t) \in \Phi(t)$ corresponds to a certain initial condition (x_0, v_0). For autonomous systems, according to eq. (5.13), with differentiable right hand sides, two solution curves $\varphi(x_1, v_1)$ and $\varphi(x_2, v_2)$ either do not intersect or one is part of the other. If the solution of the ODE with the given initial conditions is a constant, the $\varphi(t) \equiv u$ is a fixpoint in phase space. According to mathematical theory (see e.g. [106, 107, 108]) for smooth right hand sides $f(y, t)$ the phase flow (dynamical system) can contain one or several of the following four different attractors:

1. The phase space trajectory is a closed loop, $\varphi(t)$ is periodic, i.e. there is a period $p > 0$ for which $\varphi(t + p) = \varphi(t)$. For a mechanical system without external force, that means energy is conserved (Fig. 5.7a). These kind of trajectories are commonly referred to as circle or sometimes as vortex.

2. The phase space trajectory follows a spiral towards a fixpoint, the attractor, i.e. $\varphi(t_0) > \varphi(t_1)$ for $t_0 < t_1$. The energy of the mechanical system decays (Fig. 5.7b). These kind of trajectories are commonly referred to as vortex or sometimes as spiral.

3. The trajectories asymptotically move away from the saddle point, i.e. $\varphi(t_0) \neq \varphi(t_1)$ for $t_0 \neq t_1$. For a mechanical system, this means that the system has a net energy gain (Fig. 5.7c). These kind of trajectories are commonly referred to as saddle.

4. The trajectories intersect at a single point in phase space, the node, i.e. $\varphi(t_0)$ has identical solutions for different initial conditions (Fig. 5.7d).

To analyse the properties of a differential equation, it is useful to define a phase space volume as hull around certain initial conditions and to study its transport in $\Phi(t)$. Traditionally, cat heads are used to illustrate the behaviour of the phase flow[3]. In symplectic

[3]Their use was popularised by Arnold[109], but probably "invented" by his teacher Delaunay according to Zdravkovska et al.[110].

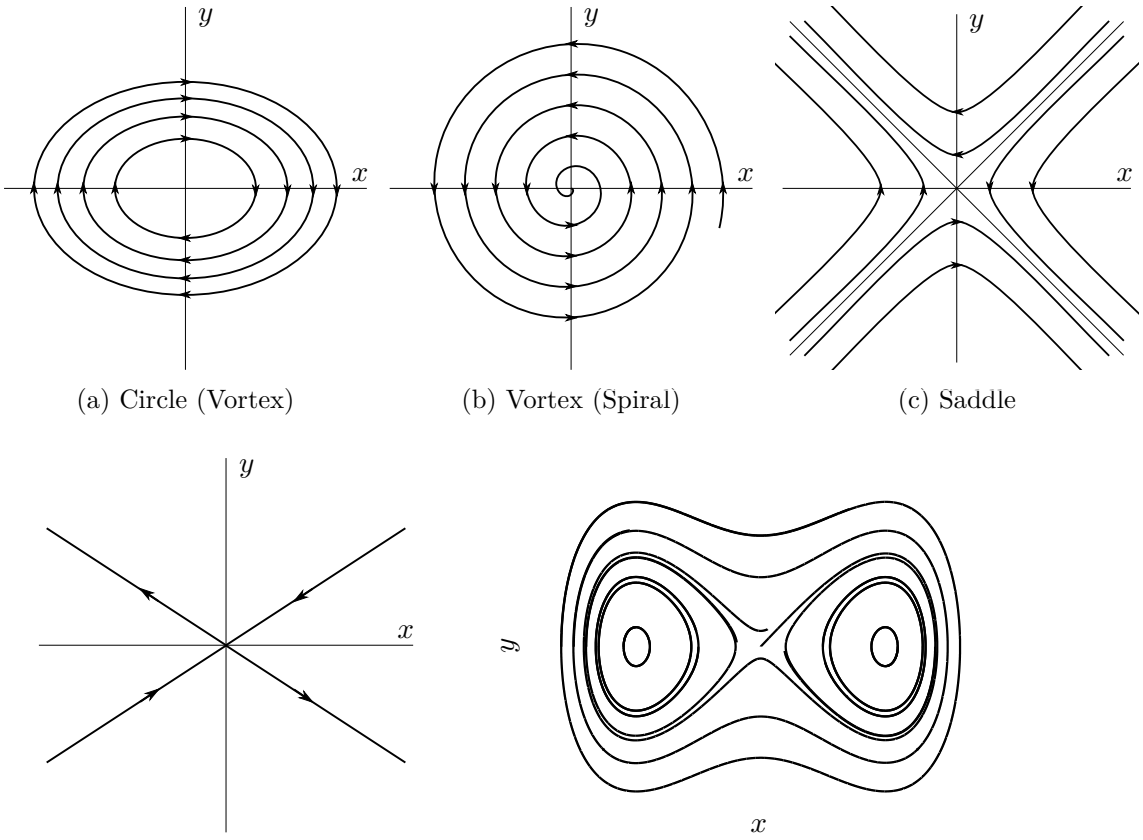

(a) Circle (Vortex) (b) Vortex (Spiral) (c) Saddle

(d) Node (e) Phase space with fixpoints, periodic trajectories and a saddle point.

Fig. 5.7 Possible attractors for ordinary differential equations in a) to d) and a global flow configuration in e) with one node and two circles.

systems the head does not change in size, i.e. is a conserved quantity, illustrating Liouville's theorem that the density of the phase space is conserved. Such systems are called symplectic (for linear symplectic systems, additionally the shape of the cat's head is conserved.) For a linear oscillator with viscous damping, energy is lost, and the phase space volume contracts exponentially as for the attractor in Fig. 5.8b due to the exponential decay of amplitude and velocity. The trajectories in the phase space spiral towards a fixed point. The direction field of the flow field is its time derivative, for a mechanical system obeying Newton's equation of motion,

$$\dot{\Phi}(t) = \begin{pmatrix} \dot{x}(x,\dot{x}) \\ \ddot{x}(x,\dot{x}) \end{pmatrix} = \begin{pmatrix} v(x,\dot{x}) \\ a(x,\dot{x}) \end{pmatrix}. \tag{5.17}$$

As the solution of the ODE is continuous, the direction field has no singularity, and the fixpoint in the centre of the spiral can not be reached in finite time.

The classical theory of ODEs[107, 106, 108] considers only equations with continuous right hand sides, like eq. (5.13). The right-hand sides for systems with Coulomb-friction $\propto \mu\,\mathrm{sign}(v)$ are not continuous due to the jump at $v = 0$. Oscillators with Coulomb

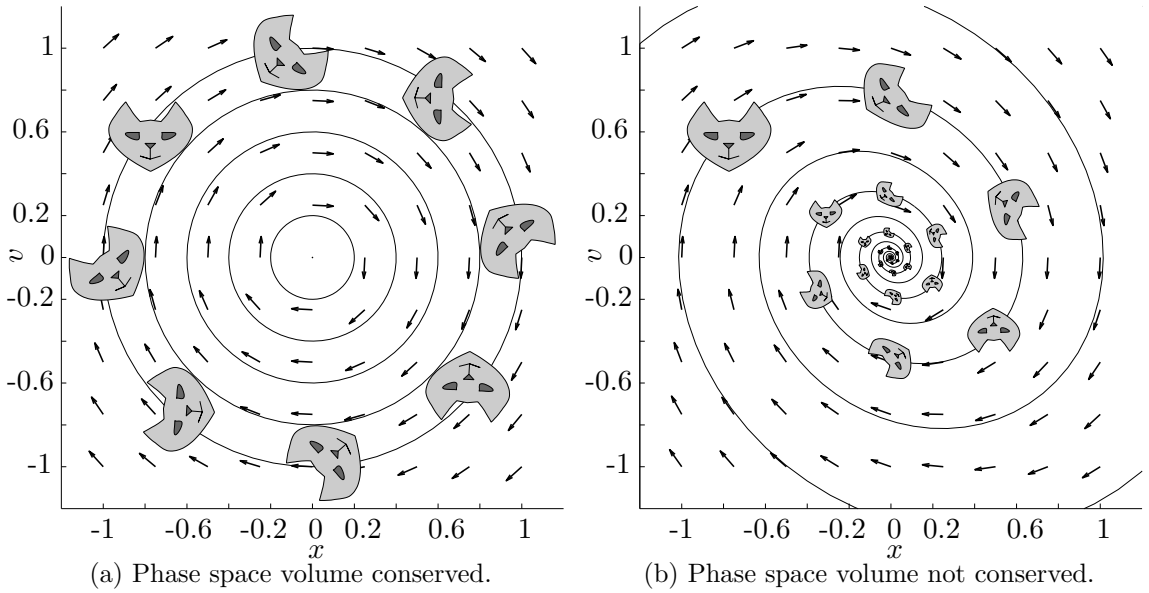

(a) Phase space volume conserved.

(b) Phase space volume not conserved.

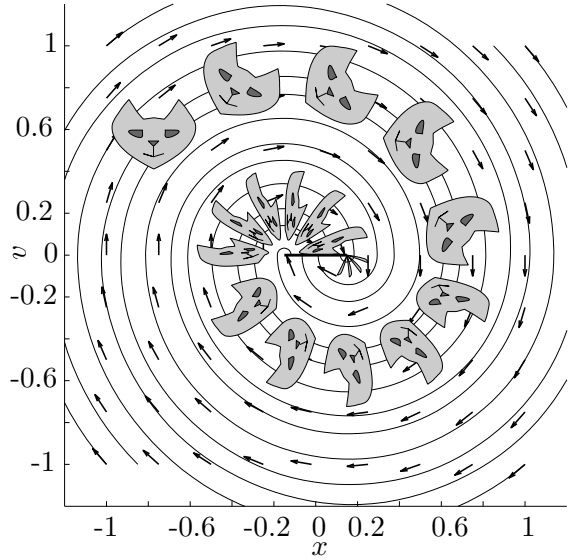

(c) Phase flow for a discontinuous system.

Fig. 5.8 Phaseflow for the linear oscillator without damping in (a), viscous (velocity dependent) damping in (b), and Coulomb friction in (c). While the flow Φ is continuous in a) and b), it is discontinuous in c).

friction therefore can not be treated in this mathematical framework (proof of existence and smoothness of solutions, etc.) due to the breakdown of the epsilon-delta continuity condition. Originally, the approach to solve such systems was to separate the phase flow on each side of the constraint and evaluate it separately[111]. This was generalised by A.F. Filippov with a "convex" interpolation as mentioned in ch. 2.6 for differential equations with discontinuous right hand sides. His approach allowed to describe phase flow appropriate for the static friction discontinuity. The numerical approach for a frictional oscillator by Hairer and Wanner[1] is based on this theory.

It will turn out that this is the phase flow which is necessary to discriminate between static and dynamic Coulomb friction. For an undamped linear harmonic oscillator

$$m\ddot{x} + kx = 0, \tag{5.18}$$

the trajectories in phase space are concentric circles around the origin (see Fig. 5.8a).

With the introduction of damping (viscous friction, proportional to the velocity)

$$m\ddot{x} + b\dot{x} + kx = 0, \tag{5.19}$$

with damping constant b, the energy is no longer conserved. The trajectories of the flow become spirals towards the fixpoint $(x = 0, v = 0)$ (Fig. 5.8b). Because the solution decays with an exponential envelope, the total energy in the system never becomes zero in finite time.

For systems with Coulomb friction,

$$m\ddot{x} + \mu F^{\mathrm{N}} \mathfrak{sgn}(\dot{x}) + kx = 0, \tag{5.20}$$

where μ is the friction coefficient, and the following "sign"-relation (in the sense of a multi-valued inclusion)

$$\mathfrak{sgn} \begin{cases} = 1 & \text{for } \dot{x} > 0 \\ \in [-1, 1] & \text{for } \dot{x} = 0 \\ = -1 & \text{for } \dot{x} < 0 \end{cases} \tag{5.21}$$

to indicate that the friction is multi-valued for $\dot{x} = v = 0$. Away from the friction constraint, the flow is continuous and similar to the viscous case. However at $\Phi(x, \dot{x}) = \left(-\frac{\mu F^{\mathrm{N}}}{k} \leq x \leq +\frac{\mu F^{\mathrm{N}}}{k}, \dot{x} = 0\right)$ the flow becomes discontinuous. The phase volume of the solution contracts, and the flow runs into a line between $-\frac{\mu F^{\mathrm{N}}}{k}$ and $+\frac{\mu F^{\mathrm{N}}}{k}$ (Fig. 5.8c), which will turn out to be the constraint manifold for Coulomb friction: $v = 0$ is possible for $|kx| < \mu |F^{\mathrm{N}}|$ (Fig. 5.9), i.e. the spring force is smaller than the static friction force. It is possible to deal with the sign-function by separating the phaseflow into two separate parts,

$$m\ddot{x} = \begin{cases} -\mu F^{\mathrm{N}} - kx & \dot{x} > 0, \\ +\mu F^{\mathrm{N}} - kx & \dot{x} < 0, \end{cases} \tag{5.22}$$

which will be important later.

In the general mathematical treatment of ordinary differential equations with discontinuous right hand sides A.F.Filippov showed[2] that phase flows converging towards the discontinuity at $\Phi(x, v = 0)$ result in a line of stationary points, equivalent to a static solution, see Fig. 5.10. "Modern" approaches with Lebesgue integration allow to formulate the phase flows for discontinuous ODE without constructing the explicit trajectory which is obtained from the theory of Filippov. While this is considered to be "more elegant" by the mathematics establishment, it is of very limited usefulness, as the formalism has no

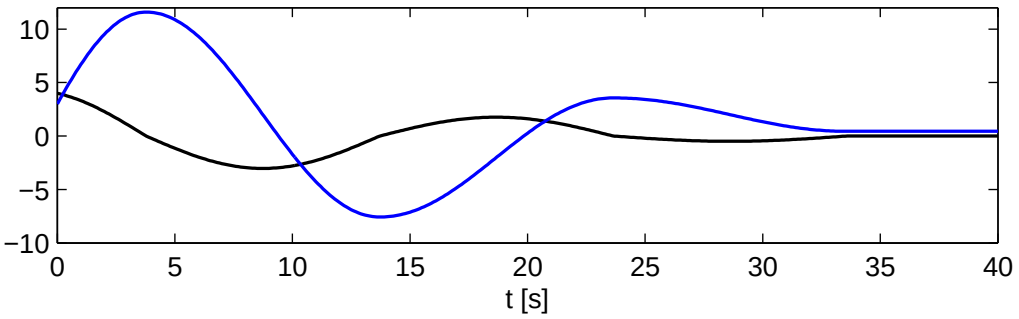

Fig. 5.9 Velocity (black) and position (blue) for the frictional oscillator with $m = 1, k = 0.1, \mu = 0.2$ with the values taken from[1]. When the kinetic energy is used up and $|kx| < \mu|F^{\mathrm{N}}|$, the velocity reaches zero.

equivalent in terms of classical trajectories or their finite differences approximations[112].

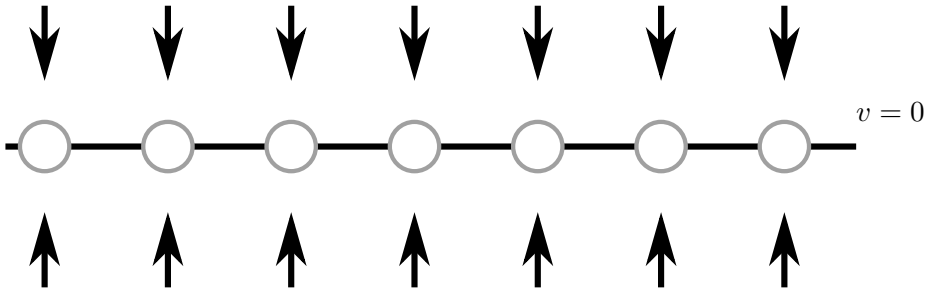

Fig. 5.10 Stationary points for the phase flow at a discontinuity.

As mentioned in chapter 2.3, Moreau, based on Lebesgue-integration, developed a generalisation for ODEs called differential inclusions[113]. As it replaces Riemann integration with Lebesgue integration, it is unsuitable for Newtonian kinematics (where velocities are time derivatives of positions), so a generalisation of kinematics (with the definition of accelerations also for non-smooth varying velocities) becomes necessary. In particular, no attention is paid to the different definitions of stability which are commonly used in numerical analysis.

The mathematical theory prefers to discuss low-dimensional attractors, usually two-dimensional (three dimensional in the case for truly chaotic attractors). That the attractor theory is also valid and relevant for higher dimensions is taken for granted in the mathematical literature. In the same logic, we will start with the discussion of the one-dimensional frictional contact in an absolute coordinate system, and take for granted that the formalism can be applied to the high-dimensional problem of many one-dimensional (tangential) contacts in many-body systems.

5.3 Numerically exact formalism for a single point mass

While the approach by Hairer and Wanner[51] is brilliant, the exposition is opaque at best and misleading at worst. This section gives a streamlined formulation with considerable simplification of the notation and the physical model.

The original approach by Hairer and Wanner employs adaptive integrators and can be considered to be "numerically exact", i.e. the friction computation is only affected by rounding errors, while the trajectory computation is, of course, affected by the discretisation of the time integrator. As a constant timestep is preferable for our simulations, we will develop necessary adaptation.

5.3.1 Phase flow for the linear oscillator

A practical formalism to compute static friction must determine whether a contact is static or not. As this discrimination is best done in phase space, it is important to understand the phase flow of the linear frictional oscillator with damping

$$m\ddot{x} + \gamma\dot{x} + \mu F^{\mathrm{N}}\mathrm{sign}(\dot{x}) + kx = 0, \tag{5.23}$$

with mass m, damping constant γ, friction coefficient μ and spring constant k. The flow of the dynamical system in phase space $\Phi(x(t), v(t))$ is plotted in Fig. 5.11 for different parameters. For the "symplectic" (energy-conserving, $\gamma = 0$ and $\mu F^{\mathrm{N}} = 0$) case in Fig. 5.11 a), the positions are $\propto \sin\left(\sqrt{\frac{k}{m}}t\right)$, the velocities $\propto \cos v$, so trajectories are closed circles in phase space. With viscous damping ($\gamma = 0.75$, $\mu F^{\mathrm{N}} = 0$) in Fig. 5.11 b), the circles degenerate into spirals towards $\Phi(x = 0, v = 0, t = \infty)$ due to the additional prefactor of $\exp\left(-\frac{2\gamma}{m}\,t\right)$ in the solution. The dry friction case in Fig. 5.11 c) is substantially different: With $\gamma = 0$ and $\mu F^{\mathrm{N}} = 0.3$, the trajectories are only spirals as long as the energy is large enough: Once $|kx| < \mu F^{\mathrm{N}}$, the flow is "trapped" at $v = 0$ in the interval $\left[-\frac{\mu F^{\mathrm{N}}}{k} \le x \le +\frac{\mu F^{\mathrm{N}}}{k}\right]$. For this static friction, the non-smooth right hand side is obtained by rewriting eq. (5.23) as

$$m\ddot{x} = \begin{cases} -\gamma\dot{x} - kx - \mu F^{\mathrm{N}} & v > 0, \\ -\gamma\dot{x} - kx + \mu F^{\mathrm{N}} & v < 0. \end{cases} \tag{5.24}$$

5.3.2 Identification of static friction

The flow in Fig. 5.11 c) for dry friction is different from the viscous case in Fig. 5.11 b). In the case of static friction, the flow $\Phi(x, v = 0)$ is pulled from above and below into the $v = 0$ axis, which is shown in in higher magnification in Fig. 5.12. For the regions I ($v > 0$) and II ($v < 0$) one can define the auxiliary quantities (to be consistent with Hairer and

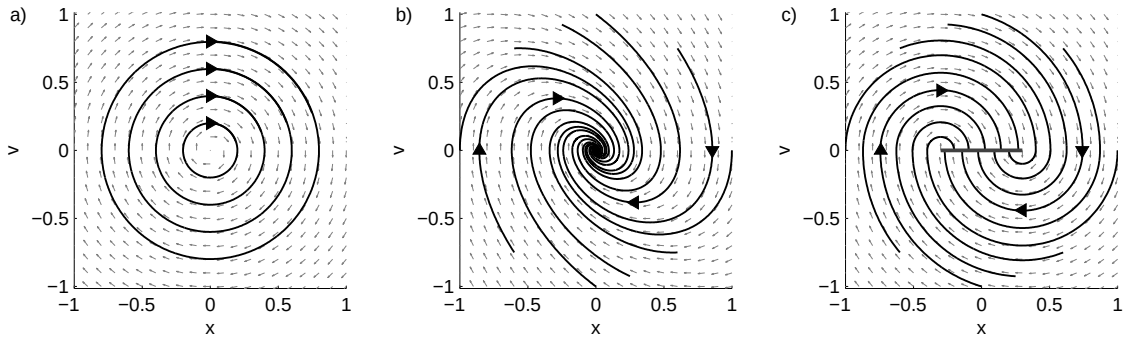

Fig. 5.11 Phase flow $\Phi(x, v, t)$ for a linear oscillator with $m = 1$ and $k = 9.81$ in a),with additional viscous damping $\gamma = 0.75$ in b) and with dry friction $\mu F^{\mathrm{N}} = 0.3$ without viscous damping in c). Direction of the flow field indicated by grey unit vectors, particular trajectories by bold lines with the flow direction indicated by an arrow symbols.

Wanner[51]) as

$$a_I = a(t) \quad \text{in region I}, \quad v < 0, \tag{5.25}$$

$$a_{II} = -a(t) \quad \text{in region II}, \quad v > 0, \tag{5.26}$$

based on the accelerations $a(t)$. (What to do with $v \approx 0$ will be discussed later in sec. 5.4.5.) This choice of sign for a_I, a_{II} will simplify the relations later on. For first order differential equations, Hairer and Wanner [51] proposed finite difference approximations for a_I, a_{II} in their version of eqs. (5.25,5.26), which were originally intended for first order differential equations and rather tedious to use for mechanics. In mechanics, the direct use of the acceleration $a(t)$ in eqs. (5.25,5.26), is simpler and more reliable. With these a_I, a_{II}, it is possible to discriminate the following cases:

Case 1. $a_I > 0; a_{II} < 0$: The flow crosses $\dot{x} = 0$ from $\dot{x} < 0$ to $\dot{x} > 0$, the friction is dynamic with a jump from $+\mu F^{\mathrm{N}}$ to $-\mu F^{\mathrm{N}}$.

Case 2. $a_I < 0; a_{II} > 0$: The flow crosses $\dot{x} = 0$ from $\dot{x} > 0$ to $\dot{x} < 0$, the friction is dynamic, with a jump from $-\mu F^{\mathrm{N}}$ to $+\mu F^{\mathrm{N}}$.

Case 3. $a_I < 0; a_{II} < 0$: The flow is pulled into $\dot{x} = 0$, we have static friction with a value that will rarely be f_I or f_{II}, but a value in between.

Case 4. $a_I > 0; a_{II} > 0$: This case is hypothetical and not obvious from Fig. 5.12. The flow would be non-unique along $v = 0$ and would pull away from $v = 0$ in opposite directions. This situation corresponds to the Painlevé-paradox, which which will be discussed later in sec. 5.3.5 for the flow in Fig. 5.13.

One surprising result of this classification is that for Cases 1. and 2., the flow at the zero crossing of the velocity $v = 0$ can actually be treated as dynamic friction. Accordingly, not much changes for discriminating static and dynamic friction coefficients $\mu^{\mathrm{stat}} \neq \mu^{\mathrm{dyn}}$,

except the end points of the constraint manifold in Fig. 5.12 will be $\pm\mu^{\text{stat}}$ instead of $\pm\mu$. This is true both for the orthodox choice of $\mu^{\text{stat}} > \mu^{\text{dyn}}$ as well as for the experimental situation with $\mu^{\text{stat}} < \mu^{\text{dyn}}$ for various kinds of polymers[10].

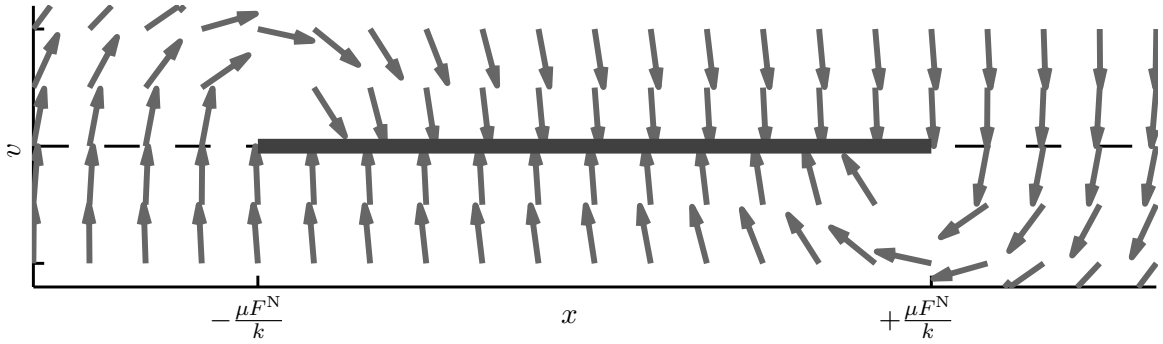

Fig. 5.12 Flow Φ in phasespace (directions only, arrows are unit vectors) for a linear oscillator with dry-friction with $m = 0.25$, $k = 1$ and $\mu = 0.2$ near to the $v = 0$-axis. The thick line is an accumulation of stable fix points.

5.3.3 Determination of the static friction force

Equation (5.23) can be rewritten for the velocity in $\gamma\dot{x} = \gamma v$ with a case discrimination for $\pm\mu F^{\text{N}}$ as

$$v = \begin{cases} \dfrac{-m\ddot{x} - kx - \mu F^{\text{N}}}{\gamma}\,, v > 0, \\ \dfrac{-m\ddot{x} - kx + \mu F^{\text{N}}}{\gamma}\,, v < 0. \end{cases} \tag{5.27}$$

For static friction at $v = 0$, there is no velocity dependence left in eq. (5.27), and therefore the computation of the numerical value for static friction will not be based on the velocity at all. Velocity dependent forces in models like Stribeck-friction from section 2.8 would also not be included in the computation of the static friction. Next, what is called an indicator function in Hairer et al.[51] is defined as

$$g(x, \dot{x}) = g(x, v) = v, \tag{5.28}$$

without actual dependence of x. This v refers to the whole velocity field in the phase space Fig. 5.12, not to the velocity $v(t)$ of a single trajectory in phasespace: This indicator function v will become the constraint function for $v = 0$ and $a_I < 0$, $a_{II} < 0$. When approaching v, forces in region I, resp. II are

$$f_I = -kx - \mu F^{\text{N}} \quad \text{for} \quad v > 0, \tag{5.29}$$

$$f_{II} = -kx + \mu F^{\text{N}} \quad \text{for} \quad v < 0. \tag{5.30}$$

The auxiliary quantities from eq. (5.25,5.26) become

$$a_I = +\frac{f_I}{m} \text{ in region I }, \; v > 0, \tag{5.31}$$

$$a_{II} = -\frac{f_{II}}{m} \text{ in region II}, \; v > 0, \tag{5.32}$$

The Filippov-solution looks for the solution for $v = 0$ in the "convex hull" of f_I, f_{II}, namely

$$f(\dot{x}, \lambda) = (1 - \lambda) f_I + \lambda f_{II}, \tag{5.33}$$

where the Lagrange parameter λ must still be determined. For $v = 0$, according to Newton's equation of motion, there is

$$\ddot{x} = \frac{f(\dot{x}, \lambda)}{m}, \tag{5.34}$$

while the indicator function eq. (5.28),

$$0 = g(x, \dot{x}) = v \tag{5.35}$$

for $v = 0$, $a_I < 0$, $a_{II} < 0$, morphs into the constraint function, therefore the suggestive abbreviation with $g(\dots)$. As in the case of the pendulum from eq. (5.3) to eq. (5.4), an "additional" equation is produced by time derivation of the constraint function $g(x, v) = v = \dot{x}$ (not the individual time derivative $v(t)$), which must also be zero,

$$0 = \frac{\mathrm{d}}{\mathrm{d}t} g(x, \dot{x}) = \frac{\mathrm{d}}{\mathrm{d}t} \dot{x} = 0. \tag{5.36}$$

One can replace $\ddot{x}$ from eq. (5.34) and obtain

$$\frac{f(\dot{x}, \lambda)}{m} = 0. \tag{5.37}$$

This means that λ can be computed via

$$f(\dot{x}, \lambda) = (1 - \lambda) f_I + \lambda f_{II} = 0 \tag{5.38}$$

from the forces as

$$\lambda = \frac{f_I}{f_I - f_{II}}. \tag{5.39}$$

By inserting the explicit expression for f_I and f_{II}, one obtains a λ so that the spring force $-kx$ is compensated exactly. Alternatively, the Lagrange multiplier can be expressed by the auxiliary variables from eq. (5.31,5.32) as

$$\lambda = \frac{a_I}{a_I + a_{II}}. \tag{5.40}$$

In the following, this approach will be called DAE-friction. Recently, D. Wolf characterized the friction law in contact dynamics in sec. 2.3 by: "Prof. Radjai has this strange friction law which depends on the acceleration, not on the velocity."[114] From our perspective, there is nothing strange about it, the acceleration-based friction is a direct outcome of the time derivative of the velocity constraint in eq. (5.36). It is more amazing that, while static friction is so non-linear that it is actually multi-valued, the correct value can by obtained from a simple scalar equation eq. (5.39) or eq. (5.40). On another side note, while the Cundall-Strack model in sec. 2.2 uses the time integral over the sliding velocities, the DAE-friction uses the differential.

5.3.4 Implementation with adaptive step size

Hairer and Wanner[51] have implemented the algorithm with adaptive step size. At the end of every time step $t_n+\tau$, they compute the dense output, the Taylor expansion for $x(t)$ and $v(t)$ between t_n and $t_n+\tau$. If a zero crossing t_0 is detected in $t_n < t_0 < t_n+\tau$, they rewind the solution back to t_0, determine which one of the Cases 1 to 4 in sec. 5.3.2 is applicable and use the formalism from sec. 5.3.3. Then they restart the simulation at t_0. While this approach is the method of choice in the case of few degrees of freedom, it is is inconvenient for multibody simulations with many thousand particles: The time integration for all particles would have to be stopped and restarted for all particles whenever there is a zero crossing of a single particle, see [51], Fig. 6.4. This would fragment the effective timestep, which would decrease with the number of particles as in the case of the inelastic collapse for rigid collisional particles[115]. Therefore, for many body simulations, a formalism with constant timestep is preferable which we will outline in sec. 5.4.

5.3.5 Painlevé-paradox

In the linear frictional oscillator in eq. (5.23), the phase flow at $v = 0$ for $k|x| < \mu|F^{\mathrm{N}}|$ is obviously the only physical meaningful choice , and the formalism for λ will produce the appropriate value for the static friction which in general will be smaller than the modulus of the dynamic friction $\mu|F^{\mathrm{N}}|$. On the other hand, if the system is started at $t = 0$ on $v = 0$, it is easy to get things wrong: Suppose we use $\pm\mu|F^{\mathrm{N}}|$ as initial friction value instead of one of the smaller static friction values which compensate the external forces. In case 4. of sec. 5.3.2, the external (elastic and damping) forces are overcompensated by the friction force and the mass is accelerated in the direction of the friction force. This acceleration due to the friction force is a contradiction to friction as a force which inhibits motion. The corresponding phase flow in Fig. 5.13 shows that the flow is pulled away from the constraint manifold due to the ad-hoc choice of sign ± 1. In the language of DAEs, this is a case of inconsistent initial conditions from sec. 5.1.5. The analysis is simple for the frictional oscillator, but not for more bodies or degrees of freedom: Erroneously implied dynamic friction leads to conflicting direction for friction forces and velocities which are

referred to as "Painlevé paradox", going back to an article by Painlevé[116] based in turn on an article by Jellet[117]. Because the assumptions $v > 0$ and $v < 0$ lead to contradictions, some authors [118] concluded erroneously that dry friction "is in contradiction to classical mechanics" or "classical mechanics is incomplete". (The conclusion is sometimes narrowed to "rigid" bodies, but in the frictional oscillator, the normal force F^{N} is rigid, without any oscillatory variation.) While for logical propositions, the principle of "tertium non datur" holds propositions and their opposites, the cases $v > 0$ and $v < 0$ are not exhaustive: That third possibility, $v = 0$ with static friction, has been overlooked. The situation is particularly inscrutable in the case of multi-body mechanisms with forces acting in different directions[119]. For such "Painlevé paradoxes", the solutions with "consistent initial conditions" would be solutions with static friction. In some cases, these solutions might even be multivalued for statically indeterminate problems, where the static friction force can be distributed between several contacts. Well before the times of differential inclusions, Hamel[120] concluded that for the case of solid friction, "one had to give up the assumption that every initial condition is realizable." Denoted as "inconsistent initial conditions", this is nowadays a common notion in the field of DAEs. The problems arising in linear complementary problems[121, 122] are a result of requiring two mathematically simultaneous solutions for a mechanical sequential problem where, based on the normal forces, the tangential forces follow as reactions.

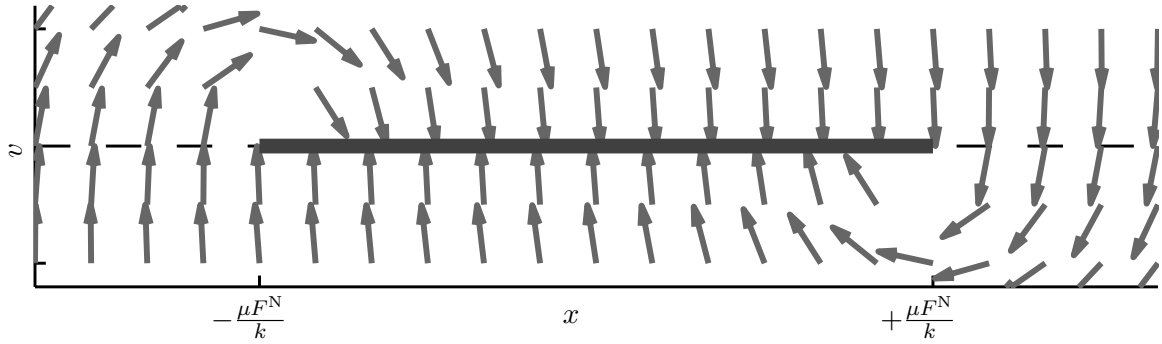

Fig. 5.13 Flow Φ in phase space (directions only, arrows are unit vectors) for inconsistent initial values at $v = 0$ which are typical for Painlevé-paradoxes: A body with $v = 0$ is unphysically pulled either into the region $v > 0$ or $v < 0$ for a friction value $\pm\mu|F^{\mathrm{N}}|$, away from the constraint manifold (thick line between $-\frac{\mu|F^{\mathrm{N}}|}{k}$ to $+\frac{\mu|F^{\mathrm{N}}|}{k}$ at $v = 0$). This type of flow is not a possible flow for ODEs with non-smooth right hand sides in the sense of Filippov[2].

5.4 Implementation with constant timestep

The approach by Hairer and Wanner[51] is "numerically exact" for the use with adaptive timestep. For use with a constant timestep τ, several adaptations were required. Such an approach is preferable for granular systems, as the elasticity Y and minimum particle mass $m_{\min}$ in the system determine a minimal possible timestep anyway:

$$\tau_{\min} = \frac{1}{10}\pi\sqrt{\frac{m_{\min}}{Y}}. \tag{5.41}$$

Stop-and-restart procedures with adaptive integrators would seriously reduce the efficiency of the algorithm, as the effective timestep (from the zero-crossing of one contact to the zero crossing of another contact) would decay fast with the particle size, see Fig. 5.14. On the other hand, adaptive timesteps with stops and restarts circumvent problems which are introduced by keeping the timestep τ constant: A zero crossing of the velocity occurs rarely ever precisely at a timestep t or the next $t + \tau$, but in between. Another issue is that when we are not directly on a zero crossing, we have to deal with a spurious, residual finite velocity.

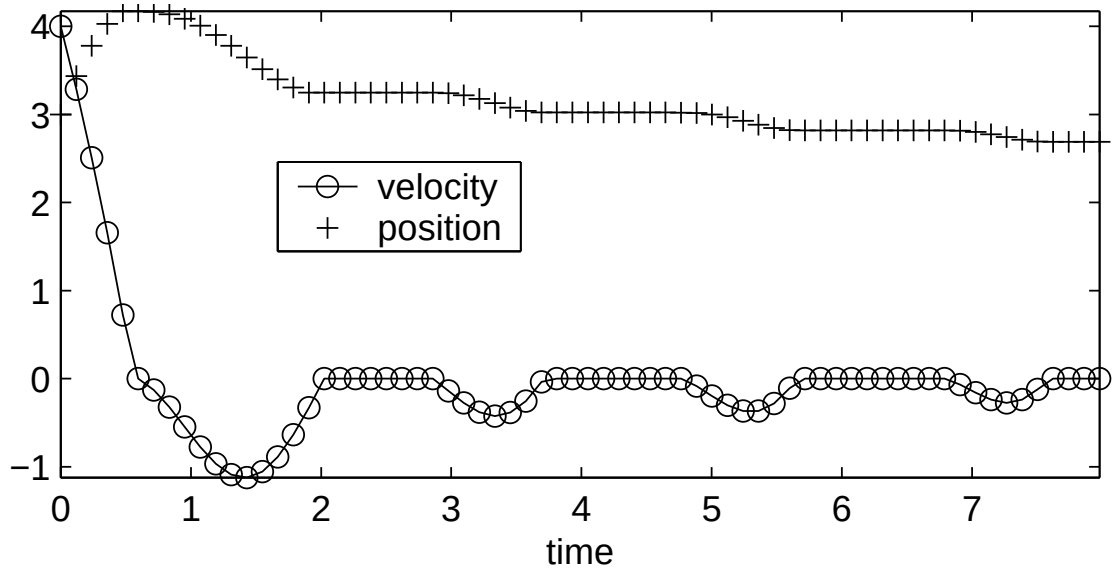

Fig. 5.14 Implementation of the friction formalism with constant timestep results in a decrease of the timestep near the zero-velocity transition. Stop- and restart procedures for the friction evaluation at every zero-crossing of the velocity lead to a fragmentation of the effective timestep. An implementation with constant timestep is therefore preferred.

5.4.1 Theoretical and actual loss of precision

When the friction condition from sec. 5.3.2 is not evaluated on the zero crossing but at the nearest timestep, we formally loose some precision, due to a modified time sequence of static and dynamic friction, see Fig. 5.15. (Stability will not be affected, as the accumulation of stable fix points in Fig. 5.12 should still attract the flow over a time-span $\leq \tau$.) This loss of precision is nevertheless ephemeral: The formal numerical precision of the trajectory computation (often three to four digits) as a rule exceeds the actual predictive accuracy for the experiment, because of the limited validity (one or two digits) of the underlying tabulated friction coefficients. Moreover, for many particle problems with strong non-linearities, there are no "quasi exact" reference solutions anyway. The frictional oscillator from Hairer et al.[51] computed with adaptive timesteps can also be obtained with constant timesteps[16]: The errors in the trajectory and velocity are smaller than the formal "error of up to 1 timestep τ" suggests. From the physical point of view, also for many body systems the error will be negligible and using a constant instead of adaptive timesteps will not have any significant effect on the accuracy.

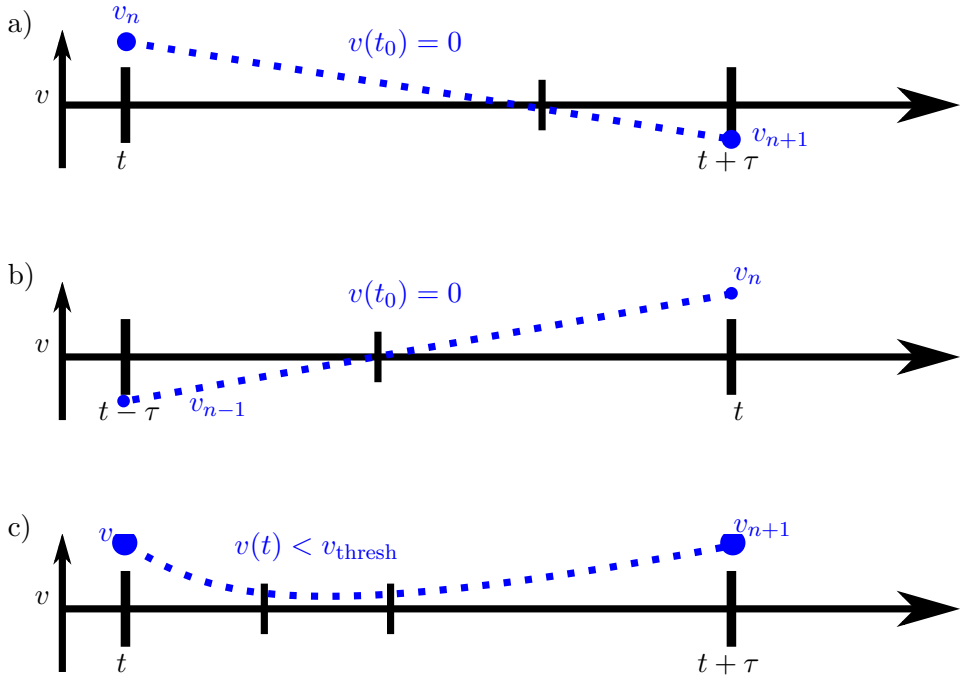

Fig. 5.15 Zero crossings of the velocity usually occur between two successive timesteps but rather inbetween a)-b), resulting in spurious finite velocities. In the current timestep, the velocity can also become vanishingly small without a zero-crossing c), likewise leading to non-zero residual velocities.

5.4.2 Threshold for vanishing velocity

For a finite-difference approximation of the time evolution, the velocities are practically never exactly zero due to rounding and discretisation errors: An n-th order integrator with accuracy $O(\tau^n)$ means that the numerical error (i.e. the noise) is $\epsilon(\tau^{n+1})$. As a

hand-waving example: When most parameters (masses etc.) are close to unity, with a timestep of $\tau = 0.1$ and a second order integrator, the error would be $\propto 0.1^3 = 0.001$. Accordingly, the algorithm must be prepared to deal with "numerically zero" velocities which are actually of the order of 0.001. The velocity may, even without zero crossings, be low enough so that the condition for static friction may be valid. Therefore, a threshold accuracy v^{thresh} for "numerically zero" has to be defined and, if the velocity is below the threshold accuracy v^{thresh}, it must be verified which of the cases 1 to 4 from sec. 5.3.2 applies. This threshold will depend on the problem (particle size, Young modulus) and the magnitude of the timestep τ. The velocity threshold for "numerically zero" velocity is given by the length scale Δx which a timestep of length τ can not resolve any more (due to modelling or accuracy issues) so that

$$v^{\text{thresh}} = \frac{\Delta x}{\tau}. \tag{5.42}$$

5.4.3 Zero crossing of the velocity in the next timestep

To determine whether there is a sign change in the velocity $v(t)$ from the current timestep t to $v(t+\tau)$ in the next timestep, we determine whether there is a zero crossing via

$$v(t) \cdot v(t+\tau) < 0. \tag{5.43}$$

Because the evaluation is still at t, estimators for $v(t+\tau)$ are required, where the obvious choice is

$$v_1^{\text{est}}(t+\tau) = v(t) + \tau a(t) \tag{5.44}$$

under the assumption that the acceleration does not change. (It is possible to specify an additional prefactor in front of $a(t)$ to take care of a possible variation of the acceleration, but instead this approach will verify whether there was a zero crossing in the previous timestep, which is explained in the next section.) More important than the influence of a variation of the external forces on the accumulated $a(t)$ will be a variation of the friction $\pm\mu|F_N|$ due to the sign change in the velocity $v(t)$. Accordingly, additionally the two other estimators should be taken into account,

$$v_2^{\text{est}}(t+\tau) = v(t) + \tau\left(a(t) - \mu|F^{\text{N}}|\right), \tag{5.45}$$

$$v_3^{\text{est}}(t+\tau) = v(t) + \tau\left(a(t) + \mu|F^{\text{N}}|\right). \tag{5.46}$$

Accordingly, in the simulation, if one of the three conditions

$$v(t) \cdot v_i^{\text{est}}(t+\tau) < 0,\ i = 1, \ldots, 3. \tag{5.47}$$

indicates a sign change in the velocity, it must be verified which of the cases 1 to 4 from sec. 5.3.2 applies. It turned out that the three conditions in eq. (5.44-5.46) were rather

independent, so none of them can be omitted. The case of a double reversal of the sign in the velocity within a single timestep ($\pm \to \mp \to \pm$) must not be treated explicitly: Such occurrences will either be spurious, or, if they are physical, they will be detected by the velocity threshold v_{thresh} from sec. 5.4.2.

5.4.4 Zero crossing of the velocity from the previous timestep

Strong force variations or oscillations at short wavelengths in packings with high coordination number may render the predictions in sec. 5.4.3 unreliable. Therefore, at time t, one should also investigate whether the previous timestep $t - \tau$ contained an unpredicted zero crossing. Accordingly, we have to verify

$$v(t) \cdot v(t - \tau) < 0. \tag{5.48}$$

Storing all contact velocities (including sliding and rolling) will be rather inefficient, so estimators will again be used, in analogy to the previous section

$$\begin{aligned} v_1^{\text{est}}(t - \tau) &= v(t) + \tau a(t), & (5.49)\\ v_2^{\text{est}}(t - \tau) &= v(t) + \tau \left(a(t) - \mu |F^{\text{N}}|\right), & (5.50)\\ v_3^{\text{est}}(t - \tau) &= v(t) + \tau \left(a(t) + \mu |F^{\text{N}}|\right). & (5.51) \end{aligned}$$

If one of the three conditions

$$v(t) \cdot v_i^{\text{est}}(t - \tau) < 0, \ i = 1, \ldots, 3. \tag{5.52}$$

is fulfilled, it must be verified which of the cases 1 to 4 from sec. 5.3.2 applies.

5.4.5 Dealing with residual velocities

The condition for static friction implies that the velocity vanishes, which is exactly implemented for adaptive stepsize integration with stopping and restarting[51] at the zero-crossings. For constant timesteps, we will only be close to zero, with small but finite residual velocities which will not be compensated by the static friction force computed under the assumption of zero velocity. In that case, we have to specify an additional "break" deceleration which reduces these residual velocities to zero. For a body with the kinetic energy

$$T(t) = \frac{1}{2} m v(t)^2, \tag{5.53}$$

there is a deceleration a which includes static friction anyway, so the work of an additional a^{break} will be required to reduce the velocity to zero within the timestep τ. Accordingly,

the kinetic energy must be equal to the work

$$\begin{aligned} \frac{1}{2}mv(t)^2 &= \frac{1}{2}m\Big(a + a^{\text{break}}\Big)\Delta x\tau \\ &= \frac{1}{2}m\Big(a + a^{\text{break}}\Big)v(t)\tau, \end{aligned} \tag{5.54}$$

so the deceleration

$$a^{\text{break}} = \left(\frac{v(t)}{\tau} - a(t)\right), \tag{5.55}$$

will reduce the kinetic energy to zero. This acceleration (or the corresponding force) is velocity dependent and may therefore not be included in eqs. (5.29,5.30) for the computation of λ, see the remarks following eq. (5.27). While the analytic situation is clear, the numerical simulation is slightly more complicated: The finite-difference approximation of the acceleration $a(t)$ and velocity $v(t)$ in the time integrator has discretisation errors, so the use of the breaking deceleration from eq. (5.55) reduces the velocity not to zero, but to a value of the error order of the time integrator. Also, the energy conservation in eq. (5.54) is violated for all integrators which are not "symplectic". These discretisation errors may result in a residual velocity $v(t+\tau) \neq 0$. For a force equilibrium where the sliding velocity yields the same $\tilde{v}(t)$ over several timesteps due to the error of the time integrator,

$$a^{\text{break,num}} = -\left(2\frac{\tilde{v}(t)}{\tau} - a(t)\right) \tag{5.56}$$

will reduce the sliding velocities below $\tilde{v}(t)$. The relative merits of a^{break} and $a^{\text{break,num}}$ will be investigated later in sec. 7.2.

5.5 Limitation of the uniqueness of the numerical solution

While the analytic solution for zero contact velocity is unique, the numerical solution allows some variation in the treatment. This is due to the generic effect of any numerical approach, not due to an arbitrariness: Deviations from the exact values must be treated in an appropriate way, and the treatment due to numerical errors allows some liberties with respect to priorities (determination of relative position more important than precise determination of the time of stick) and the intended result (stable many particle simulation, not high precision for the single particle contact). It should not be forgotten, that the Newtonian kinematics itself ($a = \dot{v} = \ddot{x}$, $v = \dot{x}$) in a numerical simulation has been replaced by a finite element approximation. This is also the reason, why the choice of integrators influences the numerical result: Obtaining precise equilibrium positions and elimination of noise are, for problems with static friction, more important than an ephemeral, pseudo-accurate computation of trajectories.

Chapter 6

Generalisation to many particle systems

Mechanics curricular start with statics and proceed to dynamics, so the statics part of mechanics looks simpler than the dynamics part. The real reason for the simplicity is that Newton's equation of motion is not needed. In contrast, the numerical realisation of a static configuration in a dynamic simulation is a significant challenge: A "numerically exact" force equilibrium is needed so that the particles come to rest relative to each other, which is unaffected by the noise introduced by the finite difference approximation of the kinematics. In the presence of too much numerical noise, there will always be a residual relative motion. Additionally, the common notion of an absolute coordinate system in the mathematical theory of dynamical systems must be abandoned and a formulation must be found for arbitrary frames of reference. (Granular materials in a mixing drum are not even described by an inertial system, but by a rotating coordinate frame.) Fixing particles in tangential direction relative to each other based on the information from the contact matrix (i.e. the matrix of the direction of tangential contacts) can fix the particles in "perfect static frictional contact", i.e. no tangential sliding[123]. On the other hand, such a formalism cannot guarantee the boundedness of the tangential forces by $\pm\mu F^{\mathrm{N}}$, the effective computed tangential force may in fact become infinite.

For finite coefficients of friction, there are ambiguities in the construction of the convex hull which lead to the problems discussed in sec. 2.4 for the algorithm proposed by Stewart.

6.1 Effective single particle problem

Instead of a (probably futile) attempt with a contact matrix for many-body systems as in Fig. 6.1, we propose that the formalism from secs. 5.3 and 5.4 is applied on the contact level: Instead of using the velocities at the centre of mass in the fixed coordinate system, the relative tangential velocities and accelerations for the reduced mass are used at the

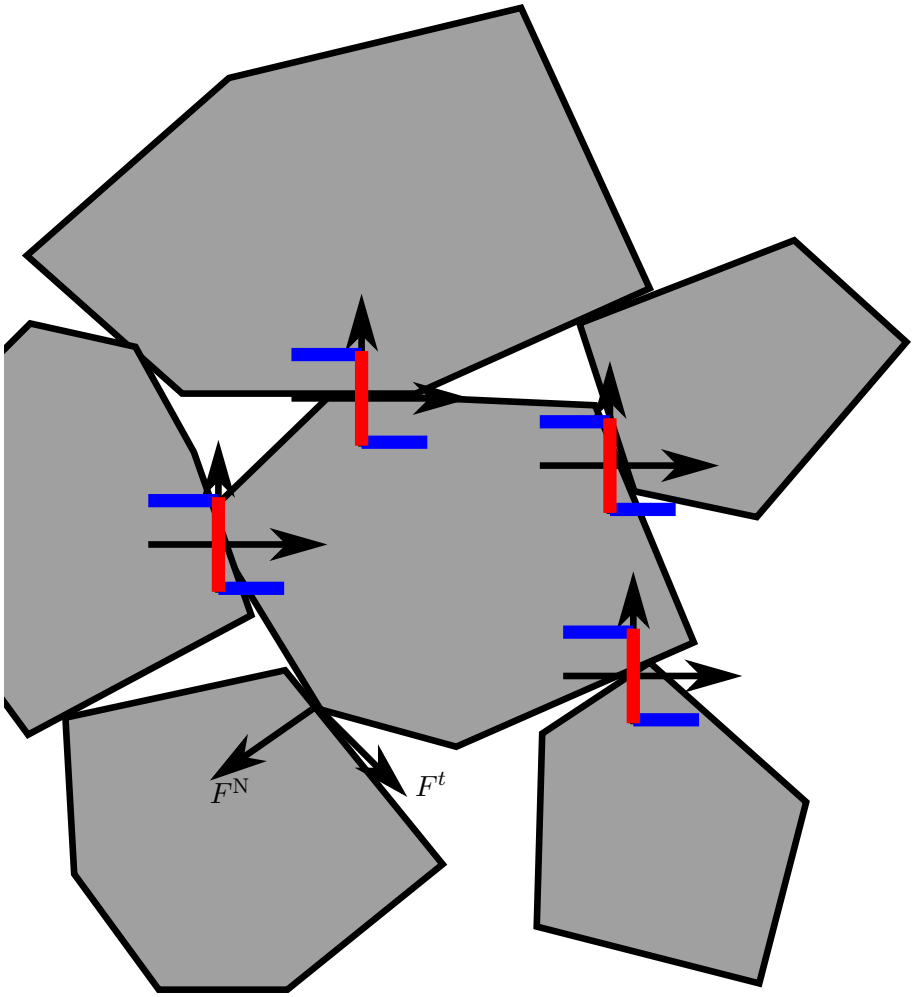

Fig. 6.1 For many-body contacts, building up the contact matrix and a related "friction space" for each particle as a simplex of frictional constraints in a combinatorial approach to static friction is not feasible: The same constraints allow multiple solutions, the dimension of the solution space increases in combinatorial order.

contact point. The velocities and accelerations are computed according to eqs. (4.8)-(4.9) and projected onto the tangential direction,

$$\boldsymbol{v}_{\mathrm{rel}}^{\tan} = ((\boldsymbol{v}_a - \boldsymbol{v}_b)\boldsymbol{t}) \cdot \boldsymbol{t}, \tag{6.1}$$

$$\boldsymbol{a}_{\mathrm{rel}}^{\tan} = ((\boldsymbol{a}_a - \boldsymbol{a}_b)\boldsymbol{t}) \cdot \boldsymbol{t}. \tag{6.2}$$

The "correct" reduced mass for the tangential motion is not the one solely based on the "rectilinear masses" m_a and m_b in eq. (4.13) for central forces, because the inertia I_a and I_b is neglected. Instead, the computation should be based on the reduced tangential mass[124]

$$\frac{1}{m_{\mathrm{eff}}^{\tan}} = \frac{1}{m_a} + \frac{r_a^2}{I_a} + \frac{1}{m_b} + \frac{r_b^2}{I_b}. \tag{6.3}$$

which also takes into account the contact vectors r_a and r_b between the centres of mass and the contact point. The reduced tangential mass can be derived for a cylinder rolling down a slope without slip, where the Coulomb friction is smaller than for a block in pure sliding motion[16], see Fig. 6.2. For a given force, the (pedantically speaking, physically invalid) use of the (normal) reduced mass m_{red} will lead to a smaller deceleration and therefore a delayed action of the dynamic friction compared to the use of $m_{\mathrm{eff}}^{\mathrm{tan}}$. For particles at relative rest, static friction will not be affected by the use of the "wrong" (tangential instead of conventional) reduced mass, because the mass is dropped in the derivation of λ from eq. (5.39) to eq. (5.40). Unique solutions at multiple contact points of a single particle can be obtained even for statically indeterminate situations, because the static friction is determined from the dynamical system.

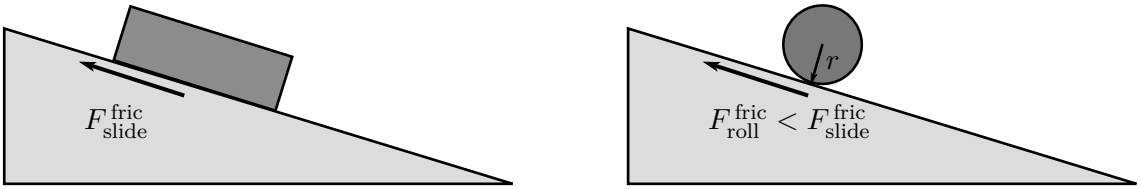

Fig. 6.2 For a block sliding down a slope, the friction force is the opposite of the downhill force. For a cylinder rolling down a slope, the tangential acceleration is coupled with an angular acceleration. The friction force required to bring the cylinder to a stop is lower than for pure sliding. This is expressed in an additional corrective term in the reduced mass.

6.1.1 Discrimination between dynamic and static friction

As for the frictional oscillator, the determination whether the contacts are in sliding or in static friction must precede the actual computation of the friction value. The influence of other contacts is formally absorbed as external force, which affects the normal force at the contact under consideration, so the formalism can proceed in analogy to the single particle case. We can separate the force equation when approaching $v_{\mathrm{rel}}^{\mathrm{tan}} = 0$ as

$$f_I = m_{\mathrm{eff}}^{\mathrm{tan}} a_{\mathrm{rel}}^{\mathrm{tan}} - \mu |F^{\mathrm{N}}| \quad \text{for} \quad v_{\mathrm{rel}}^{\mathrm{tan}} > 0, \tag{6.4}$$

$$f_{II} = m_{\mathrm{eff}}^{\mathrm{tan}} a_{\mathrm{rel}}^{\mathrm{tan}} + \mu |F^{\mathrm{N}}| \quad \text{for} \quad v_{\mathrm{rel}}^{\mathrm{tan}} < 0. \tag{6.5}$$

This allows to define the auxiliary quantities from equations (5.31) and (5.32) for the direction of the flow as

$$a_I = a_{\mathrm{rel}}^{\mathrm{tan}}(x, v) - \tfrac{\mu |F^{\mathrm{N}}|}{m_{\mathrm{eff}}^{\mathrm{tan}}}, \tag{6.6}$$

$$a_{II} = -a_{\mathrm{rel}}^{\mathrm{tan}}(x, v) - \tfrac{\mu |F^{\mathrm{N}}|}{m_{\mathrm{eff}}^{\mathrm{tan}}}. \tag{6.7}$$

As with the single contact case, we have now the same four scenarios:

Case 1. $a_I > 0; a_{II} < 0$: The flow crosses $v_{\text{rel}}^{\text{tan}} = 0$ from $v_{\text{rel}}^{\text{tan}} < 0$ to $v_{\text{rel}}^{\text{tan}} > 0$, the friction is dynamic with a jump from $+\mu F^{\text{N}}$ to $-\mu F^{\text{N}}$

Case 2. $a_I < 0; a_{II} > 0$: The flow crosses $v_{\text{rel}}^{\text{tan}} = 0$ from $v_{\text{rel}}^{\text{tan}} > 0$ to $v_{\text{rel}}^{\text{tan}} < 0$, the friction is dynamic, with a jump from $-\mu F^{N}$ to $+\mu F^{\text{N}}$.

Case 3. $a_I < 0; a_{II} < 0$: The flow is pulled into $v_{\text{rel}}^{\text{tan}} = 0$, we have static friction with a value that will rarely be f_I or f_{II}, but a value in between, to be computed in the convex hull of f_I and f_{II}.

Case 4. $a_I > 0; a_{II} > 0$: The flow would be non-unique along $v_{\text{rel}}^{\text{tan}} = 0$ and would pull away from $v_{\text{rel}}^{\text{tan}} = 0$ in opposite directions (Painlevé-paradox).

6.1.2 Determination of the static friction force

In analogy to the single particle case, eq. (5.33), for case 4 we compute the value for static friction for a single contact in the convex hull of f_I and f_{II},

$$f(v_{\text{rel}}^{\text{tan}} = 0, \lambda) = (1 - \lambda) f_I + \lambda f_{II}, \tag{6.8}$$

where the Lagrange parameter λ can be determined via eq. (5.40) as

$$\begin{aligned}
\lambda &= \frac{a_I}{a_I + a_{II}} && (6.9)\\
&= \frac{a_{\text{rel}}^{\text{tan}}(t) - \mu |F^{\text{N}}|/m_{\text{eff}}^{\text{tan}}}{a_{\text{rel}}^{\text{tan}}(t) - \mu |F^{\text{N}}|/m_{\text{eff}}^{\text{tan}} - a_{\text{rel}}^{\text{tan}}(t) - \mu |F^{\text{N}}|/m_{\text{eff}}^{\text{tan}}} && (6.10)\\
&= \frac{a_{\text{rel}}^{\text{tan}}(t) - \mu |F^{\text{N}}|/m_{\text{eff}}^{\text{tan}}}{-2\mu |F^{\text{N}}|/m_{\text{eff}}^{\text{tan}}} && (6.11)\\
&= \frac{1}{2} - \frac{m_{\text{eff}}^{\text{tan}} a_{\text{rel}}^{\text{tan}}(t)}{2\mu |F^{\text{N}}|}. && (6.12)
\end{aligned}$$

The last form, eq. (6.11) shows that for static friction, λ has to be between 0 and 1, else the relative acceleration exceeds the friction force, so that the contacts can not exhibit static friction. Again, just as in the single particle case, the static friction will depend on the relative accelerations, not on the relative velocities.

6.2 Invariance under index change

When the particle indices are exchanged in the DEM-computation, the positions are exchanged and the relative velocities and accelerations change sign. The friction computation must be invariant under such an index change, i.e. the static friction force must compensate for the reverse relative acceleration. To be on the save side, we compute this case

explicitly. For the relative velocities and accelerations, one obtains

$$v_{ba} = -v_{\text{rel}}^{\tan} = -v_{ab}, \tag{6.13}$$
$$a_{ba} = -a_{\text{rel}}^{\tan} = -a_{ab}. \tag{6.14}$$

On the constraint manifold at $v_{\text{rel}}^{\tan} = 0$, the equation for the tangential forces is separated into

$$f_{I,ba} = a_{ba} m_{\text{eff}}^{\tan} - \mu |F^{\text{N}}|, \tag{6.15}$$
$$f_{II,ba} = a_{ba} m_{\text{eff}}^{\tan} + \mu |F^{\text{N}}|. \tag{6.16}$$

Inserting the values for v_{ba} and a_{ba}, these equations can be rewritten as

$$f_{I,ba} = -a_{\text{rel}}^{\tan} m_{\text{eff}}^{\tan} - \mu |F^{\text{N}}| = -f_{II,ab}, \tag{6.17}$$
$$f_{II,ba} = -a_{\text{rel}}^{\tan} m_{\text{eff}}^{\tan} + \mu |F^{\text{N}}| = -f_{I,ab}. \tag{6.18}$$

Accordingly, for the auxiliary variables a_I, a_{II} from eqs. (5.25)-(5.26),

$$a_{I,ba} = a_{ba} - \frac{\mu |F^{\text{N}}|}{m_{\text{eff}}^{\tan}} = -a_{\text{rel}}^{\tan} - \frac{\mu |F^{\text{N}}|}{m_{\text{eff}}^{\tan}} = a_{II,ab}, \tag{6.19}$$
$$a_{II,ba} = -a_{ba} - \frac{\mu |F^{\text{N}}|}{m_{\text{eff}}^{\tan}} = a_{\text{rel}}^{\tan} - \frac{\mu |F^{\text{N}}|}{m_{\text{eff}}^{\tan}} = a_{I,ab}, \tag{6.20}$$

i.e. the indices are reversed. Compared to $\lambda = \lambda_{ab}$, for λ_{ba} it follows that

$$\lambda_{ba} = \frac{a_{I,ba}}{a_{I,ba} + a_{II,ba}} \tag{6.21}$$
$$= \frac{a_{II,ab}}{a_{I,ba} + a_{II,ba}} \tag{6.22}$$
$$= \frac{-a_{\text{rel}}^{\tan} - \mu |F^{\text{N}}| / m_{\text{eff}}^{\tan}}{-a_{\text{rel}}^{\tan} - \mu |F^{\text{N}}| / m_{\text{eff}}^{\tan} + a_{\text{rel}}^{\tan} - \mu |F^{\text{N}}| / m_{\text{eff}}^{\tan}} \tag{6.23}$$
$$= \frac{-a_{\text{rel}}^{\tan} - \mu |F^{\text{N}}| / m_{\text{eff}}^{\tan}}{-2\mu |F^{\text{N}}| / m_{\text{eff}}^{\tan}} \tag{6.24}$$
$$= \frac{1}{2} + \frac{m_{\text{eff}}^{\tan} a_{\text{rel}}^{\tan}(t)}{2\mu |F^{\text{N}}|} \tag{6.25}$$
$$= 1 - \lambda_{ab}. \tag{6.26}$$

Likewise

$$(1 - \lambda_{ba}) = 1 - \left(\frac{1}{2} + \frac{m_{\text{eff}}^{\tan} a_{\text{rel}}^{\tan}(t)}{2\mu |F^{\text{N}}|} \right) \tag{6.27}$$
$$= \frac{1}{2} - \frac{m_{\text{eff}}^{\tan} a_{\text{rel}}^{\tan}(t)}{2\mu |F^{\text{N}}|} \tag{6.28}$$
$$= \lambda_{ab}. \tag{6.29}$$

So, for the convex hull it follows, that

$$\begin{aligned} f_{ba}(v_{\text{rel}}^{\tan}=0,\lambda_{ba}) &= (1-\lambda_{ba})f_{I,ba}+\lambda_{ba}f_{II,ba} && (6.30)\\ &= -(1-(1-\lambda_{ab}))f_{II,ab}-(1-\lambda_{ab})f_{I,ab} && (6.31)\\ &= -[(1-\lambda_{ab})f_{I,ab}+\lambda_{ab}f_{II,ab}] && (6.32)\\ &= -f_{ab}(v_{\text{rel}}^{\tan}=0,\lambda_{ab}), && (6.33) \end{aligned}$$

i.e. the sign of convex hull changes. Therefore the friction force changes sign when the indices are exchanged, because the direction of the static friction force is defined with respect to $v_{\text{rel}}^{\tan}$, not with respect to $\boldsymbol{n}$ and $\boldsymbol{t}$ as the elastic force. In conclusion, at the constraint manifold, the selection of the coordinate system with respect to the collision pair does not matter. The friction force will be the same for any choice of particle indices.

6.3 Concluding remarks

The derivation has shown, that by virtue of the introduction of the tangential relative acceleration, even in the many-body many-contact problem, each individual contact can be treated as one-dimensional, with its own local phase-space. Therefore, the solutions for the frictional forces are unique and well-defined, there is no problem with statically indeterminate contacts as in many truss-and-strut problems from engineering statics courses (which use only force equations), because the whole dynamics and the constraint equations for relative velocity and acceleration, as well as the contact history (the flow path Φ in the dynamical system) supplies additional information.

For this formalism, except for single particle problems, there can be no mathematical convergence proof: A mechanical system is stabilized in a static configuration as long as the magnitude of the static friction exceeds that of the external noise sources. In the same way, a stable solid can be simulated with pairwise interactions, e.g. Lennard-Jones potentials, even in the presence of thermal vibrations. In frictional systems, there are - even on the experimental level - influences from mechanical vibrations which lead to fretting and creep[10, 125] for single particles or the disintegration of the whole assembly. For the simulation, we have to ascertain by numerical experiment that the numerical noise is small enough so that relative velocities are negligible: This is the purpose of the following chapter 7.

6.4 Extension of the friction formalism to three dimensions

The friction formalism presented in this and the previous chapter is two-dimensional. An extension to three dimensions is straight forward: The formalism itself is quasi one-dimensional, oriented along the tangential relative acceleration. It is independent of the problem dimensionality and the overlap computation. As long as the tangential component of the relative acceleration between two bodies can be defined, we can extend our friction formalism to three dimensions without modification. When a contact normal is given, this defines the two-dimensional contact plane, so that the projection of the (in the most general case) three-dimensional relative acceleration vector into that plane yields a one-dimensional problem in the contact plane $\mathcal{T}$, see section 4.4.2. In two dimensions, the tangential velocity and tangential acceleration are always parallel to each other, and therefore both static and dynamic friction forces are parallel,

$$(\boldsymbol{v}^{\mathrm{tan}} \parallel \boldsymbol{F}^{\mathrm{dyn}}) \parallel (\boldsymbol{a}^{\mathrm{tan}} \parallel \boldsymbol{F}^{\mathrm{stat}}). \tag{6.34}$$

In three dimensions the tangential velocity and the tangential acceleration are no longer necessarily parallel. As the dynamic friction force is acting in direction of the tangential velocity, and the static friction force is acting in the direction of the tangential acceleration, that means, the static and dynamic friction forces may act in different direction, i.e. in general,

$$(\boldsymbol{v}^{\mathrm{tan}} \parallel \boldsymbol{F}^{\mathrm{dyn}}) \nparallel (\boldsymbol{a}^{\mathrm{tan}} \parallel \boldsymbol{F}^{\mathrm{stat}}). \tag{6.35}$$

The moments of inertia are tensorial in three-dimensional problems, so the reduced mass becomes, eq. (6.3), becomes in three dimensions

$$\frac{1}{m_{\mathrm{eff}}^{\mathrm{tan,3D}}} = \frac{1}{m_a} + \boldsymbol{r}_a^{\top} \boldsymbol{I}_a^{-1} \boldsymbol{r}_a + \frac{1}{m_b} + \boldsymbol{r}_b^{\top} \boldsymbol{I}_b^{-1} \boldsymbol{r}_b. \tag{6.36}$$

The algorithm is applicable even for rigid body problems as long as the normal forces and friction coefficients are defined, as in the case of an ellipse moving in a plane, where the normal force is determined by the acceleration of the centre of mass relative to the plane-normal. A comparison between the relevant quantities in one-, two-, and three dimensions is presentend in table 6.1.

Table 6.1 Comparison between the variables for the friction formalism in one-, two-, and three dimensions.

1D	2D	3D
	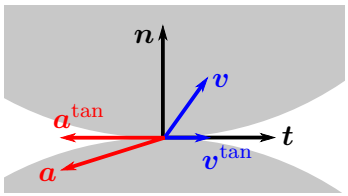	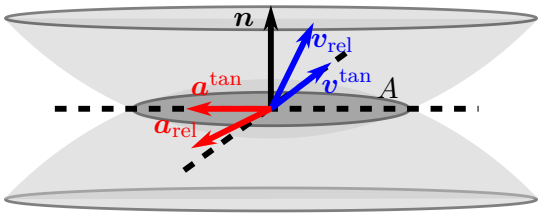
x	$\boldsymbol{x},\ \boldsymbol{n},\ \boldsymbol{t}$	$\boldsymbol{x},\ \boldsymbol{n},\ A$
v	$\boldsymbol{v}_{\text{rel}} \nearrow \boldsymbol{v}^{\text{N}}$, $\searrow \boldsymbol{v}^{\tan}$	$\boldsymbol{v}_{\text{rel}} \nearrow \boldsymbol{v}^{\text{N}}$, $\searrow \boldsymbol{v}^{\tan} = P(\boldsymbol{v}_{\text{rel}}\|A)$
a	$\vec{a}^{\text{rel}} \nearrow \boldsymbol{a}^{\text{N}}$, $\searrow \boldsymbol{a}^{\tan}$	$\vec{a}^{\text{rel}} \nearrow \boldsymbol{a}^{\text{N}}$, $\searrow \boldsymbol{a}^{\tan} = P(\boldsymbol{a}_{\text{rel}}\|A)$
m	$\dfrac{1}{m_{\text{eff}}^{\tan}} = \dfrac{1}{m_a} + \dfrac{1}{m_b} + \dfrac{\lvert\boldsymbol{r}_a\rvert^2}{I_a} + \dfrac{\lvert\boldsymbol{r}_b\rvert^2}{I_b}$	$\dfrac{1}{m_{\text{eff}}^{\tan}} = \dfrac{1}{m_a} + \boldsymbol{r}_a^{\top}\boldsymbol{I}_a^{-1}\boldsymbol{r}_a + \dfrac{1}{m_b} + \boldsymbol{r}_b^{\top}\boldsymbol{I}_b^{-1}\boldsymbol{r}_b$
scalars	$a_I = \boldsymbol{a}^{\tan} - \mu\lvert F^{\text{N}}\rvert/m$	$a_I = \lvert\boldsymbol{a}^{\tan}\rvert - \mu\lvert F^{\text{N}}\rvert/m$
$a_I,\ a_{II}$	$a_{II} = \boldsymbol{a}^{\tan} + \mu\lvert F^{\text{N}}\rvert/m$	$a_{II} = \lvert\boldsymbol{a}^{\tan}\rvert + \mu\lvert F^{\text{N}}\rvert/m$
F^{stat}	Vector $\boldsymbol{F}^{\text{stat}} \parallel \boldsymbol{t}$	Vector $\boldsymbol{F}^{\text{stat}} \parallel \boldsymbol{a}^{\tan}$
$x \parallel v \parallel a$	$(\boldsymbol{v}^{\tan} \parallel \boldsymbol{F}^{\text{dyn}}) \parallel (\boldsymbol{a}^{\tan} \parallel \boldsymbol{F}^{\text{stat}})$	$(\boldsymbol{v}^{\tan} \parallel \boldsymbol{F}^{\text{dyn}}) \nparallel (\boldsymbol{a}^{\tan} \parallel \boldsymbol{F}^{\text{stat}})$

Chapter 7

Validation of the friction law

In the following, the algorithm is applied to various problem geometries and the result compared with several different friction models. Further, the effect of the timestep and the effect of different time integrators are investigated. We use the parameters in table 7.1, if not mentioned otherwise. The density ρ with units [kg/m^2] and the Young's modulus Y with units [N/m] for polygons in two dimensions correspond to three-dimensional rod-like particles of the same cross-section with the same numerical values for the density ρ^{3D} with units [kg/m^3] and the Young's modulus Y^{3D} with units [N/m^2].

Table 7.1 Parameters for the interaction computation of 1m-long rod like particles.

Young's modulus Y	10^7[N/m]
Normal damping coefficient γ	0.5
Coefficient of friction μ (particle-particle, particle-wall)	0.6
Density of particles σ	5000[kg/m^2]

7.1 Computability and stability for granular systems

Granular materials are a paradigm of nonlinear (or chaotic) systems, in the sense discussed by e.g. Strogatz[126]. Collisions affect the trajectories two-fold, on the one hand by the non-linearity of the force for freely flying particles, as in Fig. 7.1. On the other hand, there is a cascade of direction changes when the packing density increases as in Fig. 7.2: When particles hit other particles, they either tilt or are deflected, to the left or right in two-dimensions, and towards a continuum of directions in three dimensions. This ordering of direction changes is a bifurcation cascade which advances with time, there is no nonlinearity parameter necessary as for the logistic map. In the field of granular materials, this has been termed "molecular chaos"[127] and has been the starting point for various theoretical investigations and used for the justification of simulations methods, approximations, etc.. This means, that most granular systems are intrinsically Lyapunov-

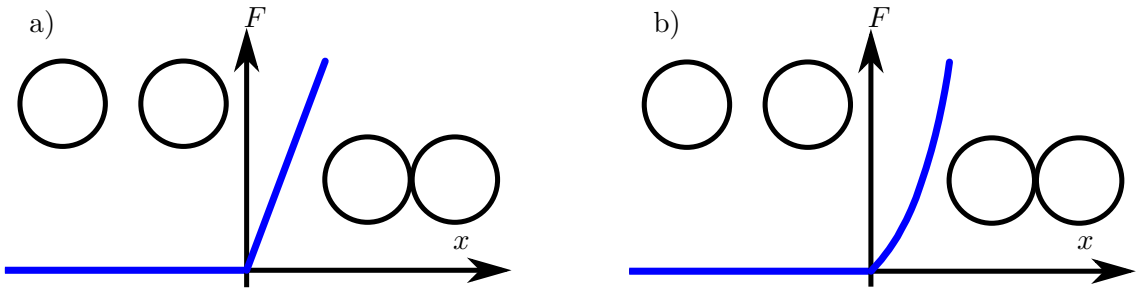

Fig. 7.1 Interaction forces for particles before the collision ($F = 0$ to the left of the vertical axis) and for the contacting particles ($F \propto x$ to the right of the vertical axis), for a "linear" force law in a) and a "non-linear" force law in b. The actual non-linearity which affects the particle trajectories during collisions is the variation from $F = 0$ to $F \propto x$ at $x = 0$.

unstable. A grave consequence is that individual trajectories of many-body systems cannot be predicted or verified, because infinitesimal changes change the whole outcome. On the other hand, such "ideally chaotic" trajectories in some cases make the averages of many-particle systems (densities, etc.) predictable. To demonstrate this effect we show the simulations of particles in a Galton board (Fig. 7.3). Round particles are dropped from a hopper into a triangular grid of pins and collected in equidistant bins at the bottom.

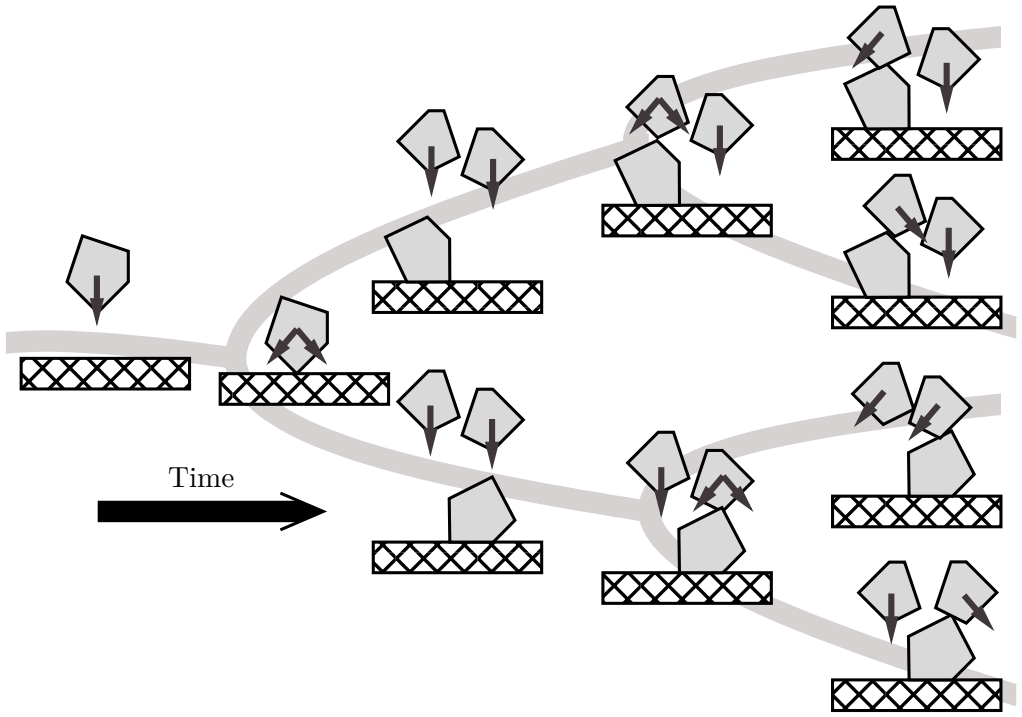

Fig. 7.2 Granular collisions, where minor differences in the initial position may lead to a cascade of different outcomes in the time evolution of particle positions. For the same initial states, vastly different final states are possible with only a tiny change of the initial position.

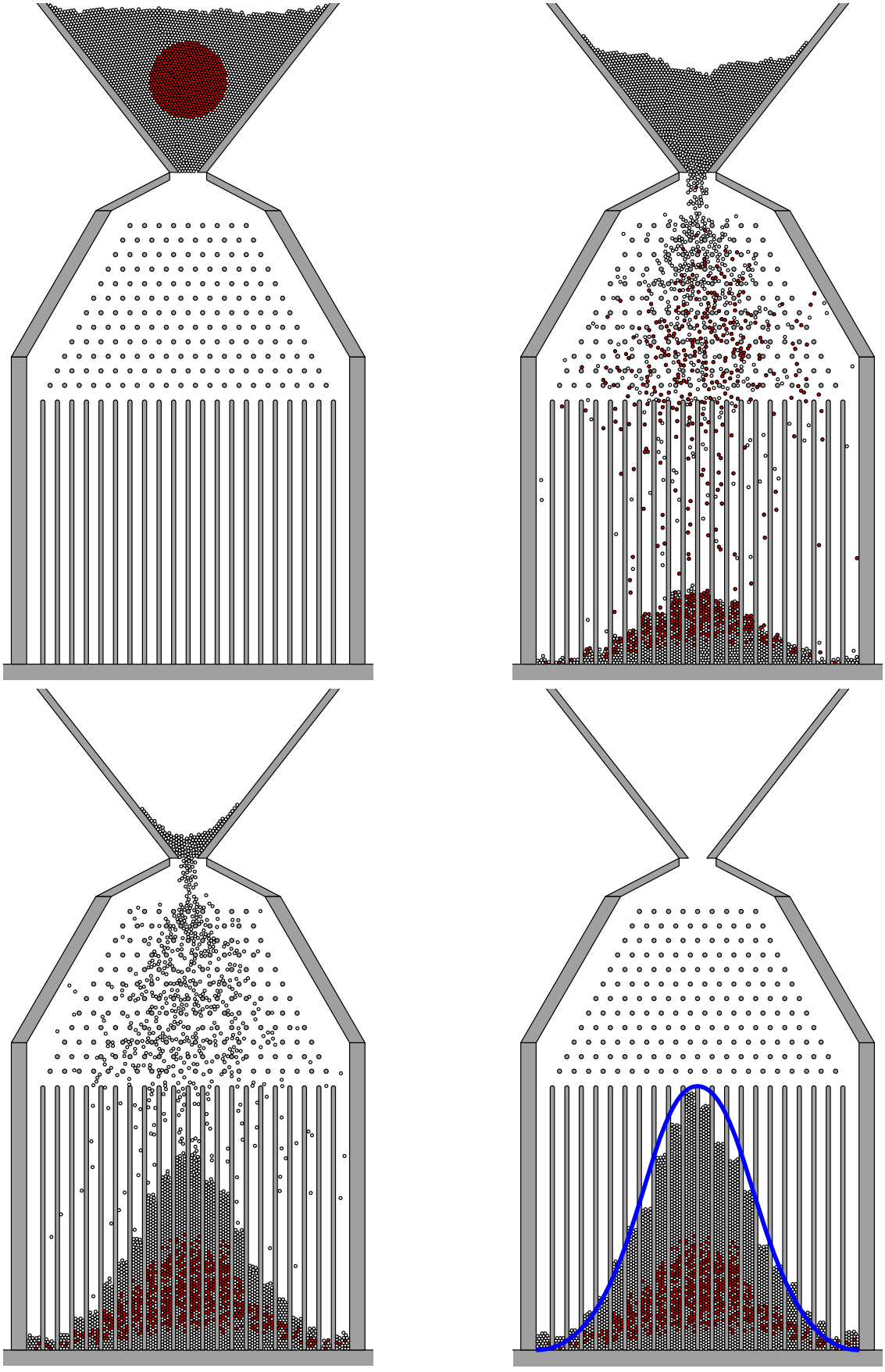

Fig. 7.3 Binomial scattering of particles into a binomial distribution in the Galton board due to the triangluar set of pins. While the initial condition shows an initially continuous red region, in the final configuration, white particles are scattered between the red ones and vice-versa due to the non-linearity of the interaction.

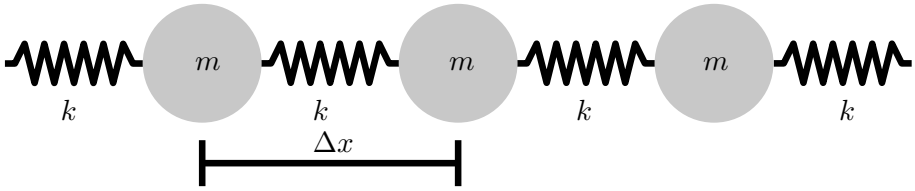

Fig. 7.4 Linear chain of discrete particles connected with springs.

The pins deflect the particles either to the left or to the right with equal probability, leading to a binomial outcome of the collisions and therefore to a binomial (normal) distribution in the height of the columns of particles at the bottom. The nonlinearity of the system is so severe, that particles in an initial compact region such as in the red "Hi-No-Maru"-circle in Fig. 7.3 top left, will be scattered into other regions, while white particles from the outside will be scattered between the red particles, see Fig. 7.3 bottom row. The Galton-board serves as a reminder that not everything which is computable is also useful as a variable, while on the other hand, systems with non-predictable trajectories may have other observables with highly predictable values. When the correctness of the friction implementation has to be verified, preliminary considerations are necessary which variables can reasonably be computed or verified, and which variables are affected by friction and which are not.

7.1.1 Sound velocity as an observable unaffected by friction

Various observables are affected by Coulomb friction in solids: In this section we show, that the sound velocity is not among them. For a linear chain of discrete particles connected with springs as in Fig. 7.4, the sound velocity can be represented as

$$c = \Delta x \cdot \omega, \tag{7.1}$$

where ω is the frequency of the oscillator given by the springs, and Δx their elongation. For a linear chain of undamped springs, the equation of the linear oscillator is homogeneous,

$$m\ddot{x} = -kx, \tag{7.2}$$

with reduced mass $m = (m_1 m_2)/(m_1 + m_2)$ and spring constant k. The oscillation frequency is given by

$$\omega_{\text{undamped}} = \sqrt{\frac{k}{m}}. \tag{7.3}$$

If the springs are viscously damped, the oscillator equation becomes

$$m\ddot{x} = -kx - b\ddot{x}, \tag{7.4}$$

with the damping constant b.

Then, the damped oscillation frequency is

$$\omega_{\text{damped}} = \sqrt{\frac{k}{m} - \left(\frac{b}{2m}\right)^2}. \tag{7.5}$$

For dry / Coulomb friction as damping mechanism, the oscillator equation becomes

$$m\ddot{x} = -kx - \mu|F^{\text{N}}|\text{sign}(\dot{x}), \tag{7.6}$$

which can according to the sign of the velocity be separated into two equations,

$$m\ddot{x} = -kx - \mu|F^{\text{N}}|,\ \dot{x} > 0 \tag{7.7}$$

$$m\ddot{x} = -kx + \mu|F^{\text{N}}|,\ \dot{x} < 0, \tag{7.8}$$

with a friction coefficient μ and a normal force F^{N}. Because this is the non-homogeneous augmentation of equation (7.2), the oscillation frequency does not change and we obtain again

$$\omega_{\text{fric}} = \sqrt{\frac{k}{m}} = \omega_{\text{undamped}}, \tag{7.9}$$

i.e. the sound velocity is independent of Coulomb friction. Nevertheless, the amplitude of propagating vibrations, i.e. the decay rate of sound will be strongly affected by Coulomb friction.

7.1.2 Mechanical stability as unmistakable observable

As shown in section 3.3.5, granular aggregates deflect forces sideways, which is the basis of long lasting arch structures. The mechanical stability of arches is an undeniable fact which must also be reproduced when simulations should be credible. For such problems, implementations without Coulomb friction will give not “slightly wrong”, but visible unphysical results. For a length-to-width relation of the Tingis Gate in Fig. 7.5, we have calculated the time evolution according to different friction implementations with the screenshots in Fig. 7.6. The blocks below the arch are fixed, the lower blocks in the arch are initialised with gaps. The arch without Coulomb friction ($\mu = 0.0$) shown in the top row collapses almost immediately. For a friction coefficient $\mu = 0.6$ (which is realistic for stone work, see ref. [128]), the implementation with Cundall-Strack friction (centre row) is stable, but the arrangement looses symmetry due to misaligned contacts, while the implementation with our DAE-friction results in a symmetric end configuration.

Fig. 7.5 Reconstruction of the Tingis Gate in Morocco from a building complex in Volubilis, dating from the 3rd century AD.

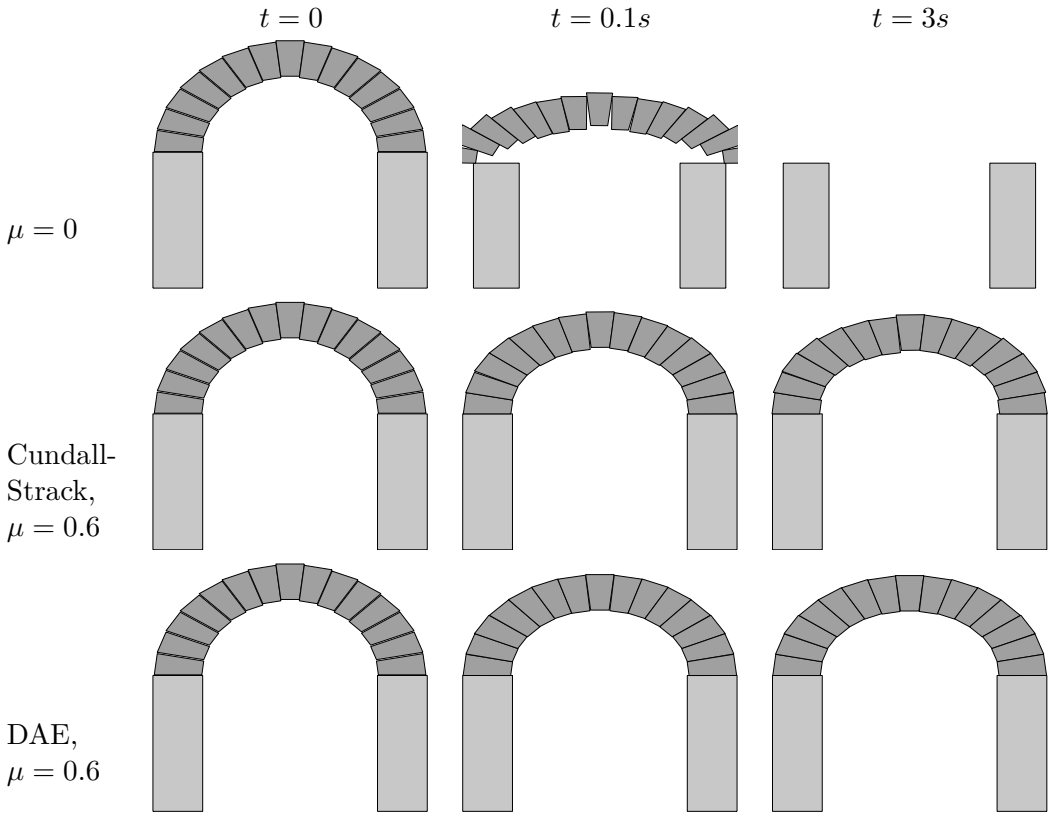

Fig. 7.6 Simulation of a granular arch without friction (top row) will lead to unphysical collapse. In simulations with Coulomb friction (middle row) the arch will remain stable, but the key stone will be slightly misaligned. In simulations with the DAE friction aproach, the arch will remain stable and well aligned.

7.2 Block leaning on a wall

For a block leaning on a wall as in Fig. 7.7 with angle 15°, the creep, i.e the velocity for the centre of mass, is computed. The edges where the block touches the wall are acute angles to mimic point-like contacts, the contact with the floor is frictional with $\mu = 0.6$, and the contact with the vertical wall is not frictional ($\mu = 0$) to simplify the comparison with the textbook example of a leaning ladder[129]. We want to determine which value for η in the damping deceleration $a^{(\eta)}_{\text{break}} = -(\eta v(t)/\tau - a(t))$, as discussed in sec. 5.4.5, gives the lowest drift away from the constraint $v = 0$ and how different integrators perform. The data for the BDF2-integrator are shown as full lines in Fig. 7.8. The smallest creep, and therefore the largest accuracy is obtained for a damping acceleration with $a^{(2)}_{\text{break}} = -(2v(t)/\tau - a(t))$ from eq. (5.56) derived under the assumption of residual constant velocity. For a timestep of $\tau = 10^{-5}$/[s] rather smaller than the minimal timestep τ_{min} in eq. (5.41) for this problem, we get a creep of 10^{-4} [m], so for a length of about 0.1 m, this means that we have a drift of about 1/1000 of the size per second, which is of the order of the overlap and therefore sufficient for most applications. The acceleration $a^{(1)}_{\text{break}} = -(v(t)/\tau - a(t))$ from eq. (5.56) based on a derivation with assumed vanishing error gives a larger creep. Reference data for damping forces with ad hoc chosen values like $a^{(0.5)}_{\text{break}} = -(0.5v(t)/\tau - a(t))$ gives a larger drift than $a^{(1)}_{\text{break}}$, and for $a^{(3)}_{\text{break}} - (3v(t)/\tau - a(t))$, the effective drift is comparable to $a^{(1)}_{\text{break}}$, but the sign of the velocity is alternating between successive timesteps. When we use an integrator which is not implicit, like the Heun method, the drift is considerably higher, the stability is considerably worse and for larger timesteps the particle drops to the floor immediately (Fig. 7.9). As the Heun method is part of the Runge-Kutta family of numerical integrators, it is an explicit, non-stiff numerical integrator. We chose the Heun integration scheme for comparison, as it could easily be implemented in predictor-

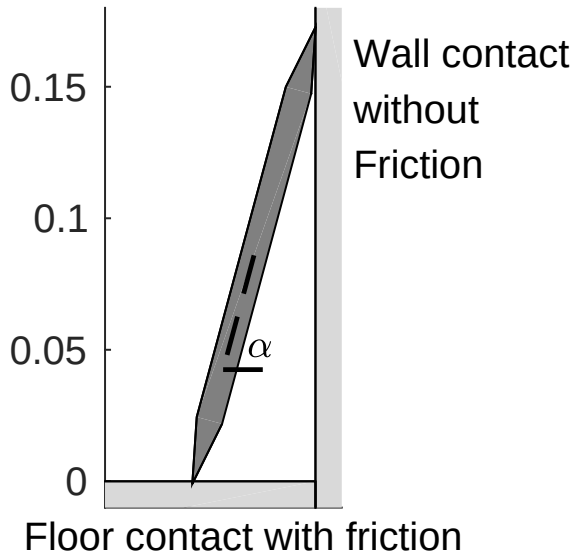

Fig. 7.7 Block leaning on a wall with the wall contact with $\mu = 0$ and the floor contact with $\mu = 0.6$.

corrector form, and therefore no change beyond renaming the integrator-call was required in the program flow, as opposed to other possible one-step methods.

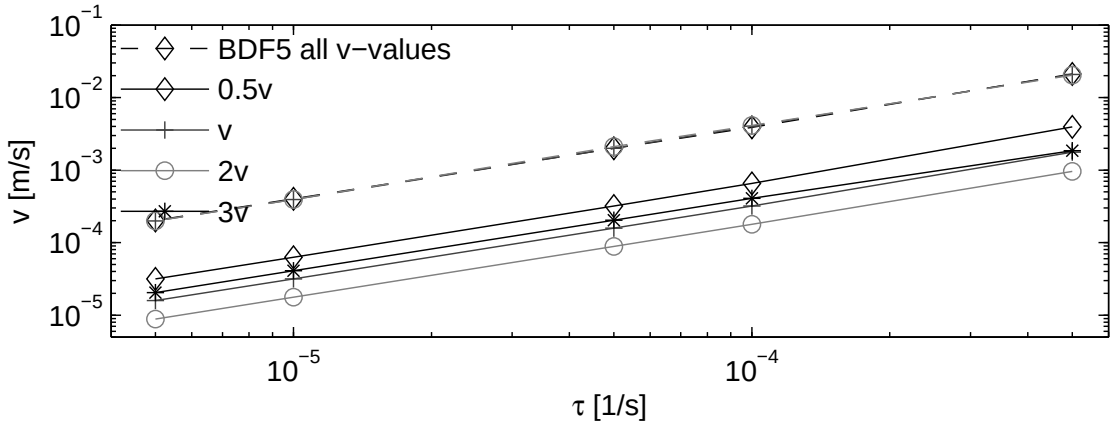

Fig. 7.8 Creep (stationary velocity) of the centre of mass for the block leaning on a wall in Fig. 7.7 for damping with $a_{\mathrm{dec}}^{(\eta)} = -(\eta v(t)/\tau - a(t))$ for different values of $\eta = 0.5$, 1, 2, 3 and τ. The data from BDF2 are marked with solid lines, the data from BDF5 are marked in dashed lines (practically on top of each other for different values of η).

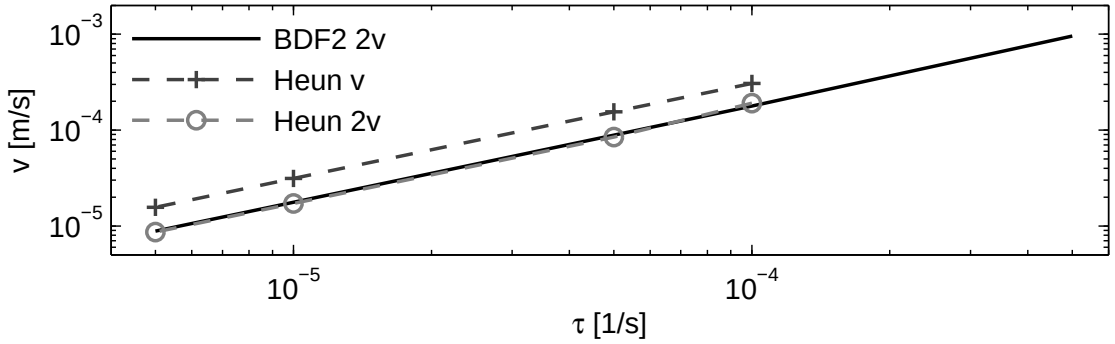

Fig. 7.9 Creep of the centre of mass for the block leaning on a wall in Fig. 7.7 using the Heun integration scheme for damping with $a_{\mathrm{dec}}^{(\eta)} = -(\eta v(t)/\tau - a(t))$ for different values of $\eta = 1$, 2 and τ. The data from Heun are marked with dashed lines, the reference data from BDF2 are marked in a solid black line. For larger timesteps the Heun method will not be stable.

7.3 A block sliding on a slope

While the case of a particle on a slope as in Fig. 7.10 looks simpler than a particle leaning on a wall, because there is only one contact, it is actually more difficult: The leaning particle has a rotational degree of freedom frozen out due to the second contact, while the particle on a slope may have a rotational oscillation which is difficult to damp out by a force computed for a single contact point with the ground alone. While the one-particle formalism for the centre of mass in sec. 5.3 would work for a rectangle moving in one

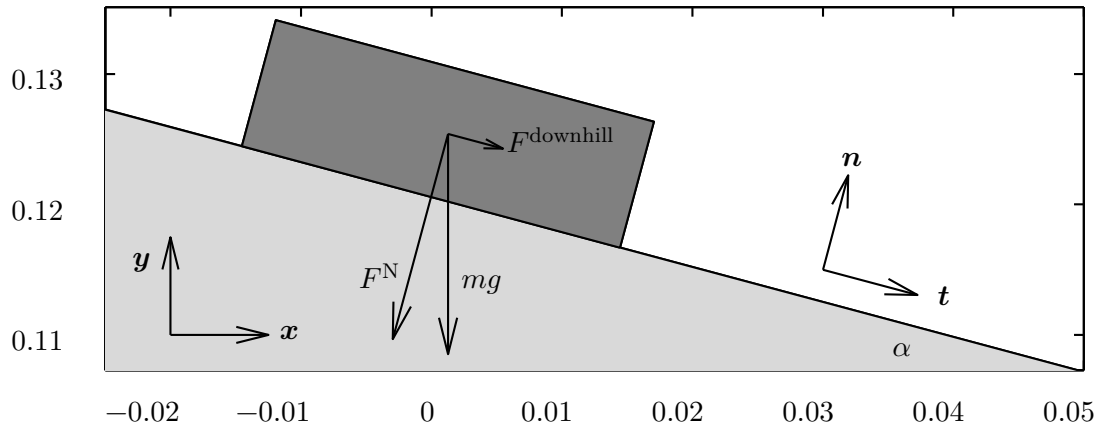

Fig. 7.10 Block with weight mg, normal force F^{N} and downhill force F^{downhill} on a slope with $\alpha = 15°$.

dimension along a linear slope without a rotational degree of freedom, we still have to prove that our many-body formalism in chapter 6 would work in a simulation where the centre of mass can move in $x-$ and $y-$direction with the possibility of a rotation around the centre of mass. As the problem is treated even in highschool, there are several alternative approaches which look feasible also for actual computer simulations. In particular, one may feel tempted to use (in brackets the abbreviations we have used in Figs. 7.11 and 7.12)

1. The theoretical value (THEO) for the friction force computed as the opposite of the downhill force, from the slope angle $\alpha = 15°$ as $F^{\text{Fric}} = -F^{\text{N}} \sin(\alpha)(\text{sign})(v) = -mg \sin(\alpha)(\text{sign})(v)$ (this formalism is oblivious to the possible particle rotation),

2. Dynamical friction (DYN) only, without any provision for static friction, in the hope that the integrator will somehow "fix" the overcompensation of forces,

3. our constraint approach (DAE),

4. the Cundall-Strack model (incrementation of a tangential spring force up to a value of μF^{N} without (tangential) damping (CS no damp.), see chapter 2.2, or

5. the Cundall-Strack model with (tangential) damping (CS w. damp.), see ch. 2.2.

We have used $\mu = 0.6$ for an angle of $\alpha = 15°$, which corresponds to about 50 % of the critical angle. Relevant for this case is not the actual coefficient of friction, but the relative size of the maxima / dynamical friction and the actual static friction value for the much lower slope. At first sight, one can see in Fig. 7.11 that the block is stopped fastest via the DAE-approach. Mathematically this is optimal, as the energy dissipation is maximal. The Cundall-Strack model takes longer to fix the particles, as the incrementation is bounded. It turns out that the theoretical constant value (THEO) is unable to stop the block altogether: As there is a small oscillatory motion both on the x, y-components as well as on the rotation, the theoretical value which is computed based on the weight

and not on the actually varying normal force is always slightly off with overcompensation of forces alternatingly downhill and uphill. That dynamical friction brings the block to a stop is rather "by luck": By a spurious cancellation of forward- and backward motion, together with normal damping, the BDF-2 integrator actually succeeds in stopping the block. The equilibrium point is clearly not in the range of physical equilibrium points which are obtained by DAE or CS. This will not happen for explicit integrators or purely one-dimensional modelling along the downhill direction, where a rhythmical (like one step back and two steps forward) motion lets the block slide downhill.

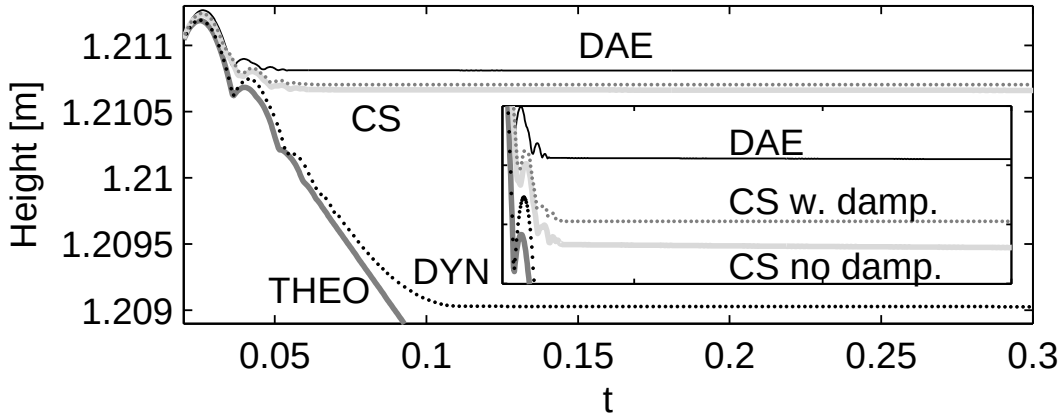

Fig. 7.11 Height of the block on a slope for different friction approaches, our differential algebraic equation (DAE), Cundall-Strack (CS) with and without damping, the theoretical (constant) value and the dynamic friction (Dyn) value.

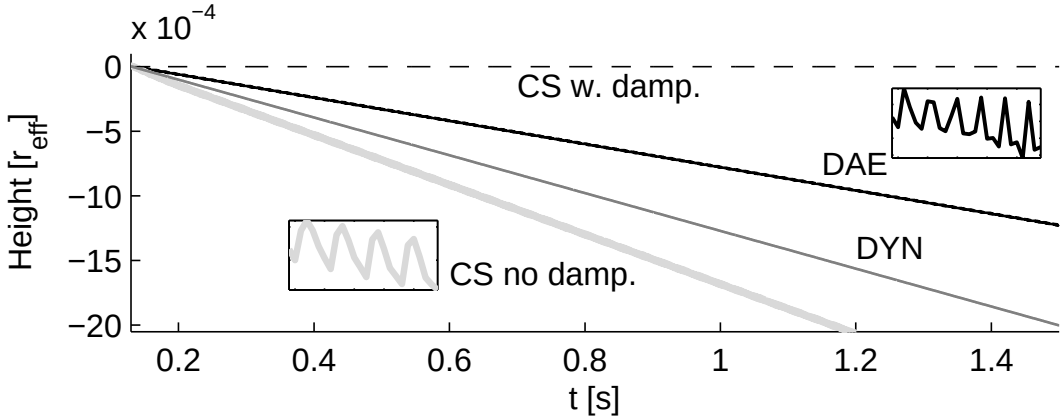

Fig. 7.12 The height of the block as in Fig. 7.11 for differential algebraic equation (DAE), Cundall-Strack (CS) with and without damping along the stationary state: For DAE and CS without damping, there is oscillatory (see insets) downhill creep. The trajectories for CS with damping and for dynamic friction (DYN) are without oscillations. The data is scaled with the effective particle radius to indicate the relative accuracy of the different methods.

While macroscopically and for short time scales, the DAE-approach and the CS-approach are satisfying, we also have to take a look at the long-term drift. The height in

Fig. 7.12 is scaled by the effective radius (or Sauter-radius)

$$r_{\text{eff}} = r_{\text{Sauter}} = \sqrt{\frac{A}{\pi}} \tag{7.10}$$

of the particle, to relate the length scale of the height to the actual particle size as an indicator of the relative accuracy. There is indeed a drift away from the constraint $v = 0$. The insert shows some that it is due to a more or less regular oscillatory motion around the constraint, with some net creep downhill. CS with tangential damping succeeds in eliminating this drift, because it has the mathematical structure of a Baumgarte stabilization, eq. (5.12) for constraint problems. A drift of the order of 0.1 % of the effective radius per second, as for the DAE approach, may not be a problem for most applications. As the creep depends on the initial conditions, it may change with the details of the problem: When we ran the simulation with the rotation switched off, for DAE the particle came to an absolute standstill with $v = 0$. The same happened for a square particle of the same cross-section area with rotation.

7.4 Vibrated box

The understanding of systems of granular particles under vibration is important for many issues relating to fluidisation, onset of convection etc. In the Cundall-Strack model, the frictional constraint eq. (1.2) is replaced by a spring, i.e. a degree of freedom, which can then again release this energy. In situations with preferred directions of motion and flow, e.g. formation of heaps from hoppers or chute flow, such spontaneous releases, as well as the retarded grip, will hardly influence the physicality of the simulation. Nevertheless, for vibrated systems, the situation is different: The oscillatory motion may either delay the grip and impede the build-up of the actual friction force, or may load up some "tangential springs" so that their energy is released when other contacts of the same particle are loosened. To investigate this problem, we consider the box in Fig. 7.13 filled with 1008 particles of average diameter 1[cm] with an average mass of 0.3407[kg] ($6.8139 \cdot 10^{-5}\text{m}^2$

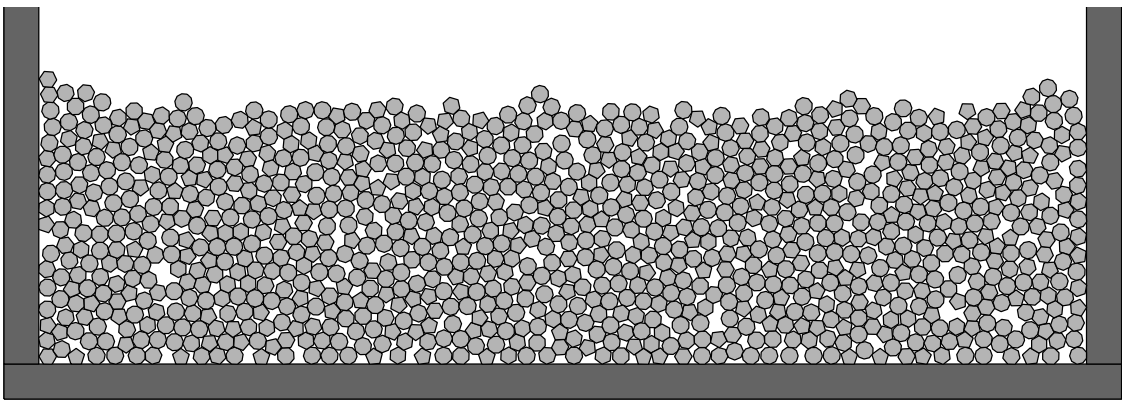

Fig. 7.13 Vibrated box (walls are higher than shown) with DEM-particles.

average cross section) under gravity $g = 9.81[\mathrm{m/s}]^2$. We vibrate the box in a sinusoidal motion with frequency $\omega = 8.58$ [Hz] and amplitude $A = 0.1$ [m], so that the Froude-number, i.e. the dimensionless acceleration,

$$\Gamma = \frac{A\omega^2}{g} = 0.75, \tag{7.11}$$

is below the gravitational acceleration, therefore, the particle agglomerate should move like a fixed block, with hardly any individual motion. When friction locks all particles together, the time evolution of the average velocity of the centre of mass

$$v^{\mathrm{com}} = \frac{\sum_i^N m_i v_i}{\sum_i^N m_i}. \tag{7.12}$$

should be sinusoidal, as the motion of the box itself. Accordingly, the kinetic energy of the centre of mass

$$E^{\mathrm{com}} = \frac{1}{2}\left(\sum_i^N m_i\right)||v^{\mathrm{com}}||^2 \tag{7.13}$$

would be sinusoidal, too. We can also consider the kinetic energy of the particles whose motion deviates from the motion of the centre of mass.

$$E^{\mathrm{dev}} = \frac{1}{2}\sum_i^N m_i||v_i - v^{\mathrm{com}}||^2. \tag{7.14}$$

as a parameter of the particles moving independently, i.e. which are not fixed by the static friction. Due to the low Froude-number, the forces between the particles are below the gravity acceleration, and the particles should move mostly like a single block. This is consistent with the sine-like time evolution of the centre of mass for the DAE-implementation in Fig. 7.14, while the system with Cundall-Strack implementation shows significant deviations. The complementary data in Fig. 7.15 show that the kinetic energy of independently moving particles is higher for the Cundall-Strack implementation. That there is a certain motion which deviates from the motion of the centre of mass is due to the fact that some particle regions can reorder due to the balance in the normal forces, tangential forces and the loads induced by the accelerations in the vibration. The implication for liquefaction problems under vibration is that reliable results can only obtained with a DAE-implementation, the Cundall-Strack friction has problems to “fix” particles under external oscillating forces. For problems with periodic vibrations, no reliable simulations can be expected for the Cundall-Strack approach.

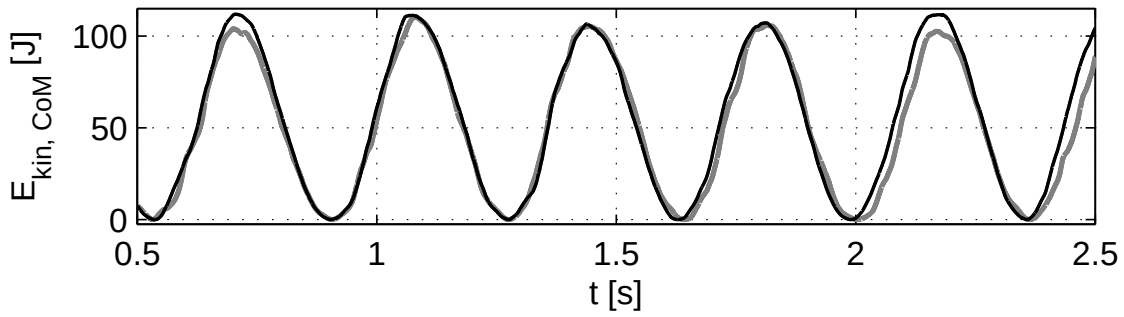

Fig. 7.14 Centre of mass energy for the system in Fig.7.13: $E_{\text{kin, COM}} = \frac{1}{2}(\sum_i^N m_i)v_{\text{COM}}^2$ with the DAE method (black) and the CS method (gray).

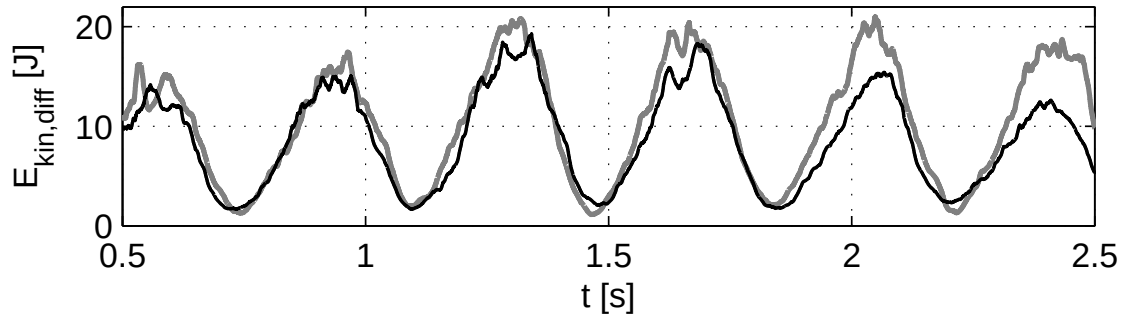

Fig. 7.15 Difference between centre of mass energy and particle energy for the system in Fig.7.13: $E_{\text{kin, diff}} = \sum_i^N \frac{1}{2} m_i(v_{\text{COM}} - v_i)^2$ for the DAE method (black) and the CS method (gray).

7.5 Friction in a heap

A sand heap is the ultimate test for the static friction evaluation of a multi-body system. To compute the friction so that the particles stay in a force equilibrium essentially reveals the physicality of the approach. For the configuration in Fig. 7.16 with 1622 particles with a Sauter mean diameter of 6.2[mm], we can compare the decay of the centre of mass for the DAE approach and the CS approach in Figs. 7.17 and 7.18. As unit, we use again the Sauter mean diameter of (in two dimensions) a circle equal to the the average particle area to relate the magnitude of the drift to the particle size. The Cundall-Strack friction has the smaller drift, because it is actually a kind of Baumgarte-Stabilization for the frictional

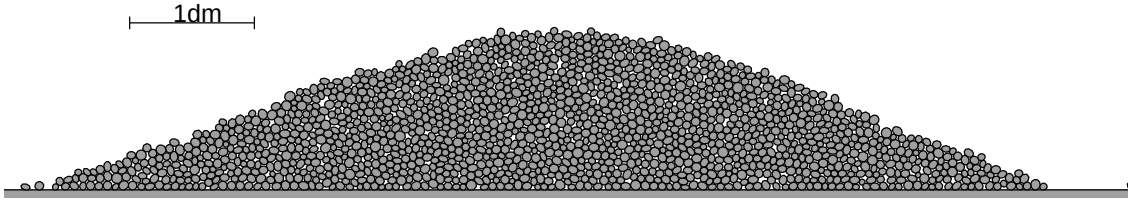

Fig. 7.16 Heap with 1622 particles for which the static friction is computed. The rounding of the apex is not due to a failure of the friction law, but due to the scattering of particles in the preliminary simulation in which the initial positions were determined.

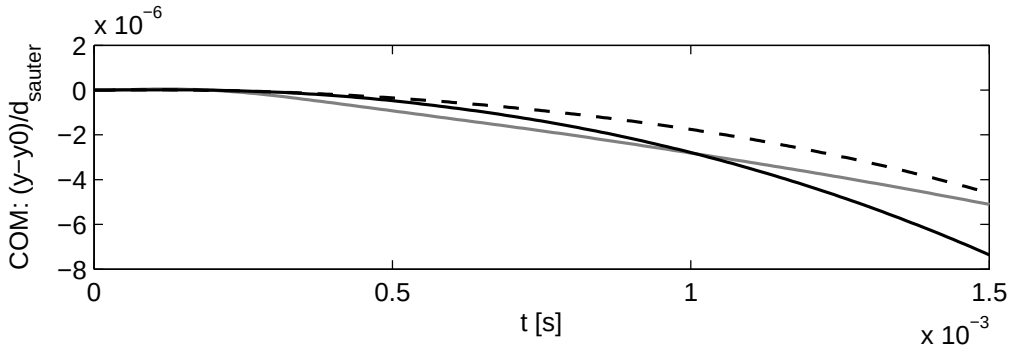

Fig. 7.17 Decay of the centre of mass height for the heap in Fig. 7.16 in Sauter diameters with DAE-friction (black) and Cundall-Strack-friction (gray) in the short term with $\tau_1 = 10^{-5}$s. DAE-friction with half the timestep $\tau_2 = 0.5\tau_1$ is shown in a dashed black line. Friction is gripping faster for the DAE method than for the Cundall-Strack model, while for longer times the Cundall-Strack-friction is inherently self-stabilizing.

contacts. As can be seen from Fig. 7.17, up to $0.25 \cdot 10^{-3}$[s], the height for both models is unchanged. Then creep sets in and DAE- and Cundall-Strack friction are equivalent up to 10^{-3}[s]. For longer times, the creep in the DAE-friction is more marked, but even for a timescale of 1[s] it is only of one tenth of a particle (Sauter-) diameter (Fig. 7.18). The constant drift velocity shows that in accordance to Newton's first law, the DAE-algorithm computes the force equilibrium correctly: The DAE-algorithm is just not able to fix the configuration. The drift is smaller for smaller timesteps due to lower numerical noise. Nevertheless, when we look at the average kinetic energy per particle in Fig. 7.19, we see another artefact: While the the energy fluctuations are random for our DAE-approach, the stable heap with Cundall-Strack friction shows unphysical residual (constant) oscillation, with an oscillation frequency of about,

$$\omega_{\text{ekin}} \approx 50\text{Hz}. \tag{7.15}$$

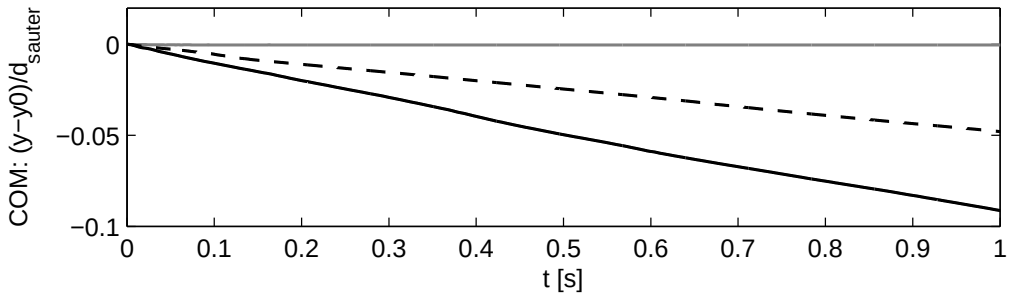

Fig. 7.18 Decay of the centre of mass height for the heap in Fig. 7.16 in Sauter diameter with DAE-friction (black) and Cundall-Strack-friction (gray). DAE-friction with half the timestep is shown in a dashed black line. For longer time spans the DAE method reaches force equilibrium, so the centre is creeping with constant velocity in accordance with Newton's first law that a system in force equilibrium can propagate at constant velocity. A lower timestep decreases the creep.

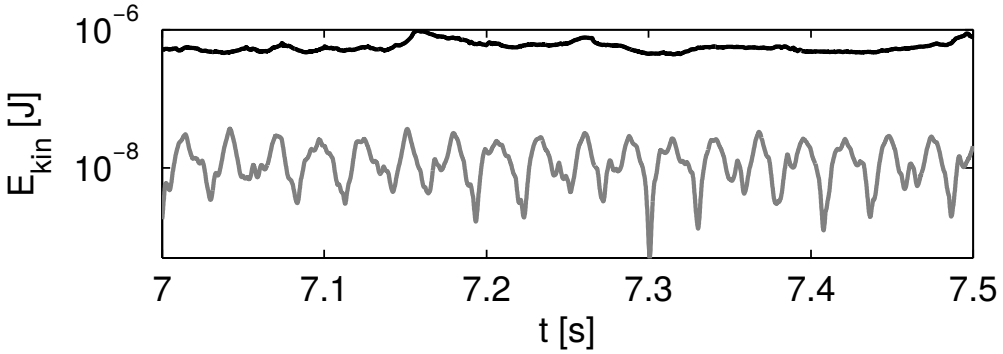

Fig. 7.19 Time dependence of the kinetic energy per particle for the heap in Fig. 7.16 with DAE-friction (black) and Cundall-Strack-friction (gray).

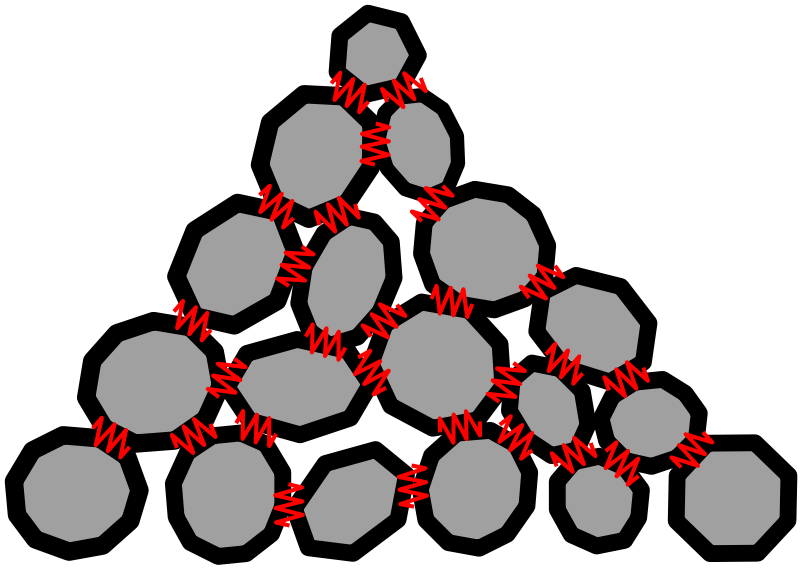

Fig. 7.20 With the Cundall-Strack model, the particle is embedded in a spring network, leading to persistent lattice vibrations. Residual rotational energy can be dissipated through damped oscillations in tangential direction.

In the Cundall-Strack model, see Sec. 2.2, tangential forces are modelled via springs. We can derive the oscillation frequency frequency of these springs as

$$\omega_{\mathrm{CS}} = \sqrt{\frac{Y_{\mathrm{CS}}}{\sum m_i}} \approx 50\mathrm{Hz}, \tag{7.16}$$

and evaluate it, using the total mass of the heap, $\sum m_i$, and the stiffness of the tangential spring, $Y_{\mathrm{CS}} = \frac{2}{7}Y$. As the theoretical oscillation frequency of the Cundall-Strack model matches with the measured oscillation frequency, we can confirm that the oscillations in the kinetic energy in Fig. 7.19 are resonances of the Cundall-Strack model. As the Cundall-Strack friction model is a spring model, particles are embedded within a spring-network, mediated through their contacts, as shown in Fig. 7.20. This means, that residual kinetic energy can propagate as persistent lattice vibrations through the granular contact network, visible as constant oscillations in the velocity, respective the kinetic energy.

7.6 Equilibration of particles in a resting box

When we place particles in a box, such as in sec. 7.4, when no external excitation applies and the box is at rest, we expect the system to equilibrate, and the mean velocity to decay towards zero, apart from numerical errors and inconsistencies in the force modelling. However, when we look at the mean kinetic energy in Fig. 7.21, instead of an exponential viscous decay or a fast, linear dry-friction decay, we find instead unphysical stagnation of the energy, with a large number of energy spikes from reordering of particles, even in mechanical equilibrium. Energy dissipation via fixed walls still works, but its influence is too subdued to be useful and reintroduction of kinetic energy by means of reorientation will further stall dissipation. When we (unphysically) disable the rotational degrees of freedom for the particles, we get the desired decay towards zero and, additionally, much less reordering of the configuration, see Fig. 7.21. The residual kinetic energy in the equilibrium state for DAE, together with residual energy oscillations for the CS-model (as shown in Fig. 7.19) show, that the DEM-approach has a problem with residual rotation in its equilibrium state. But, whereas the Cundall-Strack friction model includes a crude form of Baumgarte stabilisation for the particle orientation by design, our DAE friction formalism does not, and requires supplementary stabilisation for the constraints of position and orientation. It is the purpose of the next chapter to investigate the micromechanical reason behind this residual energy and to develop a stabilization method for the rotational degrees of freedom.

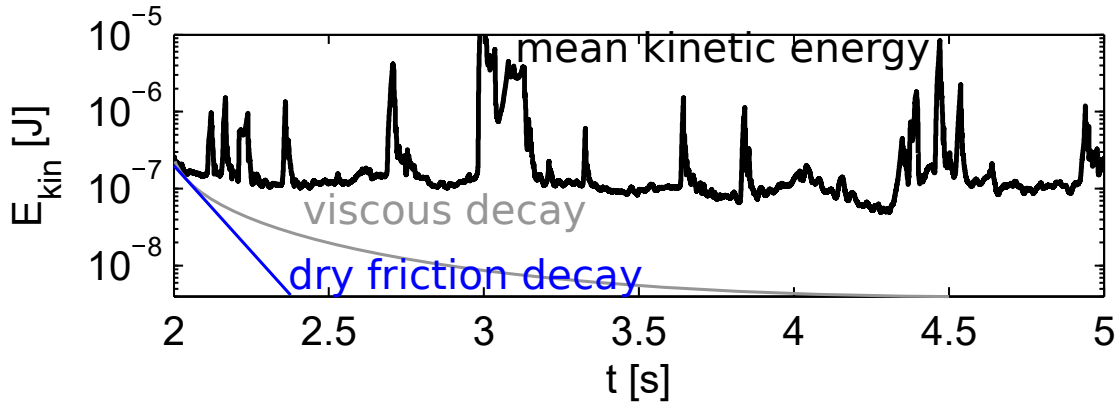

Fig. 7.21 Unphysically stagnating mean kinetic energy for particles in a resting box, instead of the expected viscous or dry-friction decay. Spikes indicate sudden reordering of the configuration.

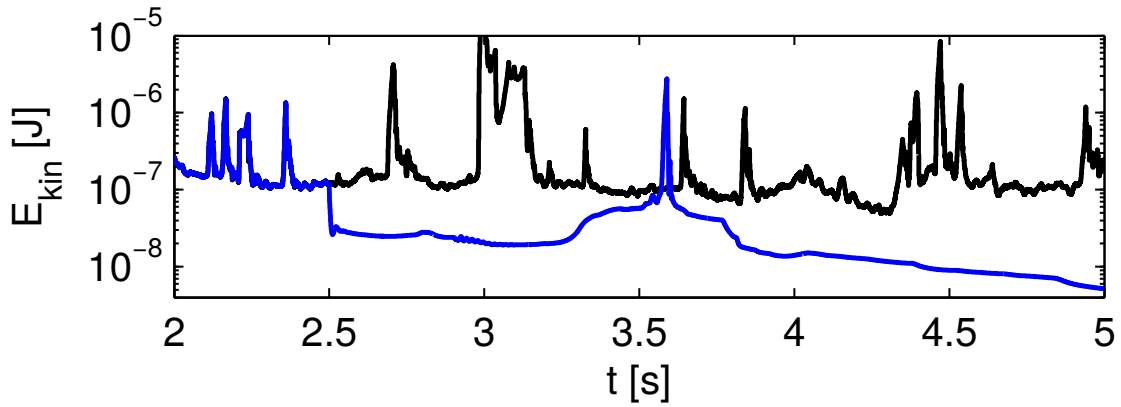

Fig. 7.22 If the rotational degrees of freedom are (unphysically) disabled at 2.5 seconds, the energy decay meets physical expectations and decays towards zero (blue line). In addition, the system shows much less reordering than with physical rotation allowed (black line).

Chapter 8

Stabilization

As we have shown in chapter, 4.2, residual energy in the rotational degrees of freedom will lead to inconsistencies in the force balance and orientation of the contact vectors. For the static granular heap in section 7.5, our "numerically exact" friction shows residual kinetic energy. The irregular oscillations do not go to zero, while in the physical situation, the grains come to a standstill immediately. As the oscillations become smaller with the timestep τ, it is obviously a problem of the discretisation error. Within a single timestep, the rectilinear coordinates as well as the angular coordinates are accurate up to a discretization error $\epsilon(\tau^n)$, the (angular) velocities are accurate up to $\epsilon(\tau^{n-1})$, and the (angular) accelerations up to $\epsilon(\tau^{n-2})$. The standard approach for DAEs is to use stabi-

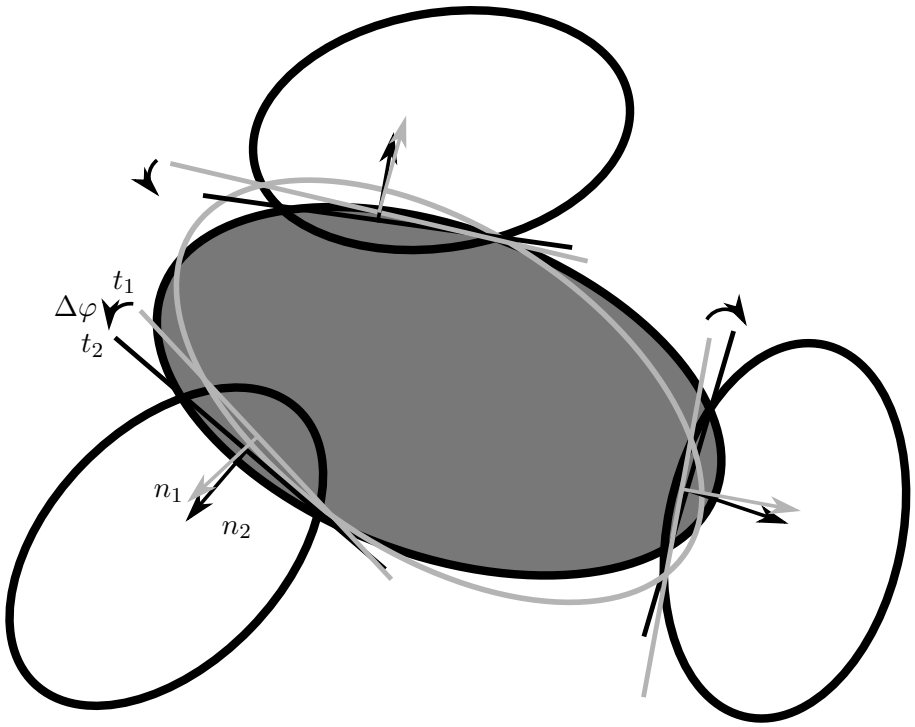

Fig. 8.1 Residual rotation will lead to small changes in the contact orientation $\Delta\varphi$, and possibly unbalanced forces, inducing additional noise in the rectilinear degrees of freedom.

lization techniques which "fix" the system along the algebraic constraints: Either only the solution component is taken which is in accordance with the constraint ('stabilization by projection", see [102, 103, 1] and section 5.1.4), or the deviation is damped out to converge towards the constraint ("Baumgarte stabilization", see [101, 1] and section 5.1.4). The Cundall-Strack friction model behaves like a crude form of Baumgarte stabilization (see sec. 2.2) which will restore the particle to an equilibrium, but unfortunately, there are always persistent periodic oscillations in the kinetic energy (Fig. 7.19). Various stabilization approaches exist for mechanical systems[130] so that positions are restored, but for granular systems, the issue is not the average position, but the fluctuation of the velocities, including the angular velocities. When we switch off the rotation, the fluctuations in the velocities vanish immediately, so the reason for the residual energy is the inconsistency of angular and linear degrees of freedom as in Fig. 8.1: Particle rotation changes the overlap and therefore the magnitude and direction of the linear forces, which in turn cause a change of the torques, and so on. Changing the friction law of the linear degrees of freedom for individual contacts will not help, the forces will fluctuate independently and induce rotation. We have tried to damp this spurious motion with various velocity dependent terms, but none of them was successful, the coupling introduced by the geometric inconsistencies is too noisy and too weak to successfully damp out the motion. For our DAE-friction, a stabilization approach is needed which removes the noise amplitudes, takes into account the situation at the static contacts, but wipes out the surplus kinetic energy in the angular degrees of freedom directly before the motion can be fed back into the rectilinear degrees of freedom. As a more forceful coupling becomes necessary which can actually "fix" the orientation additionally to the positions, we decided to extend our DAE-formalism to the angular degree of freedom to stabilize the simulation against spurious oscillations, which have last not least, the unwelcome effect of an "external" vibration. In this chapter, we develop an analogy between friction and the damping of rotation, and explain the analogies and differences.

8.1 Angular velocity as indicator function

For static friction in the rectilinear degrees of freedom, the indicator function is the particle velocity, respective the relative velocity at the contact point. Similarly for stabilization of the particle orientation in the angular degrees of freedom, we can choose the angular velocity ω as indicator function. Nevertheless, the angular motion is not the relative motion of contacting particles, but the relative rotation to the whole surrounding matrix of particles. The indicator function will then be the relative rotation

$$\widetilde{\omega} = \omega - \omega_0, \tag{8.1}$$

where ω_0 is the rotation of the surrounding granular matrix, obtained from weighting the rotation of the contacting particles around the particle with the elastic normal force $F_i^{\mathrm{el,N}}$

of the contacts,

$$\omega_0 = \frac{\sum_i^N \omega_i |r_i F_i^{\mathrm{el,N}}|}{\sum_i^N |r_i F_i^{\mathrm{el,N}}|} \quad \forall \text{ contacts } i, \tag{8.2}$$

where the angular velocity at the contact due to the motion of the particle j is given by

$$\omega_i = \frac{|\boldsymbol{v} \times \boldsymbol{r}|}{|\boldsymbol{r}_j|^2} = \frac{v_{x,j} r_{y,j} - v_{y,j} r_{x,j}}{|\boldsymbol{r}_j|^2} \quad \text{(in two dimensions)}, \tag{8.3}$$

where v is the velocity at the contact point and r the distance from the centre of mass to the contact point. Whereas the static friction at every contact can be dealt with independently, the particle rotation is influenced by the sum of all damping torques from every single contact of the particle. That means, a simultaneous balancing of all torques will be necessary.

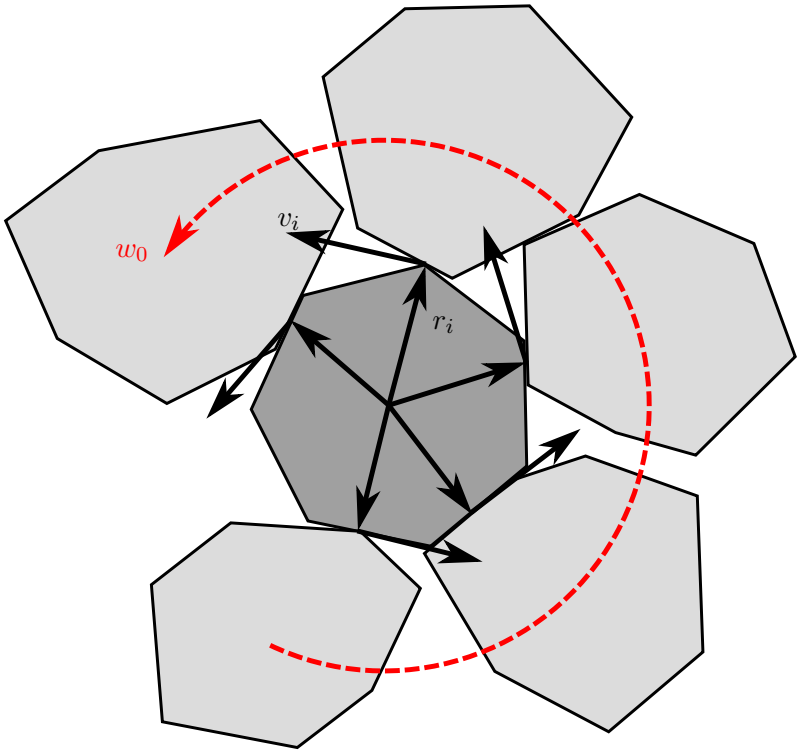

Fig. 8.2 The rotation of a particle within other particles is influenced by the motion of the whole surrounding granular matrix rotation, which for rigid body rotation of the surrounding granular matrix can be expressed with an angular velocity ω_0.

8.2 Damping in analogy to the static friction formalism

To stabilize the simulation with respect to inconsistencies in rotation and translation due to shape, we follow the formalism for static friction explained in chapter 5. Differences exist in several aspects, which we will explain here in more detail. Table 8.1 provides a comparison between the components and conditions of the two formalisms. In analogy to

eqs. (6.4,6.5) for the static friction formalism we can separate the torque to the left and the right of the indicator function eq. (8.2),

$$T_I = T^{\text{ext}} - T^{\text{dyn}}_{\text{abs}}, \tag{8.4}$$

$$T_{II} = T^{\text{ext}} + T^{\text{dyn}}_{\text{abs}}, \tag{8.5}$$

T^{ext} is the torque due to elastic forces and dynamic friction forces acting upon the particle,

$$T^{\text{ext}} = T^{\text{el}} + T^{\text{dyn}}, \tag{8.6}$$

where T^{el} is the torque due to elastic forces at all contacts i of the particle,

$$T^{\text{el}} = \sum_i^N \boldsymbol{r} \times \boldsymbol{F}^{\text{el}}, \tag{8.7}$$

and T^{dyn} the torque due to friction forces on all contacts k with dynamic friction,

$$T^{\text{dyn}} = \sum_k^N \boldsymbol{r} \times (\mu F^{\text{el}} \boldsymbol{t}). \tag{8.8}$$

Because the convex hull for static friction is computed from the absolute values of the friction coefficient and the normal force $|\mu F^{\text{N}}|$ with respect to the indicator function, we also need the positive sum of all possible torques due to static friction. This $T^{\text{dyn}}_{\text{abs}}$ in eqs. (8.4,8.5 is defined with the absolute value, as it has to be used with respect to the sign of the indicator function $\widetilde{\omega}$ (from eq. (8.2)) as

$$T^{\text{dyn}}_{\text{abs}} = \sum_j^N |\boldsymbol{r} \times (\mu F^{\text{N}} \boldsymbol{t})|, \tag{8.9}$$

summed over all contacts j of the particle with static friction. In analogy to the auxiliary variables a_I, a_{II} for the static friction formalism we introduce the auxiliary variables for the phase flow for rotation as

$$b_I = +\frac{T_I}{I} = +\left(\frac{T^{\text{el}}}{I} + \frac{T^{\text{dyn}}}{I} + \frac{T^{\text{dyn}}_{\text{abs}}}{I}\right), \tag{8.10}$$

$$b_{II} = -\frac{T_{II}}{I} = -\left(\frac{T^{\text{el}}}{I} + \frac{T^{\text{dyn}}}{I} - \frac{T^{\text{dyn}}_{\text{abs}}}{I}\right). \tag{8.11}$$

The case of dynamic friction (analogously to conditions 1. and 2. in section 5.3.2) is then given by

$$b_I < 0 \quad \text{and} \quad b_I > 0, \quad \text{or} \tag{8.12}$$

$$b_I > 0 \quad \text{and} \quad b_I < 0. \tag{8.13}$$

The torque acting upon the particle is then the sum of all torques due to the external forces, eq. (8.6), which we will call "external torque".,

$$T = T^{\text{ext}}. \tag{8.14}$$

As long as there is not more than a single contact with static friction, the torques are computed this way.

With more than one static friction contact, the particle should come to a standstill with respect to the surrounding granular matrix, so in that case, a formalism analogously to static friction has to be used, with a Lagrange multiplier which fixes the orientation of the particle within the surrounding granular matrix, irrespective of the numerical error. Whereas the DAE friction formalism treats every contact separately, the torque to damp the rotation has to be computed based on all other torques acting simultaneously on the particle.

In the case that there are two or more contacts that fullfill the requirements for static friction, the orientation of the particle is constrained, and we have to verify that the signs of both auxiliary variables are negative, i.e.

$$b_I < 0 \text{ and } b_I < 0, \tag{8.15}$$

so that we can apply the rotation damping formalism. If the condition for the number of static contacts and for the sign of the auxiliary variables are both fullfilled, then we find the applying damping torque in the convex hull of T_I and T_{II}. The Lagrange parameter for rotation damping is defined with the torques instead of the auxiliary variables as

$$\lambda^{\text{rot}} = \frac{T_I}{T_I + T_{II}} \quad \in [0, 1], \tag{8.16}$$

which guarantee smoothness of the force law. The damping torque can then be computed from the convex hull,

$$T^{\text{damp}} = (1 - \lambda^{\text{rot}})T_I + \lambda^{\text{rot}} T_{II}. \tag{8.17}$$

The final torque acting upon the particle is then

$$T = T^{\text{el}} + T^{\text{dyn}} + T^{\text{damp}}. \tag{8.18}$$

8.3 Treatment for residual angular velocity

The stabilization approach detailed above works on the assumption that $\widetilde{\omega} = 0$. When we use constant timesteps, we will only be close to $\widetilde{\omega} = 0$, with small but finite residual angular velocities which will not be compensated by the damping torque derived under the assumption of zero angular velocity. To bring the rotation to a complete stop, we

therefore require an additional torque. In analogy to equation (5.55), we can include an angular acceleration for finite timesteps as

$$\dot{\omega}^{\text{res}} = -\left(\frac{\widetilde{\omega}}{\tau} - \dot{\omega}\right), \tag{8.19}$$

with the current angular acceleration $\dot{\omega}$ of the particle. Equation (8.18) then expands into

$$T = T^{\text{el}} + T^{\text{dyn}} + T^{\text{damp}} + I\dot{\omega}^{\text{res}}. \tag{8.20}$$

Table 8.1 Comparison of the static friction formalism and the rotation damping formalism in analogy to the static friction formalism.

Quantity	static friction	rotation damping
Area of action	local, single contact	entire particle, all contacts
Indicator function	$v_{\mathrm{rel}} = v_1 - v_2$	$\widetilde{\omega} = \omega - \omega_0$ $\omega_0 = \dfrac{\sum_i^N \omega_i \lvert r_i F_i^{\mathrm{el,N}}\rvert}{\sum_i^N \lvert r_i F_i^{\mathrm{el,N}}\rvert} \quad \forall$ contacts i
Acceleration	$a_{\mathrm{rel}} = \dot{v}_{\mathrm{rel}}$	$\dot{\omega}$
Absolute value of dynamic friction	$F_{\mathrm{abs}}^{\mathrm{dyn}} = \mu \lvert F^{\mathrm{N}}\rvert$	$T_{\mathrm{abs}}^{\mathrm{dyn}} = \sum_j^N \left\lvert \boldsymbol{r} \times \left(\mu F^{\mathrm{N}} \boldsymbol{t}\right)\right\rvert$ $\forall$ static contacts j
Forces / Torques from left / right	$F_I = F^{\mathrm{ext}} - F_{\mathrm{abs}}^{\mathrm{dyn}}$ $F_{II} = F^{\mathrm{ext}} + F_{\mathrm{abs}}^{\mathrm{dyn}}$	$T_I = T^{\mathrm{ext}} - T_{\mathrm{abs}}^{\mathrm{dyn}}$ $T_{II} = T^{\mathrm{ext}} + T_{\mathrm{abs}}^{\mathrm{dyn}}$
external forces / torques	$F^{\mathrm{ext}} = m \cdot a_{\mathrm{rel}}^{\tan}$	$T^{\mathrm{ext}} = T^{\mathrm{el}} + T^{\mathrm{dyn}}$
Dynamic friction / torques due to dyn. fric.	$F^{\mathrm{dyn}} = -\mu \lvert F^{\mathrm{N}}\rvert \mathrm{sgn}(v_{\mathrm{rel}})$	$T^{\mathrm{dyn}} = \sum_k^N \boldsymbol{r} \times \left(\mu F^{\mathrm{N}} \boldsymbol{t}\right)$ $\forall$ dyn. contacts k
Torque due to elast. force		$T^{\mathrm{el}} = \sum_i^N \boldsymbol{r} \times \boldsymbol{F}^{\mathrm{el}} \quad \forall$ contacts i
Auxiliary variables / phase flow	$a_I = +\dfrac{F_I}{m}$ $= + \left(a_{\mathrm{rel}}^{\tan} - \mu \dfrac{\lvert F^{\mathrm{N}}\rvert}{m}\right)$	$b_I = +\dfrac{T_I}{I}$ $= + \left(\dfrac{T^{\mathrm{el}}}{I} + \dfrac{T^{\mathrm{dyn}}}{I} - \dfrac{T_{\mathrm{abs}}^{\mathrm{dyn}}}{I}\right)$
	$a_{II} = -\dfrac{F_{II}}{m}$ $= - \left(a_{\mathrm{rel}}^{\tan} + \mu \dfrac{\lvert F^{\mathrm{N}}\rvert}{m}\right)$	$b_{II} = -\dfrac{T_{II}}{I}$ $= - \left(\dfrac{T^{\mathrm{el}}}{I} + \dfrac{T^{\mathrm{dyn}}}{I} + \dfrac{T_{\mathrm{abs}}^{\mathrm{dyn}}}{I}\right)$
Condition for dynamic friction	$a_I < 0,\ a_{II} > 0$ $a_I > 0,\ a_{II} < 0$	$b_I < 0,\ b_{II} > 0$ $b_I > 0,\ b_{II} < 0$
Force computation for dynamic case	$F = F^{\mathrm{ext}} - \mu \lvert F^{\mathrm{N}}\rvert \mathrm{sgn}(v_{\mathrm{rel}})$	$T = T^{\mathrm{el}} + T^{\mathrm{dyn}}$
Cond. for static friction / damping regime	sign-change of v_{rel}	≥ 2 stat. contacts
Cond. for static friction / damping	$a_I < 0,\ a_{II} < 0$	$b_I < 0,\ b_{II} < 0$
Lagrange-parameter	$\lambda = \dfrac{a_I}{a_I + a_{II}} \in [0, 1]$	$\lambda^{\mathrm{rot}} = \dfrac{T_I}{T_I + T_{II}} \in [0, 1]$
Static friction / rotation damping	$F^{\mathrm{stat}} = (1 - \lambda) F_I + \lambda F_{II}$	$T^{\mathrm{damp}} = (1 - \lambda^{\mathrm{rot}}) T_I + \lambda^{\mathrm{rot}} T_{II}$

8.4 Numerical verification

We apply our damping formalism to a series of increasingly complex problem geometries. The simulation parameters are the same as for the verification of the friction algorithm in table 7.1.

8.4.1 Two leaning particles

If we take two particles and lean them onto each other (Fig. 8.3), the resulting equilibrium is fragile. So the slightest imbalance of forces and torques will result in the configuration toppling to one side or the other. We initialise the particles slightly apart, so there will be an initial rotation until the particles make contact with each other. The damping formalism must not inhibit this initial rotation, only act to stabilise the final configuration. When we look at the angular velocity in the equilibrium position, we find that with our damping formalism, the rotation decays faster towards zero than without, compare Fig. 8.4. In the long term however, the oscillations in the damped case decay slower than in the undamped case, as the rotational damping has also affected the residual rectilinear motion. When we look at the horizontal centre of mass position we find a strong deviation from the original centre of mass, coupled with strong oscillations around its equilibrium position, for the configuration without rotation damping, while the damped configuration is essentially stable (Fig. 8.5). The situation is slightly different for the vertical component of the centre of mass position. Here, the damped case shows stronger oscillations in the long term than the undamped case, though the order of magnitude is the same (Fig. 8.6).

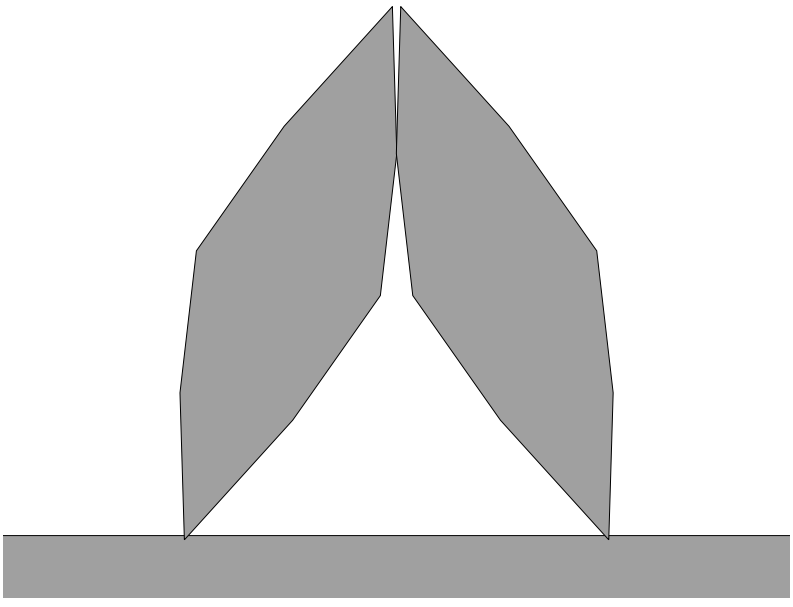

Fig. 8.3 Two particles leaning onto each other in an unstable equilibrium.

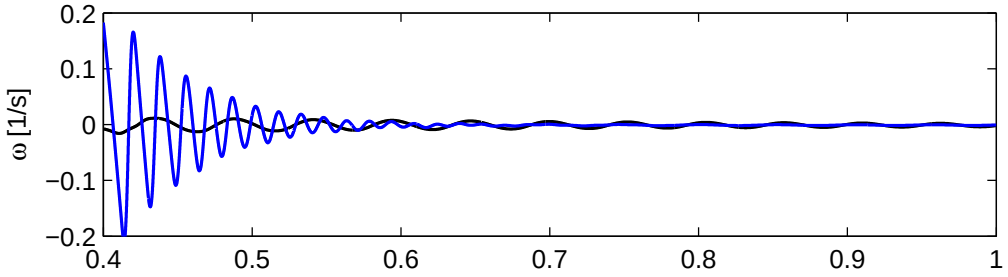

Fig. 8.4 Oscillations in the two particle configuration decay faster for the damped case (black) than for the undamped case (blue) but remain slightly stronger in the long term.

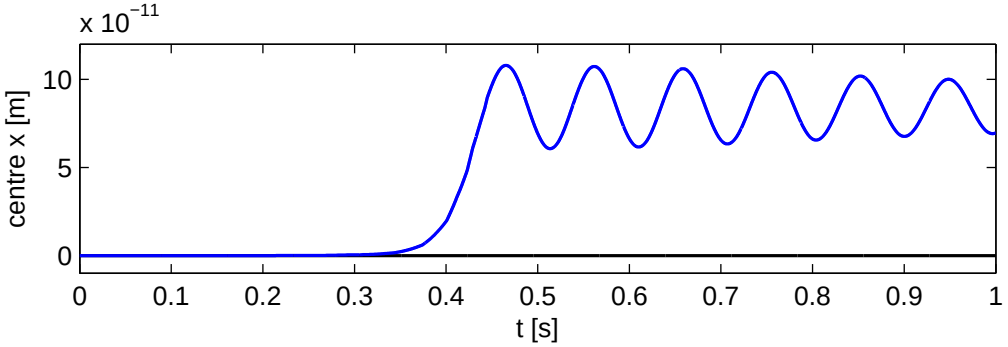

Fig. 8.5 The horizontal component in the centre of mass coordinates of the two particle problem deviates strongly from its initial position in the undamped case (blue), while the damped case (black) is essentially stable.

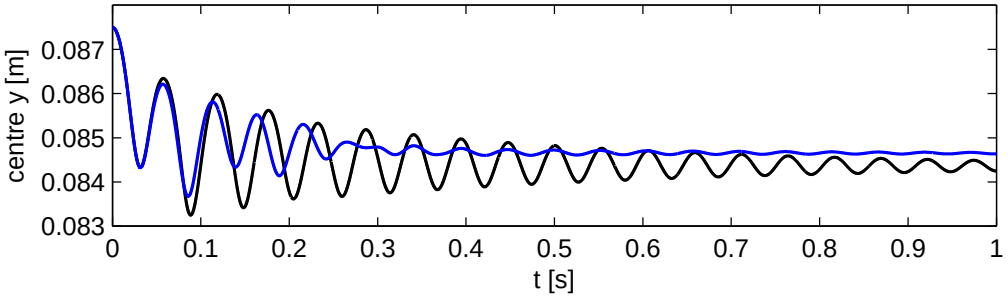

Fig. 8.6 Oscillations in the vertical component of the centre of mass coordinates of the two particle problem are stronger in systems with rotation damping (blue) than in systems without (black), but the order of magnitude is the same in both cases.

8.4.2 Equilibration of particles in a resting box

We revisit the problem of equilibration of particles in a resting box from section 7.6. Whereas the undamped configuration showed unphysical stagnation of the kinetic energy, which dissipated when the rotational degrees of freedom were turned off, the damped solution shows a complete absence of kinetic energy without any spikes from reordering of the particle orientation (Fig. 8.7). In the same way, the vertical component of the centre of mass shows no drift when the rotation damping is enabled, as opposed to the case without rotation damping, see Fig. 8.8.

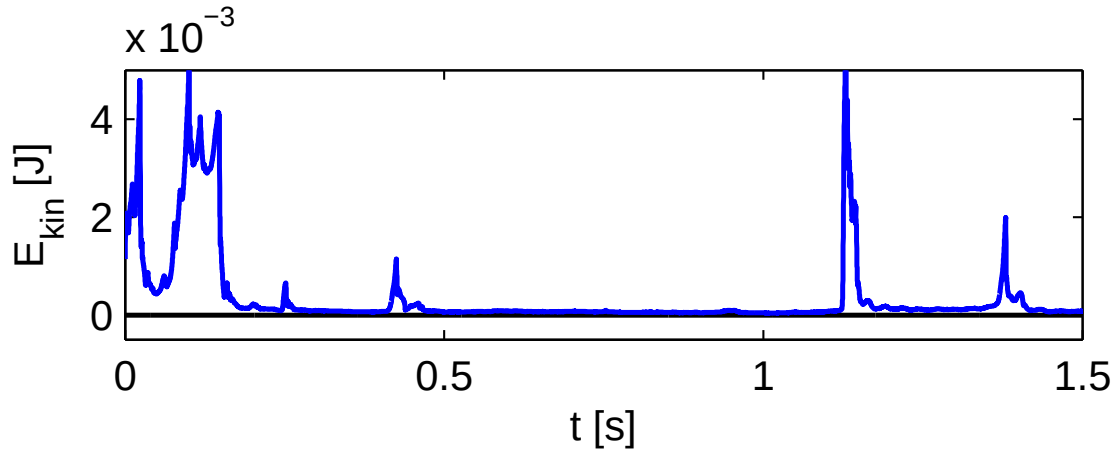

Fig. 8.7 The mean kinetic energy for the equilibrating particle configuration in a resting box shows is stagnating at high magnitude, with many large energy spikes from reordering of the particle configuration (blue line). With rotation damping, the transfer of energy into the rectilinear degrees of freedom is inhibited, and the kinetic energy in the stable state becomes zero (black line). The simulations were restarted with configurations from previous simulations.

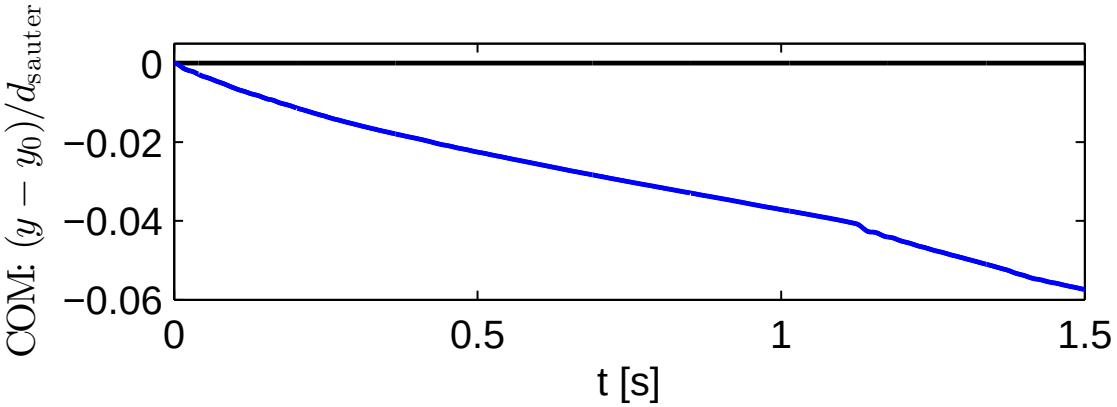

Fig. 8.8 As the rotation damping prevents additional noise in the rectilinear degrees of freedom, the drift in the centre of mass height can be exactly compensated, and the configuration will be stable (black line), compared with the non-stabilized solution (blue line).

8.4.3 Revisiting the granular heap

We apply our damping formalism to the problem of the granular heap from section 7.5. When we ran the simulation without rotational damping, we found that remaining energy in the rotational degrees of freedom was spreading into the rectilinear degrees of freedom and increasing the creep in the centre of mass position. Repeating the same simulation with the same parameters and additionally the rotation damping formalism, we were able to compensate the downward drift of the centre of mass exactly (Fig. 8.9), and to keep the kinetic energy in the equilibrium state at zero (Fig. 8.10).

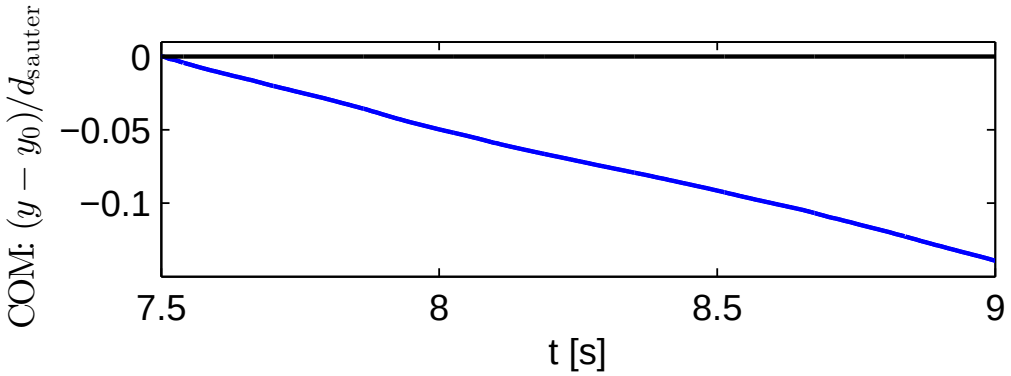

Fig. 8.9 Compared to the undamped approach (blue line) with a vertical centre of mass drift of about 10% of the mean particle diameter, the result of the stabilized formalism is perfectly stable (black line).

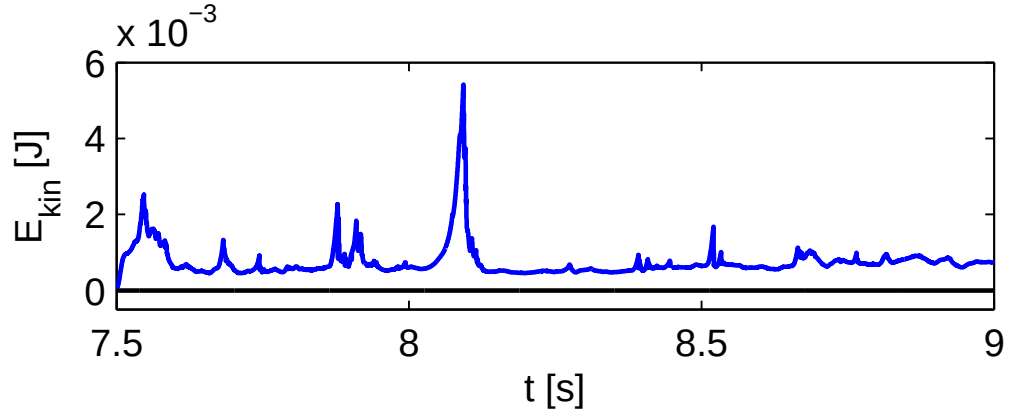

Fig. 8.10 With rotational damping, the residual kinetic energy for the heap configuration in mechanical equilibrium is zero, as the centre of mass drift is perfectly compensated (black line), whereas the unstabilized configuration shows an unphysically stagnating kinetic energy with random fluctuations (blue line).

8.5 Summary of the rotation damping

Residual noise in the angular degrees of freedom spreads into the rectilinear degrees of freedom, where it can no longer be compensated by friction and velocity dependent damping. To maintain the constraint of orientation, and thus to reduce the drift in the rectilinear degrees of freedom, stabilization of the rotational degrees of freedom is necessary. Velocity based damping works for simple configurations, but underestimates the necessary damping force in many-body configurations. In this section we have outlined a formalism for stabilization of the angular degrees of freedom in analogy to the DEM friction formalism. We have implemented a proof of concept, and can show, that for restarted many-body configurations the residual kinetic energy will be exactly compensated. In simple configurations some drift still remains, so optimisation is still required. The auxiliary variables b_I, b_{II}, eqs. (8.10,8.11), can be extended to include the angular acceleration $\dot{\omega}$, however further analysis is required to determine the effectiveness of the additional term.

Chapter 9

Conclusion

For a long time, static friction in many-body systems with arbitrary contact orientation as a reaction to prescribed normal forces has eluded treatment. In this work, we have derived a "numerically exact" formalism for Coulomb friction, in the sense, that the friction computation is only affected by rounding errors, not by the discretisation of the time-integrator. Our approach uses the framework of Differential Algebraic Equations (DAE) as the language of constraint problems like static friction. Analysis of the phase-flow around the static-friction constraint provided us with the criteria necessary to distinguish between static and dynamic friction. We could then evaluate the Coulomb friction as a reactive force based on the applying normal forces and relative tangential accelerations at each contact of a many-particle system. From the mathematical point of view, the results are both necessary and unique, and therefore parameter free. The criterion is local, so that unphysical global jumps in the value of the friction force can not occur. The formalism itself is applicable whenever there is a DAE with unilateral constraints and bounded variation where reactive forces must be computed from the priorly determined normal forces. Whenever there is no explicit functional velocity dependence for friction (e.g. viscous or turbulent fluids), the formalism is applicable when force components must be computed which should not vanish with the velocity. That means, the formalism is not only applicable for sliding friction, but also for rolling and pivoting friction. We have provided the necessary adaptations for use with constant timesteps and that no numerically problematic concepts are required, such as determination of roots in the relative velocities for finite timesteps. While the formalism was presented in two-dimensions only, we also showed what is required for a three-dimensional extension. For verification, we computed several problem geometries in a discrete-element-method (DEM) simulation, and compared the results with different friction laws. We further investigated the effect of the timestep and different time integration schemes. We found, that a second order Backward Difference Formula is the most stable numerical integrator for our constraint problem. The DAE-formalism gives superior results for vibrated systems compared to the Cundall-Strack modelling. For long-term simulations of static configurations, the DAE-method showed

irregular residual kinetic energy.

Our approach can also be extended to multibody-finite element methods (FEM) due to the geometric similarity of the elements. Typically, for contact problems with finite elements, regularizations, "rigid-body approaches" (by simultaneously computing normal and tangential forces, with all the complexities which have been mentioned in sec. 2.4, 2.5) or variational criteria[131, 132, 133] are discussed. With our approach, via eq.(5.39,5.40), the friction between contacting element pairs can be computed directly, as long as normal forces and tangential accelerations are known. As the discrete element method already is a penalty method, our approach can also be used with a penalty FEM with slightly penetrating contacts.

As many constraint problems, our DAE-friction formalism is affected by numerical errors which induce noise terms and residual kinetic energy. In particular for discrete element methods, this is caused by inconsistencies between the linear and angular coordinates and velocities and leads to a drift which cannot be compensated by friction or damping alone. An additional numerical stabilisation mechanism was developed which damps the noise from the angular degrees of freedom analogously to the static friction for the linear degrees of freedom. This stabilisation formalism completely eliminates the noise in the kinetic energy and the drift for the centre of mass.

References

[1] E. Hairer and G. Wanner. *Solving ordinary differential equations II: Stiff and differential-algebraic problems*. Springer, 2nd edition, 1996.

[2] A.F. Filippov. *Differential equations with discontinuous righthand sides*, volume 18 of *Mathematics and its Applications*. Springer, 1 edition, 1988.

[3] I. M. Hutchings. Leonardo da vinci s studies of friction. *Wear*, (360):51 – 66, 2016.

[4] G. Amontons. On the resistance originating in machines. *Proceedings of the French Royal Academy of Sciences*, 1699.

[5] D. Dowson. *History of tribology*. Wiley, 2nd edition, 1998.

[6] B. Persson. *Sliding friction: Physical principles and applications*. NanoScience and Technology. Springer, 2nd edition, 2000.

[7] V. Popov. *Contact mechanics and friction: Physical principles and applications*. Springer, 2010.

[8] C Gillmor. *Coulomb and the evolution of physics and engineering in eighteenth-century france*. Princeton University Press, 2017.

[9] Elena Popova and Valentin L. Popov. The research works of coulomb and amontons and generalized laws of friction. *Friction*, 3(2):183–190, Jun 2015.

[10] ASM International Handbook Committee. *Friction, Lubrication, and Wear Technology*, volume 18 of *ASM handbook*. ASM International, 1992.

[11] W. Benenson, J.W. Harris, H. Stöcker, and H. Lutz, editors. *Handbook of physics*. Springer, 2002.

[12] A.J. Morin. New friction experiments carried out at metz in 1831-1833. *Proceedings of the French Royal Academy of Sciences*, 4(1):128, 1833.

[13] Coulomb. Théorie des machines simples: en ayant égard au frottement de leurs parties et à la roideur des cordages. *Bachelier*, 1809.

[14] A. Plößl and G. Kräuter. Wafer direct bonding: tailoring adhesion between brittle materials. *Materials Science and Engineering: Reports*, 25(1):1–88, 1999.

[15] E. Rabinowicz. *Friction and Wear of Materials*. Wiley, New York, 1965.

[16] Hans-Georg Matuttis and Jian Chen. *Understanding the discrete element method*. Wiley, 1 edition, 2014.

[17] W. Krenkel and N. Langhof. Ceramic matrix composites for high performance friction applications. *Proceedings of the IV Advanced Ceramics and Applications Conference*, pages 13–28, 2017.

[18] F. P. Bowden and D. Tabor. The area of contact between stationary and between moving surfaces. *Proceedings of the Royal Society of London A: Mathematical, Physical and Engineering Sciences*, 169(938):391–413, 1939.

[19] F.P Bowden and D. Tabor. The theory of metallic friction and the role of shearing and ploughing. *Australia. Council for scientific and industrial research. Bulletin*, 145, 1942.

[20] F. Bowden and D. Tabor. *The friction and lubrication of solids*. Clarendon Press, 1954.

[21] A.I. Bailey and J.S. Courtney-Pratt. The area of real contact and the shear strength of monomolecular layers of a boundary lubricant. In *Proceedings of the Royal Society of London A: Mathematical, Physical and Engineering Sciences*, volume 227 of *1171*, pages 500–515, 1955.

[22] F. Bowden and D Tabor. *The friction and lubrication of solids*. Clarendon Press, 2nd edition, 2001.

[23] R.J. Covert, R. Ott, and D. Ku. Friction characteristics of a potential articular cartilage biomaterial. *Wear*, 255 .:1064–1068, 2003.

[24] F. P. Bowden and W. R. Throssell. Adsorption of water vapour on solid surfaces. *Proceedings of the Royal Society of London A: Mathematical, Physical and Engineering Sciences*, 209(1098):297–308, 1951.

[25] P Blau. *Friction science and technology: From concepts to applications*. CRC Pres, mechanical engineering edition, 2008.

[26] B. Bhushan and B. Gupta. *Handbook of tribology: materials, coatings, and surface treatments*. CRC series: mechanics and materials science. McGraw Hill, 1991.

[27] P.W. Anderson. More is different. *Science*, 177(4047):393–396, 1972.

[28] B. Bushan. Nanotribology and nanomechanics in nano/biotechnology. *Phil. Trans. Roy. Soc. A*, 366:1499–1537, 2008.

[29] B. Bhushan. *Handbook of Micro/Nano Tribology*. CRC series mechanics and materials science. Taylor & Francis, 1995.

[30] J. Israelachvili. *Intermolecular and Surface Forces*. Elsevier Science, 2015.

[31] N. Sasaki, Itamura N., H. Asawa, D. Tsuda, and K. Miura. Superlubricity of graphene/c_{60}/graphene interface -experiment and simulation. *Tribology Online*, 7(3): 96–106, 2012.

[32] J.J. Kalker. *Three-Dimensional Elastic Bodies in Rolling Contact*. Springer Netherlands, 2013.

[33] Hans-Jürgen Tillemans and Hans J. Herrmann. Simulating deformations of granular solids under shear. *Physica A: Statistical Mechanics and its Applications*, 217(3): 261 – 288, 1995.

[34] P. A. Cundall and O. D. L. Strack. A discrete numerical model for granular assemblies. *Géotechnique*, 29(1):47–65, 1979.

[35] J. Shäfer, S. Dippel, and D. E. Wolf. Force schemes in simulations of granular materials. *J. Phys. I France*, 6(1):5–20, 1996.

[36] H.-G. Matuttis. Simulations of the pressure distribution under a two dimensional heap of polygonal particles. *Granular Matter*, 1(2):83–91, 1998.

[37] J. J. Moreau. Unilateral contact and dry friction in finite freedom dynamics. In J. J. Moreau. and P. D. Panagiotopoulos, editors, *Nonsmooth Mechanics and Applications*, volume 302 of *CISM Courses and Lectures*, pages 1–82. Springer, 1988.

[38] J.J. Moreau and P.D. Panagiotopoulos, editors. *Nonsmooth Mechanics and Applications*, volume 302 of *CISM International Centre for Mechanical Sciences*. Springer, 1988.

[39] F. Dubois, V. Acary, and Jean M. The contact dynamics method: A nonsmooth story. *Comptes Rendus Mécanique*, 346(3):247–262, 2018.

[40] F. Pfeiffer and C. Glocker. *Multibody Dynamics with unilateral contacts*. Wiley Interscience, New York, 1997.

[41] F. Radjai, M. Jean, J.J. Moreau, and S. Roux. Force distributions in dense two-dimensional granular systems. *Phys. Rev. Lett.*, 77(2):274–, July 1996.

[42] F. Radjai, D.E. Wolf, M. Jean, and J.J. Moureau. Bimodal character of stress-transmission in granular packings. *Phys. Rev. Lett.*, 80:61–64, 1998.

[43] F. Radjai. Contact dynamics method. *Eur. J. Environ. Civ. Eng.*, 12(7-8):871–900, 2008.

[44] Computational Granular Physics, http://cgp-gateway.org, last visited 07/2018.

[45] Markus Kunze and Manuel D.P. Monteiro Marques. An introduction to moreau's sweeping process. In *Impacts in Mechanical Systems*, pages 1–60. Springer Berlin Heidelberg, 2000.

[46] Jean-Jacques Moreau. Liaisons unilatérales sans frottement et chocs inélastiques. *Comptes-rendus des séances de l'Académie des sciences. Série 2, Mécanique-physique, chimie, sciences de l'univers, sciences de la terre*, 296(19):1473–1476, 1983.

[47] David Stewart. A high accuracy method for solving odes with discontinuous right-hand side. *Numer. Math.*, 58:299–328, 1990.

[48] D. E. STEWART and J. C. TRINKLE. An implicit time-stepping scheme for rigid body dynamics with inelastic collisions and coulomb friction. *International Journal for Numerical Methods in Engineering*, 39(15):2673–2691, 1996.

[49] M. Anitescu and F.A. Potra. Formulating dynamic multi-rigid-body contact problems with friction as solvable linear complementarity problems. *Nonlinear Dynamics*, 14:231, 1997.

[50] David E. Stewart. Rigid-body dynamics with friction and impact. *SIAM Review*, 42(1):3–39, 2000.

[51] E. Hairer, S. P. Norsett, and G. Wanner. *Solving Ordinary Differential Equations I: Nonstiff Problems*. Springer, 2nd. edition, 1993.

[52] D. Stewart. *Dynamics with Inequalities*. Society for Industrial and Applied Mathematics, 2011.

[53] R. Leine and H. Nijmeijer. *Dynamics and Bifurcations of Non-Smooth Mechanical Systems*, volume 18 of *Lecture Notes in Applied and Computational Mechanics*. Springer, 2004.

[54] D. Kaplan and L. Glass. *Understanding Nonlinear Dynamics*, volume 19 of *Texts in Applied Mathematics*. Springer, 1995.

[55] A. F. Filippov. Differential equations with discontinuous right-hand side. In *AMS Translations*, volume 42 of *ser. 2*, pages 199–231. American Mathematical Society, 1964.

[56] G.V. Smirnov. *Introduction to the Theory of Differential Inclusions*, volume 41 of *Graduate Studies in Mathematics*. American Mathematical Society, 2002.

[57] E. Mahmudov. *Approximation and Optimization of Discrete and Differential Inclusions*. Elsevier, 2011.

[58] J. Aubin and A. Cellina. *Differential Inclusions Set-Valued Maps and Viability Theory*. Springer, 2012.

[59] Philip R. Dahl. Solid friction damping of mechanical vibrations. *AIAA Journal*, 14(12):1675–1682, 1976.

[60] Philip R. Dahl. *Measurement of solid friction parameters of ball bearings*, volume Proceedings: Sixth Annual Symposium on Incremental Motion Control Systems and Devices, May 24-27, 1977. Board of Trustees of the University of Illinois at Urbana-Champaign, 1977.

[61] C. Canudas de Wit, H. Olsson, K. J. Astrom, and P. Lischinsky. A new model for control of systems with friction. *IEEE Transactions on Automatic Control*, 40(3): 419–425, Mar 1995.

[62] D. Krengel, S. Strobl, A. Sack, M. Heckel, and T. Pöschel. Pattern formation in a horizontally shaken granular submonolayer. *Granular Matter*, 15(3):377–387, 2013.

[63] Dominik Krengel, Wei Shen Cheng, Jian Chen, and Hans-Georg Matuttis. The effect of the shape of granular particles on density. *Journal of the Physical Society of Japan*, 84(6):064401, 2015.

[64] B. Andreotti, Y. Forterre, and O. Pouliquen. *Granular Media: Between Fluid and Solid*. Cambridge University Press, 2013.

[65] G. Darwin. On the horizontal thrust of a mass of sand. *Institution of Civil Engineers*, 1883.

[66] J. Boussinesq. Note on mr. g. h. darwin's paper 'on the horizontal thrust of a mass of sand'. *Minutes of the Proceedings of the Institution of Civil Engineers*, 72:262–271, 1883.

[67] H.-G. Matuttis. Simulation of the pressure distribution under a two-dimensional heap of polygonal particles. *Granular Matter*, 1:83–91, 1998.

[68] L. Vanel, D. Howell, D. Clark, R. P. Behringer, and E. Clément. Memories in sand: Experimental tests of construction history on stress distributions under sandpiles. *Physical Review E*, 60(5), 1999.

[69] O. Reynolds. On the dilatancy of media composed of rigid particles in contact. *Phil. Mag.*, 20:469–481, 1885.

[70] I. Roberts. On the pressure of wheat stored in elongated cells or bins. *Engineering*, 34:399, 1882.

[71] I. Roberts. Determination of the vertical and lateral pressures of granular substances. *Proc. Royal Soc. Lond.*, 36:225–240, 1884.

[72] H.A. Janssen. Versuche über Getreidedruck in Silozellen. *Ztg. Ver. dt. Ing.*, 39:1045–1049, 1895.

[73] H.S. Cuming. On hour glasses. *British Archeological Asssociation*, 29:130–, 1873.

[74] D.H. Cornforth. *Landslides in practise*. Wiley, 2005.

[75] D. Schulze. *Pulver und Schüttgüter*. Springer Vieweg, 3rd edition, 2014.

[76] H.M. Jaeger, S.R. Nagel, and R.P. Behringer. Granular solids, liquids, and gases. *Reviews of Modern Physics*, 68(4):1259–1273, 1996.

[77] Y. Forterre and O. Pouliquen. Long surface wave instability in dense granular flows. *J. Fluid Mech.*, 2003.

[78] G.W. Baxter, R. Behringer, T. Fagert, and G.A. Johnson. Pattern formation in flowing sand. *Physical Review Letters*, 62(24):2825–2828, 1989.

[79] F. Radjai and F. Dubois. *Discrete-Element modelling of granular materials*. Wiley, 2011.

[80] N. Estrada, E. Azéma, F. Radjai, and A. Taboada. Identification of rolling resistance as a shape parameter in sheared granular media. *Phys. Rev. E*, 84:011306, 2011.

[81] A. H. Clark, J. D. Thompson, M. D. Shattuck, N. T. Ouellette, and C. S. 2 O'Hern. Critical scaling near the yielding transition in granular media. *Phys. Rev. E*, 97(6): 062901, 2018.

[82] R. A. Bagnold. Experiments on a gravity-free dispersion of large solid spheres in a newtonian fluid under shear. *Proceedings of the Royal Society of London A: Mathematical, Physical and Engineering Sciences*, 225(1160):49–63, 1954.

[83] O. Pouliquen. Scaling laws in granular flows down rough inclined planes. *Phys. Fluids*, 11:542–548, 1999.

[84] A. Rosato, K. J. Strandburg, F. Prinz, and R. H. Swendsen. Why the brazil nuts are on top: Size segregation of particulate matter by shaking. *Phys. Rev. Lett.*, 58(10), 1987.

[85] O. Pouliquen, J. Delour, and S.B. Savage. Fingering in granular flows. *Nature*, 386:816–817, 1997.

[86] S. Ulrich, M. Schröter, and H. L. Swinney. Influence of friction on granular seggregation. *Phys. Rev. E*, 76:042391, 2007.

[87] A. Džiugys and R. Navakas. The role of friction in mixing and segregation of granular material. *Granular Matter*, 11:403–416, 2009.

[88] T. Elperin and E. Golshtein. Effects of convection and friction on size seggregation in vibrated granular beds. *Physica A*, 247:67–78, 1997.

[89] EMSA. The world merchant fleet in 2016. Technical report, EMSA, 2017.

[90] M. C. Munro and A. Mohajerani. Liquefaction incidents of mineral cargos on board bulk carriers. *Advances in Materials Scinece and Engineering*, 2016.

[91] D. S. Liyanapathirana and H. G. Poulos. A numerical model for dynamic soil liquefaction analysis. *Soil dynamics and Earthquake engineering*, 22:1007–1015, 2002.

[92] A. Yamaguchi, T. Mori, M. Kazama, and N. Yoshida. Liquefaction in tohoku district during the 2011 off the pacific coast of tohoku earthquake. *Soils and Foundations*, 52(5):811–829, 2012.

[93] Matuttis, Hans-Georg, Nawa, Masaki, and Krengel, Dominik. Stress-strain diagrams for non-convex particles. *EPJ Web Conf.*, 140:06005, 2017.

[94] Krengel, Dominik and Matuttis, Hans-Georg. Comparing numerically exact and modelled static friction. *EPJ Web Conf.*, 140:15020, 2017.

[95] J. Chen. *Discrete element method for 3d simulations of mechanical systems of non-spherical granular materials*. PhD thesis, The University of Electro-Communications, 2012.

[96] MATLAB, Version: 8.3.0.532 The Mathworks (R2014a).

[97] Lawrence F. Shampine and Mark W. Reichelt. The matlab ode suite. *SIAM J. Sci. Comput.*, 18(1):1–22, January 1997.

[98] P. Bogacki and L.F. Shampine. A 3(2) pair of runge - kutta formulas. *Applied Mathematics Letters*, 2(4):321–325, 1989.

[99] J.R. Dormand and P.J. Prince. A family of embedded runge-kutta formulae. *Elsevier Journal of Computational and Applied Mathematics*, 6(1):19–26, 1980.

[100] C. William Gear. *Numerical initial value problems in ordinary differential equations*. Prentice-Hall, Englewood Cliffs, NJ, 1971.

[101] J. Baumgarte. Stabilization of constaints and integrals of motion in dydynamic systems. *Computational Methods in Applied Mechanical Engineering*, 1(1):11–16, 1972.

[102] C. Lubich. On the convergence of multistep methods for nonlinear stiff differential equations. *Numerische Mathematik*, 58(1):839–853, Dec 1990.

[103] Edda Eich. Convergence results for a coordinate projection method applied to mechanical systems with algebraic constraints. *SIAM Journal on Numerical Analysis*, 30(5):1467–1482, 1993.

[104] L. Petzold. Differential algebraic equations are not odes. *SIAM Journal on Scientific and Statistical Computing*, 3(3):367–384, 1982.

[105] Klaus Jänich. *Analysis für Physiker und Ingenieure: Funktionentheorie, Differentialgleichungen, spezielle Funktionen*, volume Funktionentheorie, Differentialgleichungen, spezielle Funktionen. Springer, 4th edition, 2001.

[106] G. Birkhoff and G.C. Rota. *Ordinary differential equations*. Wiley, 1989.

[107] A. Coddington and N. Levinson. *Theory of ordinary differential equations*. Robert E. Krieger, 1984.

[108] M. Tenenbaum and H. Pollard. *Ordinary differential equations*. Dover Books on Mathematics Series. Dover Publications, Incorporated, 2012.

[109] V. I. Arnold. *Mathematical methods of classical mechanics*. Graduate Texts in Mathematics. Springer-Verlag, 2nd edition, 1989.

[110] S. Zdravkovska and P.L. Duren. *Golden years of Moscow mathematics*. History of Mathematics Series. Amer Mathematical Society, 2007.

[111] J.P. Den Hartog. Forced vibrations with combined viscous and coulomb damping. *Phil. Mag. Ser. 7*, 9:801–817, 1930.

[112] R. Leine and H. Nijmeijer. *Dynamics and bifurcations of non-smooth mechanical systems*. Lecture Notes in Applied and Computational Mechanics. Springer, 2013.

[113] J.J. Moreau and P.D. Panagiotopoulos. *Nonsmooth mechanics and applications*. CISM International Centre for Mechanical Sciences. Springer Vienna, 2014.

[114] D. Wolf, priv. comm., Powders and Grains conference, Montpellier (2017).

[115] S. Luding and S. McNamara. How to handle the inelastic collapse of a dissipative hard-sphere gas with the TC model. *Granular Matter*, 1(3):113–128, 1998.

[116] P. Painleve. Sue les lois du frottement de glissement. *C. R. Acad. Sci.*, 121:112–115, 1895.

[117] J.H. Jellet. *Treatise on the theory of friction*. Hodges, Foster and Co, 1872.

[118] L. Lecornu. Sur la loi de coulomb. *Comptes Rendus Acad. Sci. Paris*, 140:847–848, 1905.

[119] L. X. Anh. *Dynamics of Mechanical Systems with Coulomb Friction*. Springer, 2003.

[120] G. Hamel. *Theoretische Mechanik*. Springer, 1949.

[121] P. Lötstedt. Coulomb friction in two-dimensional rigid body systems. *ZAMM - Journal of Applied Mathematics and Mechanics / Zeitschrift für Angewandte Mathematik und Mechanik*, 61(12):605–615, 1981.

[122] Frank Génot and Bernard Brogliato. New Results on Painlevé Paradoxes. Technical Report RR-3366, INRIA, February 1998.

[123] J. Chen, A. Schinner, and H.-G. Matuttis. Static friction, differential algebraic systems and numerical stability. *Physics Procedia*, 6:65–75, 2010.

[124] Franck Radjai. *Dynamique des rotations et frottement colllectiv dans les systémes granulaires*. PhD thesis, University Paris Orsay, 1995.

[125] K.L. Johnson and K.K.L. Johnson. *Contact Mechanics*. Cambridge University Press, 1987.

[126] S. H. Strogatz. *Nonlinear Dynamics And Chaos*. Sarat Book House, 2007.

[127] S. Luding, M. Müller, and S. McNamara. The validity of "molecular chaos" in granular flows. In *World Congress on Particle Technology*, 1998.

[128] G.F. Swain and A. Mehmel. *Festigkeitslehre*. Springer, 1st edition, 1928.

[129] D. Morin. *Introduction to Classical Mechanics: With Problems and Solutions*. Cambridge University Press, 2008.

[130] G. Engeln-Müllges, K. Niederdrenk, and R. Wodicka. *Numerik-Algorithmen*. Springer, 10th edition, 2011.

[131] P. Wriggers. *Nonlinear Finite Element Methods*. Springer Berlin Heidelberg, 2008.

[132] N. Kikuchi and J.T. Oden. *Contact Problems in Elasticity: A Study of Variational Inequalities and Finite Element Methods*. Studies in Applied Mathematics. Society for Industrial and Applied Mathematics, 1988.

[133] Maik Brinkmeier, Udo Nackenhorst, and Matthias Ziefle. *Computational Contact Mechanics*, chapter Modern Approaches on Rolling Contact, pages 83–127. Springer, 2006.

Published works

List of publications related to this thesis

1. D. Krengel and H.-G. Matuttis. "Comparing numerically exact and modelled static friction." International Conference Powders and Grains 2017, EPJ Web of Conferences, Vol. 140, 15020, Sci- ences, 2017, 4 pages

2. D. Krengel and H.-G. Matuttis. "Implementation of static friction for many-body problems in two-dimensions." J. Phys. Soc. Jpn. 87, 2018, 16 pages

Published papers

1. P. Müller, D. Krengel, and T. Pöschel. "Negative coefficient of normal restitution." Physical Review E 85.4 (2012): 041306

2. D. Krengel, S. Strobl, A. Sack , M. Heckel, and T. Pöschel. "Pattern formation in a horizontally shaken granular submonolayer." Granular Matter 15.3 (2013): 377-387.

3. D. Krengel, W. S. Cheng, J. Chen, and H.-G. Matuttis. "The effect of the shape of granular particles on density." Journal of the Physical Society of Japan 84.6 (2015): 064401.

4. H.-G. Matuttis, M. Nawa, and D. Krengel. "Stress-Strain diagrams for non-convex particles." International Conference Powders and Grains 2017, EPJ Web of Conferences, Vol. 140, 06005, Sci- ences, 2017.

5. D. Krengel and H.-G. Matuttis. "Some basic ideas on friction", To be published in Environmental Geotechnics Themed Issue: Thermodynamics in Material Modelling and Geotechnical Design, 16 pages, invited paper

Conference Attendance

1. 2014, 69th spring meeting of the Japanese Physical Society: Oral Presentation
2. 2014, 28th National Congress of Fluid Dynamics: Oral Presentation
3. 2014, 63rd National Congress of Theoretical and Applied Mechanics: Oral Presentation
4. 2015, 70th spring meeting of the Japanese Physical Society: Oral Presentation
5. 2015, International Workshop Friction -from atomic to geophysical scales-, Poster Presentation
6. 2016, 71st spring meeting of the Japanese Physical Society: Oral Presentation
7. 2016, International conference THESIS 2016, TWO-PHASE MODELLING FOR SEDIMENT DYNAMICS IN GEOPHYSICAL FLOWS, Poster Presentation
8. 2017, International conference Powders and Grains, Poster Presentation
9. 2017, Tohoku Daigaku AIMR: Invited Seminar Talk
10. 2017, Nihon Daigaku: Invited Seminar Talk
11. 2018, 73rd spring meeting of the Japanese Physical Society: Oral Presentation
12. 2018, International Workshop Rheology of disordered particles, Oral Presentation
13. 2018, 32th National Congress of Fluid Dynamics: Oral Presentation

Acknowledgments

First and foremost, I would like to express my sincere gratitude to my supervisor, Associate Professor Dr. rer. nat. Hans-Georg Matuttis, for the opportunity to work on this project, for his patient guidance and contribution to this research, and his motivation and encouragement ever since I started as a research student in his group.

I am grateful for the financial support of the Japanese Government (MEXT) scholarship.

This work would not have been possible without the patient support of several people.

I would like to thank Jan Müller for his help with some of the experiments, discussions and proofreading of the manuscript.

I am grateful for the invaluable discussions with Jian Chen and Henrik Tünnermann, the proofreading of the thesis and encouragement when it seemed as if nothing made sense.

I would like to acknowledge all the members of the Matuttis laboratory through the years who supported me with all the issues big and small and providing a hand during some of the experiments.

I would like to thank Aki Hatae for providing hand and foot with some pictures and her support and encouragement.

Finally, I wish to thank my parents and my younger sister for their love and encouragement through my years of study and research for this thesis. I could not have managed this work without you. Thank you.